AN ABSTRACT OF THE THESIS OF

Paiboon Sripakagorn for the degree of Master of Science in Mechanical Engineering presented on December 1, 1997. Title: Frequency and Phase Response of a Resonantly-Coupled Alpha Stirling Cooler.

Abstract approved: _____
Richard B. Peterson

A resonantly-coupled α-Stirling (RCAS) cooler was designed and constructed. Tests on air and helium were performed with constant driving displacement over a range of frequencies. The effects of changing driving amplitude and charged pressure were studied.

The use of stainless steel bellows in place of pistons eliminated the problem of piston seals and relaxed the construction tolerances. The fatigue life of the bellow is, however, a problem. The experimental optimization based on Taguchi methods was performed on regenerator mass, regenerator wire diameter, vibrating mass, and damping coefficient.

Driven by a voice coil actuator, the characteristic phase shift of the Stirling cycle cooler was demonstrated where the hot-end displacement led the cold-end displacement. The 90 ° phase shift was selected as the natural frequency.

The pressure-volume diagrams for each working space were plotted and the indicated powers were determined. The compression powers in the hot and cold-ends show maximum values near the natural frequency. The mechanisms are different. At the hot-end where the displacement was kept constant, operation near the natural frequency gave a maximum pressure ratio and also maximized the compression power. The phase shifts in the cold-end were, however, relatively constant. The maximum pressure ratio and amplitude gave the maximum expansion power near the natural frequency.

The expansion powers in the cold-end as indicators of cooling potential were approximately 2-4 watts for the air case, and 3-7 watts for the helium case. In both air and helium tests, the value of the parasitic losses reached 12 watts.

The temperature difference developed across the regenerator is considered an indication of the cooling capacity. Good correlations were found between the indicated cooling capacity in the expansion space and the temperature difference.

For a given size of cooler, the use of helium offered higher cooling capacity due to smaller pressure drop loss and smaller amplitude ratio. Higher cooling performance was also attained from helium at elevated pressures.

Frequency and Phase Response

of

a Resonantly-Coupled Alpha Stirling Cooler.

by

Paiboon Sripakagorn

A THESIS

submitted to

Oregon State University

in partial fulfillment of
the requirements for the
degree of

Master of Science

Presented December 1, 1997
Commencement June 1998

Master of Science thesis of Paiboon Sripakagorn presented on December 1, 1997

APPROVED:

Major Professor, representing Mechanical Engineering

Head of Department of Mechanical Engineering

Redacted for privacy

Dean of Graduate School

I understand that my thesis will become part of the permanent collection of Oregon State University libraries. My signature below authorizes release of my thesis to any reader upon request.

Redacted for privacy

Paiboon Sripakagorn, Author

ACKNOWLEDGEMENTS

My most sincere gratitude is extended to my academic advisor, Prof. Richard B. Peterson who conceived of the original configuration and the design of the device and allowed me to have good experiences in undertaking this investigation. His support and thoughtful suggestions that nurtured my academic growth are greatly appreciated.

Helpful discussions on Taguchi method with Prof. David G. Ullman in his Robust design course and his guidance in the optimization part of this investigation are acknowledged. Thanks also to my fellow graduate students in the robust design course: Thanat Jitpraphai, Thanat Moungkeow and Yuqing Liu who made the experiments more enjoyable and fruitful.

Timely help with manufacturing processes together with experience and expertise were provided by Orrie Page and were greatly appreciated. Thanks also to Majed Al Hazmy who is working in the same field as mine and provided many useful suggestions on experiment results.

My studies in the United States were supported by the Royal Thai Government. My love and appreciation also go to my parents and my sister for their moral support and encouragement through these years.

TABLE OF CONTENTS

TABLE OF CONTENTS(Continued)

TABLE OF CONTENTS(Continued)

Chapter Page

LIST OF FIGURES

LIST OF FIGURES (Continued)

LIST OF FIGURES (Continued)

Page

LIST OF FIGURES (Continued)

LIST OF TABLES

LIST OF APPENDIX FIGURES

LIST OF APPENDIX TABLES

LIST OF APPENDIX TABLES (Continued)

LIST OF APPENDIX TABLES (Continued)

Frequency and Phase Response
of
a Resonantly-Coupled Alpha Stirling Cooler

CHAPTER 1
INTRODUCTION

1.1) Research objectives

The objectives of the study are to develop a resonantly coupled α-Stirling (RCAS) cooler capable of cooling the cold side gas to a temperature below 0 °C, experimentally determine the frequency and phase response of the RCAS cooler, and determine how these factors affect cooling performance. The choice of air or helium as the working gas will also be investigated. The indicated work from the pressure-volume (P-V) diagram will be used for the energy balance analysis of the cooler.

1.2) Justification

A free-piston Stirling cooler offers many advantages over the original kinematic-type cooler. These advantages include simplicity in construction, expected longer life, potential for hermetic sealing, and good prospects for miniaturization. The main-stream interest in free-piston Stirling coolers has been on the piston-displacer design. However, in this type of cooler, the reliability of operation is of major concern due to the wear of the sliding seal. This problem also contributes to the contamination of the working fluid

and reduces shelf-life. Self-starting and quiet operation are also possible in the free-piston design, but in practice only coolers with highly accurate machining and assembly achieve these benefits. The interest in this study is on the alpha-configuration in which many attractive features are presented–simpler mechanical design, no sliding seals, high frequency operation, and ease of miniaturization–all of which minimize the drawbacks found in the piston-displacer type. Additional studies are, therefore, necessary to justify the promised performance. In this respect, general design ideas, especially in the area of the dynamics of operation, must be developed. A major part of this thesis is devoted to the study of the RCAS system dynamics and its influence on cooler performance.

1.3) Research approach

From preliminary work done at the OSU, the concept of the RCAS cooler was established with a proof-of-principle device operating with air at atmospheric pressure. The cooler generated a 20 °C temperature difference across the regenerator. The ability of the system to change the phase between the driving and the driven bellows with the variation in driving frequency was demonstrated. Using the same basic configuration in this study, the prototype cooler was modified to work with pressurized helium at the pressure of 1-2 bars. Details of the component design and construction will be presented later, but the original proof-of-principle device was modified to produce a cooling rate of 3-5 watts. The overall length and diameter of the device was approximately 20 cm and 8 cm, respectively, where the small size demonstrated the potential for miniaturization.

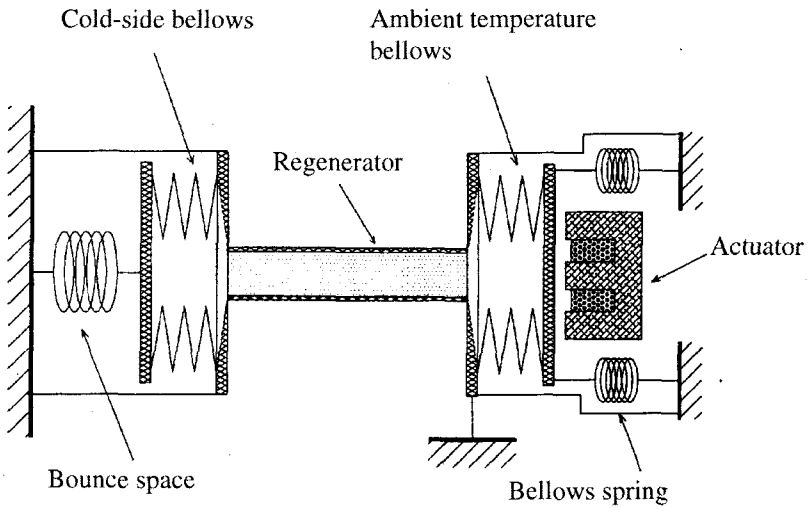

Fig. 1.1 Schematic diagram of a RCAS cooler.

The general design concept for the Stirling cooler will use forced convection to transfer heat from the bounce chamber. Natural convection will be used to transfer heat from the outside surface of the cylinder to the environment. In some studies, the cold cylinder is evacuated and covered to reduce convection and radiation losses. In this investigation, the heat load on the cold end was uncontrollable. The regenerator configuration for the cooler was a cylindrical tube packed with a porous media. Also, because a pressurized working gas was used, the whole device was sealed.

In the dynamics aspect, the device was instrumented to give the readings of the motions of both bellows and the pressure and temperature variations in the hot and the cold space. The amplitude and phase of the displacement were used for describing the resonantly-coupled motion. The indicated work and cooling effect were also determined from the pressure-volume diagrams. The gas temperature next to the exit of the regenerator in both sides gave an indication of cooling processes in both the hot and cold

spaces. The sinusoidal signal generated from a function generator was amplified by a power amplifier and fed to a voice coil actuator. The device was driven by the actuator at the frequency of the order of 100 Hz. As a result, the power input to the actuator could be monitored and the input power to the device at any operating condition could be determined.

1.4) Literature review

After the Stirling cycle machine was reinvented by the Dutch company N. V. Philips in the 1940s and 50s, many potential advantages including high thermal efficiency, mechanical simplicity, multifuel capability (in case of power plants) , and no use of greenhouse gases (in the case of refrigerators) were incentives for technological development. Hundreds of Stirling engines used in power generators were made by Philips in the 1950s (Walker, et al. (1979)). Stirling coolers were also introduced to the commercial market during this time as small air liquefiers. The increasing technological maturity brought the Stirling engine to a competitive position for both power and refrigeration machines. At the same time the advancement of the technology also placed higher requirements on performance. There are two main types of Stirling cycle machines, namely kinematic and free-piston machines. This review focuses on the development of the free-piston type. Applications as both an engine and a cooler will be presented. Technological developments in the component design area, together with experimental investigations, will be reviewed.

Applications of Stirling machines cover a wide range of possibilities. Rifkin (1980) illustrated the FPSE (free-piston Stirling engine) design of a 10 W cryocooler, a residential heat pump, an engine for vehicle propulsion, and a 1 MW powerplant. Teagan, et al. (1983) showed the distinct advantages of the Stirling engine over conventional engines in many applications including heat pumps, rural power generators and solar thermal generators. Many examples of applications, for instance an exhaust-driven automotive air conditioning system and a gas furnace air conditioner, have been presented by Walker, et al. (1992). To compete with well-established vapor compression machines, the possibility of applying Stirling refrigerators to the near-ambient temperature range was extensively investigated in both the US and other countries (Kagawa, et al. (1991), Walker, et al. (1992), Kim (1993)).

Despite these past studies, many technical areas remain to be explored. The regenerator design and dynamics of the FPSE are among the two most important ones. The regenerator is the center-piece of Robert Stirling's invention. It plays a significant role in the performance of the Stirling machine, but the systematic design of the regenerator has not yet been fully developed. Also, without an accurate model of engine dynamics to capture the coupling between machine operation and thermodynamics, the potential of the FPSE can not be realized. Moreover, Teagan, et al. (1983) pointed out that longer life and higher reliability are two characteristics of Stirling engine performance still needing study. Among the problematic components are piston seals, shaft seals, and high temperature combustor/heater head systems.

The development of the systematic approach to regenerator design using stacked wire screens has been under investigation. Hamaguchi (1991) presented the basic relationships governing the flow loss and heat transfer characteristics of stack wire gauze. Also investigated were the effects of the regenerator size on a two-piston type Stirling engine. Miyabe, et al. (1982) developed a design procedure for wire screen matrix regenerators. The method was verified by the test on a mechanically linked, two-piston Stirling engine. Despite the fact that the flow in the regenerator is oscillatory, most of the work has been based on steady flow correlations. Attempts to study the pressure drop in oscillating flow and in unidirectional flow were made by Chen (1983) and Tiehan, et al. (1989). Tew, et al. (1990) reviewed NASA funded work in understanding thermodynamic losses. He also discussed the criteria on which to base the use of steady flow correlations for oscillatory flow. Guo, et al. (1987) investigated the cyclic flow characteristics through metal screen matrix regenerators. A transfer matrix for cyclic flow in a regenerator was proposed with some experimental results showing the verification. Despite all the design strategies, many investigators found the use of simple steel wool as an effective regenerator in miniature Stirling cryocooler (Walker (1983), Davey and Orlowska (1987)).

Linear dynamic analysis has long been used to analyze the operating frequency and stability criteria for the FPSE (Benvenuto, et al. (1989), Cichy (1984), Kankum (1992), Kankum, et al. (1992)). For most of these studies, the dynamics of each component was decoupled from the thermodynamics of the cycle. Isothermal conditions in the working space was also usually assumed. Berchowitz and Wyatt-Mair (1979)

presented a closed form solution for frequency, phase, and performance of FPSEs. Their method was verified for the Harwell and Beale machines. Das (1979) performed a dynamic analysis on a mechanically linked Stirling engine and a FPSE used for solar thermal-electric generation. The results demonstrated that the free-piston dynamics can be approximated by second order models where the piston motion has two resonant frequencies. The stability criteria and control strategy via the pressure modulation were discussed. Ackerman (1981) described the use of vector analysis to provide some insights on the dynamics of a free-piston refrigerator. Three simultaneous equations were needed for defining the performance of the machine: 1) the energy equation defining the cooling capacity, 2) mass continuity equation, and 3) the equations of motion. Redlich and Berchowitz (1985) derived the linear dynamic equations and applied them to obtain stability criterion, oscillation frequency, and the relative amplitudes of the dynamic components. The method was applied to Beale's machine, Harwell's thermomechanical generator, and a free-cylinder engine. Benvenuto, et al. (1990) presented a dynamic analysis algorithm for piston-displacer FPSE and established the stability criterion for operation. The method was applied to optimize the machine for stable dynamic behavior and to increase engine efficiency. Berchowitz (1988) and Benvenuto, et al. (1991) utilized the linear system analysis with control theory to describe the response to load of the FPSE. Also studied was how the nonlinearity of the displacer and piston damping helps to ensure stable operation. Berchowitz (1988) demonstrated how the response to the source temperature rise initiates the system instability which eventually gives the self-starting character to a well-designed FPSE. A majority of these past investigations studied

the popular piston-displacer configuration. The dynamic analysis of the free-piston refrigerator with a two-piston configuration can be found in De jonge (1979).

Besides the thermodynamic design, many mechanical features of the cooler must be carefully considered to yield superior performance and long operating life. Beale, et al. (1973) described many of these mechanical features including bearings, gas dampers, displacer guidance as well as lubrication and piston position stabilization. Gas seals were also discussed. Davey and Orlowska (1987) described the design and construction of a miniature split Stirling refrigerator. Their instrumentation and the operating procedure were also presented.

Many of the past experimental investigations provided insights into the machine operation. Agbi (1973) studied the effects of charge pressure and the type of working fluid on the Beale-type FPSE. De jonge (1979) performed tests on a Stirling refrigerator driven by an electrodynamic drive to verify an analysis procedure based on system dynamics. Dochat, et al. (1980) tested a fully-instrumented FPSE/linear alternator. The dependencies of power output, and efficiency on heater head temperature were also presented. Azetsu, et al. (1984) described the performance testing of a two-piston Stirling engine. The effect of phase difference on engine performance was discussed. Also, Three different working gases–helium, argon and neon–were tested and compared. Instantaneous pressure variation in the piston was presented and discussed in relation to engine performance. Orlowska (1987) and Bradshaw, et al. (1986) performed energy balance measurements on a two-piston, two-linear motor driven Stirling refrigerator. In their study, major sources of energy losses were described quantitatively using an analysis

of the experimental data. Also presented in Bradshaw's work and Orlowska's work were static and dynamic heat load variations with the cold-end temperature and the displacer amplitude, respectively. Further investigations on Stirling machine energy balances can be found in the work by Thirumaleshwar and Subramanyam (1986a and 1986b) as the method was applied to a Gifford-McMahon cycle cryocoolers. Otaka, et al. (1993) from Toshiba corporation, and Kim, et al. (1993) from Gold Star Co. Ltd. examined the performance of small Stirling cycle coolers developed for home appliance applications. In Otaka's work, P-V diagrams were evaluated for the estimation of work and cycle coefficient of performance (COP). A heat balance diagram was also presented. Kim, et al. (1993) investigated the effects of various parameters including speed, charge pressure and heat source temperature on the overall performance of a Stirling cooler. Martini (1984) reviewed many experimental studies and pointed out the need for fully instrumented machines to verify increasingly complex designs and simulation methods. Suggestions on the instrumentation and measurement technique were provided.

Finally, many works provide an excellent basis for the analysis of FPSE. Among the best known are West (1986) and Reader and Hooper (1983) in which basic principles and applications of Stirling engines were described. Martini (1975) gave a simple isothermal analysis on the Stirling engine which involved an analysis of both the heat exchanger and regenerator. Vincent, et al. (1980) presented an analysis that combined linear dynamics with thermodynamics. Walker (1989) provided depth to the description of the Stirling concept especially when it is applied to cooling electronic components. More specifically on FPSEs, Walker and Senft (1985) gave a detailed mechanical and

dynamical description of FPSEs. The performances of real engines were analyzed including a free-piston Stirling cryocooler and a liquid piston engine.

CHAPTER 2

BACKGROUND OF STIRLING MACHINE TECHNOLOGY

2.1) Stirling Cycle Machine : History, usage and trends in development

Stirling cycle machine technology is not new. Stirling engines have been used as both prime movers and air liquifiers throughout the 19th century. The name 'hot air engine' was used to distinguish it from the contemporary 'steam' engine. During the late 1950's, Dr. R.J. Meijer at Philips laboratories gave the engine the name 'Stirling' after the original inventor Reverend Dr. Robert Stirling (1790-1878).

2.1.1) Stirling engines: Robert Stirling's invention

Robert Stirling came from a remarkable engineering family. His grandfather was one of the early agricultural engineers, inventing a rotary threshing machine in 1756. After studying at the Universities of Glasgow and Edinburgh (Walker, et al., 1994), Robert Stirling became a cleric while he continued making scientific instruments in his workshop at home. Eight days after Robert Stirling was licensed to preach by the church of Scotland in 1815, he applied for a patent on his hot-air engine with a heat regenerator. The introduction of a regenerator, or economizer as he preferred to describe his invention, is the most important aspect of his invention. The use of regeneration for storing heat during one process and reusing it during another process significantly improved the thermal efficiency of his engine. Robert Stirling and his brother James (a famous civil

engineer at the time) continued working on regenerative power systems for many years but their machines never became a commercial success.

In that period, the Stirling engine and other derivatives served in a variety of applications. The power ranges of these early engines were from one quarter to five horsepower units. Later, larger engines were installed in ships with power outputs of 224 kW (Walker, et al., 1994). The engines were characterized as big, heavy, and slow running machines. However, they proved less prone to explosion compared with steam engines and gave better reliability and fuel efficiency. These advantages made the Stirling engines a viable alternative to the steam engines.

However, after the mid 19th century, the emergence of much better and cheaper alternatives–internal combustion engines and later electric motors–virtually eliminated the worldwide production of the air engine.

2.1.2) Revival of the engine: the Philips research

A significant revival of Stirling engine research was started by Philips Electric Company, Eindhoven, Netherlands in 1946. The initial effort of the Philips company was to develop a closed cycle hot air engine for small electrical generators to replace heavy lead-acid accumulators used in vacuum-tube radios at the time. Unfortunately, due to the diminishing market, the generator set developed was in production for only a few hundred machines. The success in the development and the significant of the research work on Stirling engines, however, was recognized by Philips researchers and the effort had been continued.

Research on larger engines was further pursued by Philips. The Stirling engine turns out to possess favorable torque characteristics and quiet operation that is well suited for ship propulsion. The license between Philips and General Motors (1958-1970) and later with Ford in the 1970s, also demonstrated the potential of the Stirling engine as automotive power plants. Its potential for high efficiency with low emissions was the main incentive for the development.

The Stirling engine also found use in the solar energy field. A practical system was first developed in the 1960s and was packaged as a solar thermal conversion system (Walker, 1980). It cames as a module combining an engine and a parabolic tracking dish. The dish concentrated the sunlight onto the heater portion of the engine. The power produced from the engine was used either to generating electricity directly or pumping water. In the solar energy area, both kinematic and free-piston machines were used. Power ranged from a few kilowatts up to 50 kW. One of these systems, a 25 kW-electric system, achieved the world record net solar-to-electric conversion efficiency of 29.4 % (Mancini, et al., 1994).

Small free-piston Stirling engines have well proven reliability giving freedom from maintenance. Self starting and fully enclosed, the small FPSE is particularly suited for remote power generation in rural areas. Low grade fuel such as rice husk or biomass is abundantly available for burning as an external heat source. A thermomechanical generator using a diaphragm power piston and suspension spring to eliminated many moving parts. Sliding and static friction was also reduced. The generator has operated for more than 10 years with no failure or maintenance requirements (Walker, 1980).

Even in the medical field, compactness and the ability to use an external heat source made the Stirling engine a viable choice for artificial heart power. The development started at the McDonald Douglas company in the mid 1960s and later at the University of Washington. With module efficiency of more than 25% at power levels of 5 watts, an engine demonstrated maintenance free operation for more than 4 years (West, 1986). The quiet operation of the Stirling engine would allow a patient to live as normal a life as possible.

2.1.3) Stirling coolers

The reversed Stirling cycle for refrigeration production was first proposed by John Hershel in 1834 for ice making applications. In 1874, the Scottish engineer Alexander Kirk published his work on Stirling cycle refrigerators. His refrigerator reached about 214 K with air operating between 1 and 2 atmospheres. For the commercial market, the Stirling cooler was first introduced as small air liquifiers in the 1950s (Chen, 1988) as a result of the Philips research and development program.

It was noted in a paper found in the Philips Technical Review (Kohler,1954) that, "A hot air engine suddenly deprived of heat from its burner, but kept in motion by an electric motor, functions as a refrigerator." Under these conditions, the expansion space simply continues to absorb heat from its surrounding. Without a heat supply, it becomes cold and refrigeration results. In addition to the commercial application of Stirling cycle coolers for large air liquifiers, the technology has found success in the field of miniature

cryocoolers. Stirling cryocoolers are currently used extensively in infrared detectors of night vision equipment and missile guidance systems.

2.1.4) Trends in development

The recent environmental concerns about the use of CFCs in refrigerating machines bring another potential area to Stirling cooler applications. Although the coefficient of performance (COP) of Stirling refrigerators (ideally equals the Carnot COP, practically reaches 45% of Carnot COP) can not match the higher COP (60-70 % of the Carnot COP) of vapor compression machines, environmental concern is a driving force behind the Stirling refrigerator research. Works on near-ambient temperature Stirling coolers have been pursued widely both in the United States and overseas for domestic air-conditioning applications.

Semiconductor electronic devices work faster and with lower noise at reduced temperatures. With commercial success in the area of cooling infrared detectors and missile guidance systems, Stirling cryocoolers are well suited for the cooling of electronic components. In addition, with the recent development of high temperature superconducting materials with transition temperatures between 90 and 100 K, the cooling needs of this application can be met easily with Stirling cryocoolers with minimal additional research efforts. The use of Stirling cryocoolers in this case eliminates the difficulties associated with open cycle liquid nitrogen cooling.

The recent emergence of micromachine technology brought the Stirling cooler in to focus. With the transition from the bulky main frame computer in the 1960s,

microtechnology has brought the concept of distributed information processing which results in much more powerful personal computers. A similar concept of distributed energy processing may help reducing distribution-related losses in energy systems. In some cases, up to 40% of the energy is consumed in ducting system losses and losses associated with central heating and cooling equipment. With the simple construction of Stirling coolers, a miniaturized version might be fabricated in the form of sheet architecture to distributed cooling where it is needed. This concept of a distributed energy system is currently under investigations by Pacific Northwest National Laboratory (PNNL) in Richland, Washington. With the target of 1 watt per cm^2 cooling capacity, one square meter of sheet architecture (10 kW cooling capacity) is sufficient to heat and cool an average house (Wegeng and Drost, 1994).

2.2) Thermodynamic analysis

2.2.1) Ideal cycle: Carnot vs. Stirling

The Stirling cycle is a closed regenerative thermodynamic cycle which serves as the ideal basis for Stirling engine operation. It is however worth noting at this point that actual Stirling engines operate on a much more complicated cycle and should never be termed as Stirling cycle engine (Walker and Senft, 1985). The Stirling cycle, like most power cycles, compresses the working fluid at low temperature and expands it at high temperature. The surplus expansion work is the output power of the cycle. Because the Stirling cycle has isothermal heat transfer processes from and to temperature reservoirs, it

possesses the highest thermal efficiency–Carnot efficiency.

At this point, it is beneficial to look at the Carnot cycle where the Carnot efficiency is based on. The Carnot cycle consists of two isothermal processes and two isentropic processes. For the Carnot cycle, heat is supplied from the high-temperature source reversibly and extracted to the low-temperature sink reversibly through isothermal processes. The process between these two isothermal processes must be reversibly adiabatic; isentropic process in the Carnot cycle. The four processes of the Carnot cycle were illustrated in Fig. 2.1. Areas on the P-V diagram represent work done and areas on the temperature-entropy (T-S) diagram represent heat transfer. Carnot theorem established in 1824 states that the efficiency of all reversible engines operating between the same two temperature levels is the same: Carnot efficiency. An irreversible engine working between the same two temperature levels must have a lower efficiency than this reference efficiency.

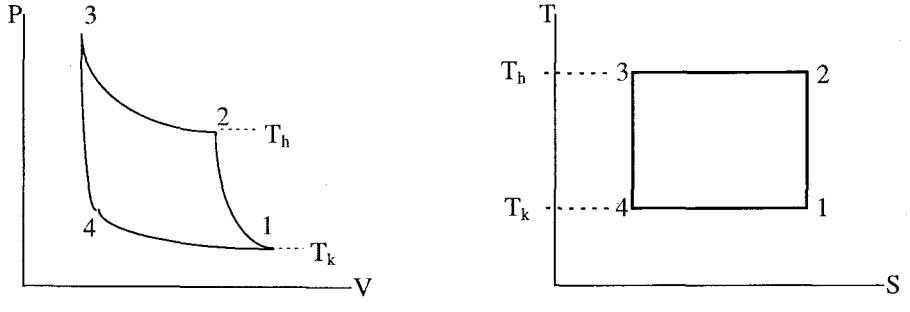

a) Pressure-volume diagram b) Temperature-entropy diagram

Fig. 2.1 Thermodynamic description of the Carnot cycle.

For real gases, such as air, the isothermal and isentropic processes show almost the same amount of slope. This character makes the indicated work on a P-V diagram negligibly small for the Carnot cycle. Regardless of its superior efficiency, extra high pressure or unwieldy long stroke is needed for an engine to provide reasonable work with Carnot cycle. The Stirling cycle replaces two isentropic processes in the Carnot cycle with two constant volume processes (see Fig. 2.2). The increased area on the P-V diagram means more work is available between two temperature levels. Ideally, Carnot efficiency may then be utilized with a decent amount of power output.

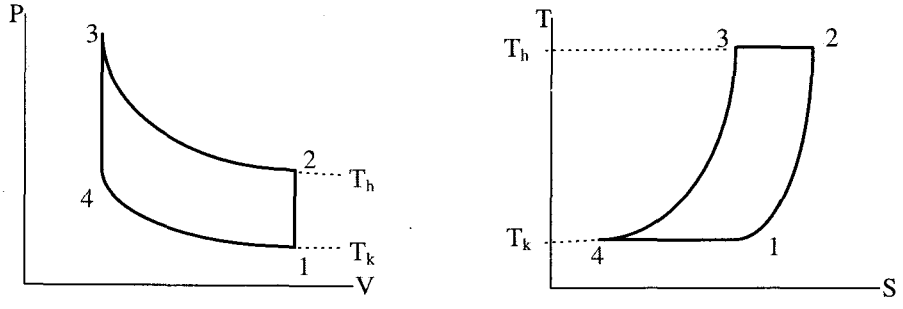

a) Pressure-volume diagram b) Temperature-entropy diagram

Fig. 2.2 Thermodynamic description of the Stirling cycle.

To illustrate physical processes of the Stirling cycle, a basic piston-cylinder arrangement was examined in Fig. 2.3. Firstly, heat was supplied to the cylinder. The fluid pressure increased and the piston was pushed downward: process 1-2. When the bottom dead center position was reached, the heat supply was removed and the cylinder was cooled by an external source: process 2-3. As the cylinder was cooled down, the

pressure decreased. During this period the piston started moving up and compressed the fluid: process 3-4. The cooling process kept in balance with the heating effect from the compression so that the process was under the isothermal condition. When the piston reached the top dead center position, the cooling source was removed and replaced by a heating source: process 4-1.

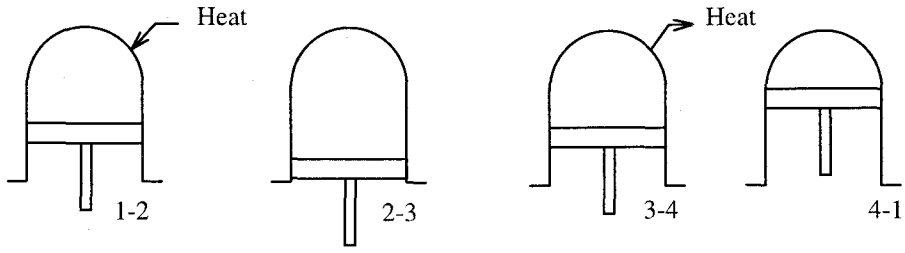

Fig. 2.3 Stirling cycle operation on a piston-cylinder arrangement (adapted from Reader and Hooper, 1983).

It is obvious that with this piston-cylinder arrangement, the way of supplying and removing of heat to the same area–cylinder head–is somewhat cumbersome. The arrangement of the Stirling engine invented by Robert Stirling solves this problem by introducing a displacer in tandem with the piston. The displacer is used to displace thefluid between the stationary hot and cold space. The regenerator stack effectively separates the heat supply area from the heat removal area.

2.2.2) Practical cycle

There are many aspects in which practical Stirling engines behave differently from

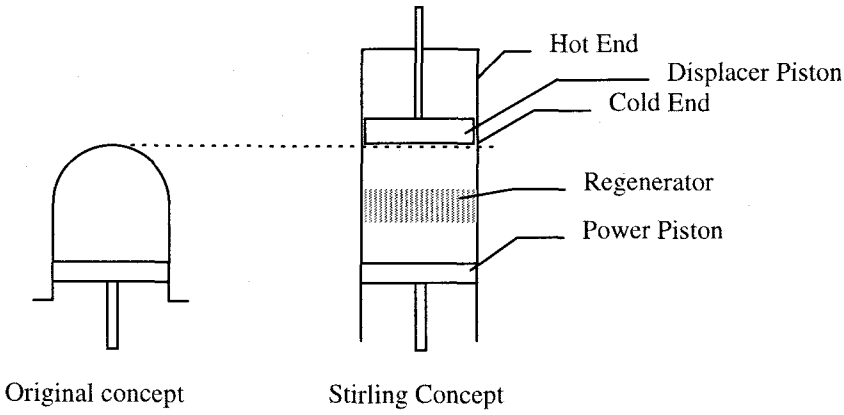

Fig. 2.4 Stirling concept of a displacer piston.
(adapted from Reader and Hooper, 1983)

the Stirling thermodynamic cycle. One of the major differences lies in the way pistons move. In practical cycle, the piston is driven by a mechanical drive in which for a majority of mechanisms results in continuous, sinusoidal motion instead of the discontinuous motion shown in Fig. 2.2. As a result, the actual pressure and volume diagram are reduced to an egg-shape diagram. Therefore due solely to the drive mechanism, available power output for the cycle operating between two temperature levels is reduced from the ideal cycle. This is a principal reason (Kolin, 1984) that makes Stirling engine not possible to operate at low level of temperature difference.

In addition, in a practical Stirling engine, the compression and expansion process do not take place in just one space, but they happen in a separate compression space and expansion space. At least three P-V diagrams result; one for compression space, one for the expansion space and one for the total enclosed volume (without friction, the total

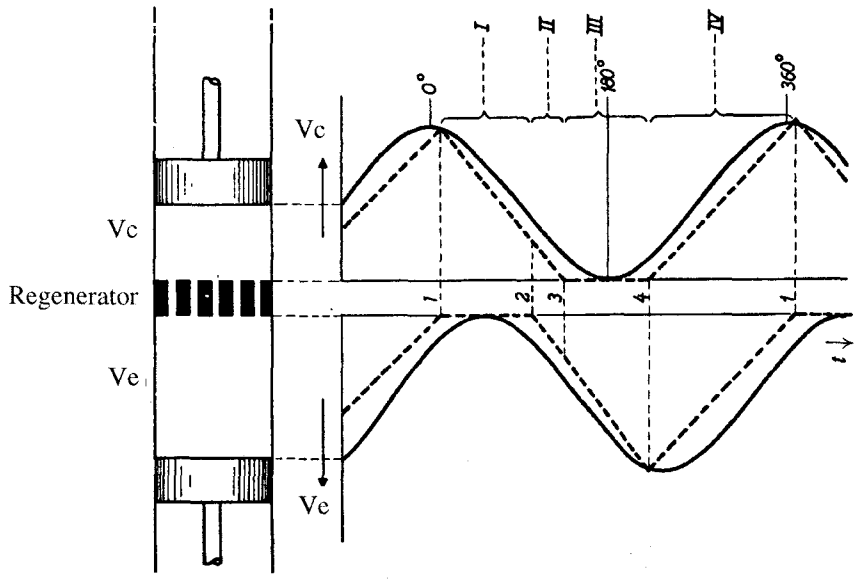

Fig. 2.5 Comparison of the discontinuous piston motion of the ideal Stirling cycle with the sinusoidal piston motion of practical Stirling refrigerators (from Walker, 1989).

indicated diagram area is equal to the expansion space area subtracts the compression space area). Each process is best described by using the two-piston arrangement shown in Fig. 2.6. The compression process takes place when most of the fluid is in the cold space: process 1-2. The cooler extracts heat of compression from the fluid so that the process is under isothermal condition. Next, most of the fluid is transferred to the hot space in a nearly constant volume manner: process 2-3. The regenerator acts like a heat source and supply heat to the fluid. Supplied with more heat from the heater, the hot fluid then expands. The expansion process–process 3-4–gives more work than the negative compression work in the previous step; net work output results. Finally the fluid is returned to the cold space. While doing so, it gives the heat to the regenerator that now performs like a heat sink: process 4-1.

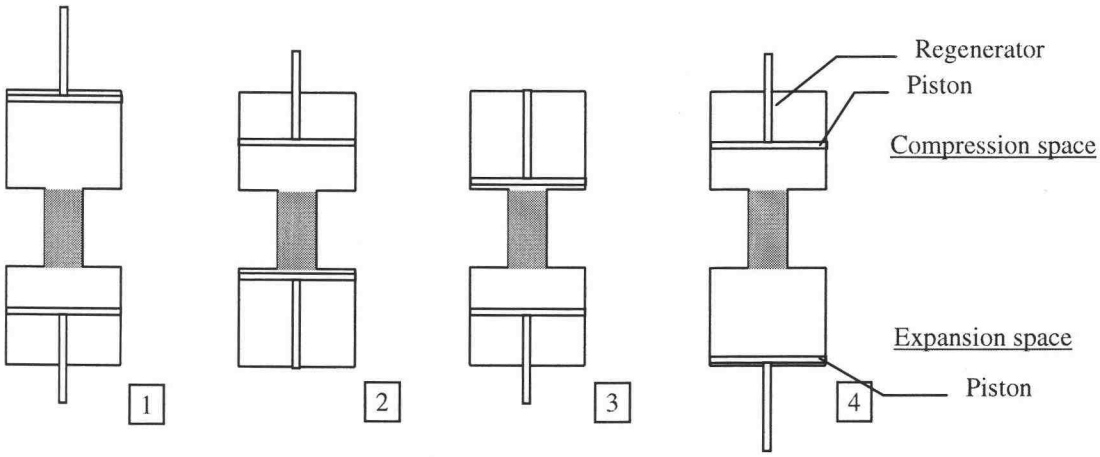

a) Piston motion

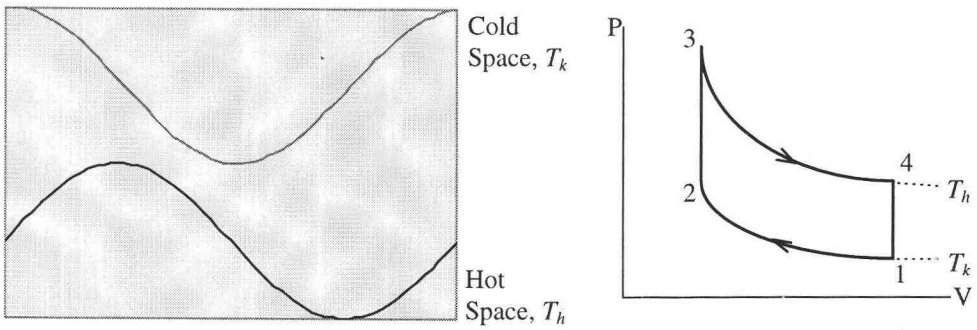

Cold-space volume variation leads
Hot-space volume variation.

b)Associated P-V diagram

Fig. 2.6 Stirling cycle in two-piston arrangement : engine mode of operation.

Eventhough the piston motion is sinusoidal as a consequence of the driving mechanism, the pressure variation generally has a sharper peak and a shallower bottom than a sinusoidal variation. There is also some pressure drop as the fluid is shuttled from the hot space through the heater, the regenerator, and the cooler to the cold space. The result is that the amplitude of the pressure variation in the expansion space will be less than that in the compression space (see Fig. 2.7).

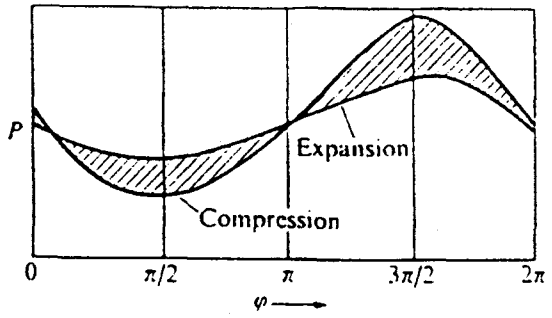

Fig. 2.7 Typical shape of the pressure variation in the expansion and compression space (from Walker, et al. ,1994).

Another departure of a practical cycle from the Stirling cycle is the thermal behavior of the gas in the cylinder. For the Stirling cycle, the expansion and compression occur in isothermal fashion. In practice, operating at high speed, the engine does not allow much time for the heat transfer. As a result, the gas temperature fluctuates in response to the pressure variation. In many situations where the heat transfer is negligible, the gases behave adiabatically. Adiabatic losses arise from large gas temperature variations within one cycle.

2.2.3) The Stirling cycle engine/refrigerator/heat pump

A Stirling cycle machine can operate either as a prime mover, a refrigerator, or a heat pump. No matter in which mode the machine is, however, the direction of heat flow is the same that is from the compression space to the expansion space (Walker, 1980). Only the temperature levels are different between each mode.

Table 2.1 Modes of Stirling machine operation

Mode	Engine	Refrigerator	Heat pump
Location/ Upper temp.level	Heater/ High-material limit	Cooler/ Ambient	Heater/ Elevated temp.
Location/ Lower temp.level	Cooler/ Ambient	Freezer/ Refrigerated temp.	Absorber/ Ambient
Efficiency(Engine)/ COP(Ref./Heatpump)	$\frac{T_{\max} - T_{\min}}{T_{\max}}$	$\frac{T_{ref}}{T_{amb} - T_{ref}}$	$\frac{T_{heat}}{T_{heat} - T_{amb}}$

The operation of a Stirling cycle for an engine is the same as in the case of refrigerator. But in the refrigerating machine, the temperature at the expansion space where the heat is supplied is lower than the temperature at the compression space where the heat is rejected (see Fig. 2.8a). For the comparison between a refrigerator and a heat pump, the only difference lies in the location of ambient temperature (see Fig. 2.8b). For the refrigerating machine, the cooler is at the ambient temperature provided by the availability of cooling water. In case of heat pump, the heat is rejected for heating a room or building at a temperature above ambient while the heat is supplied from atmospheric air or water at approximately ambient temperature.

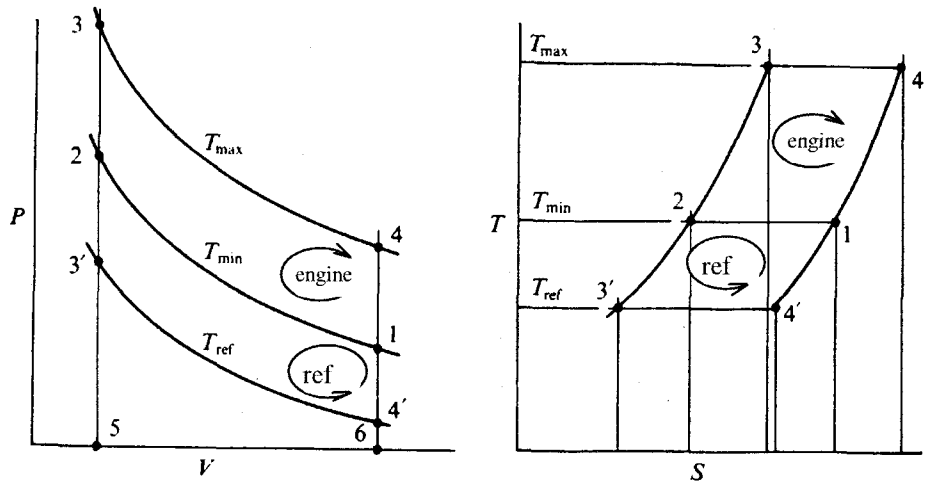

a) The Stirling cycle machine as a prime mover and a refrigerating machine.

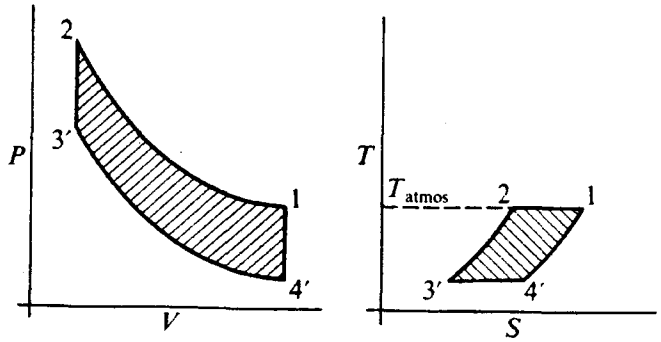

b1) heat pump

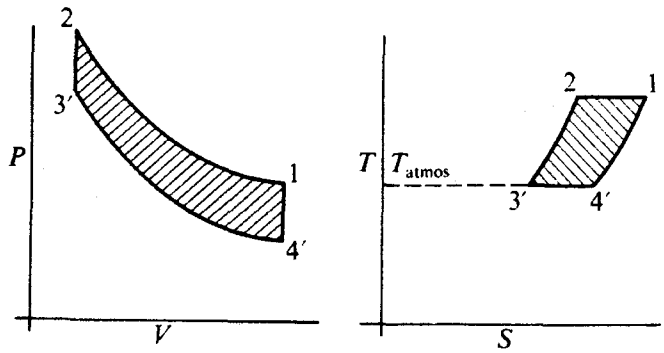

b2) refrigerating machine

b) The Stirling cycle machine as a heat pump and a refrigerating machine.

Fig. 2.8 Modes of operation of the Stirling cycle engines (from Walker, 1980).

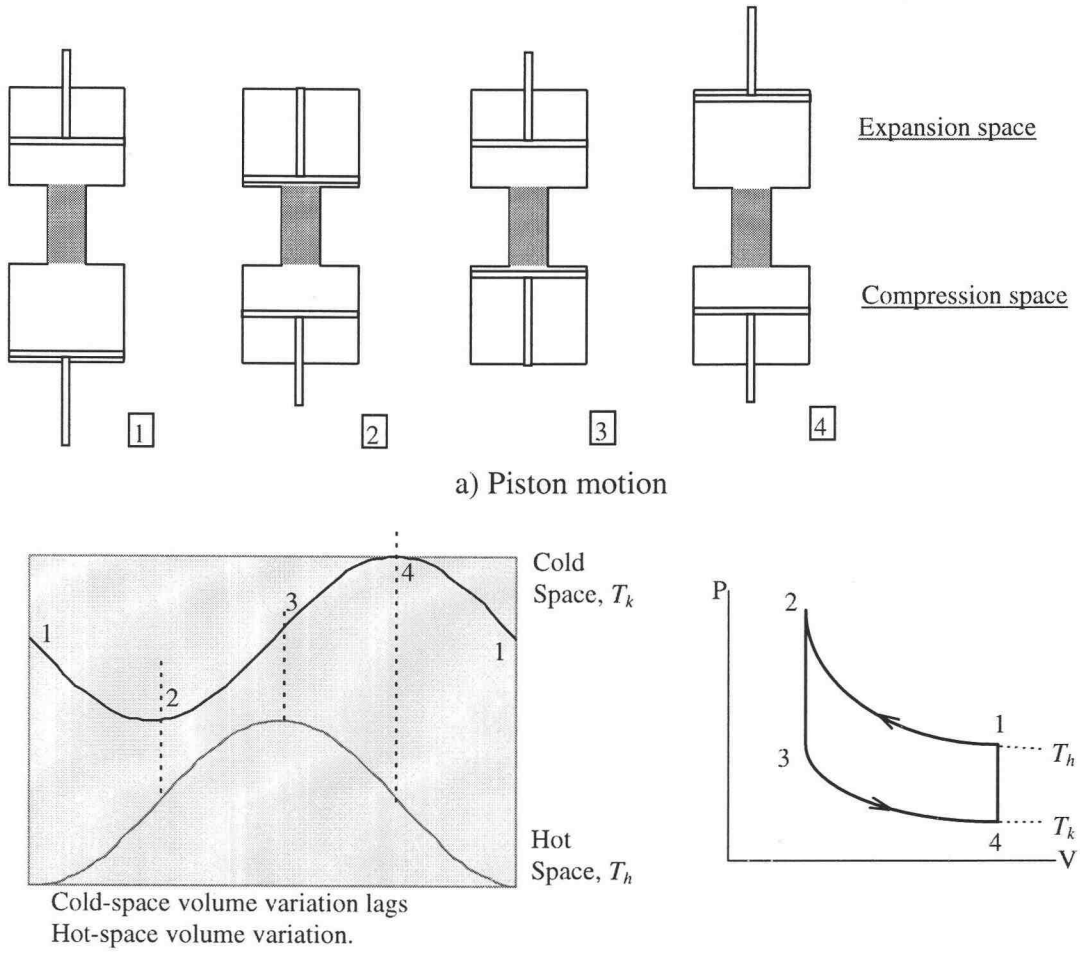

Fig. 2.9 Stirling cycle in two-piston arrangement: refrigerator mode of operation.

2.2.4) Theoretical analysis

Dated back to the time Rev. Robert Stirling had patented the Stirling cycle in 1816, there was no scientific analysis of the machine possible for almost half a decade later. It is more surprising to learn that the Carnot theorem establishing the maximum attainable thermal efficiency and the mechanical equivalent of heat–the foundations for

the first law of thermodynamics–were published by Sadi Carnot and Joule in 1824 and 1849 respectively. Therefore as the development of the Stirling engine continued from the time of invention, the early engineers probably calculated the power graphically (Martini, 1981).

The first analytical prediction of the Stirling cycle was derived by Gustav Schmidt in 1871 based on the assumption that the working spaces are isothermal; so the method was called isothermal analysis. Because the hot and the cold space do not practically behave isothermally, except for small, low pressure engines, the actual indicated power is less than that predicted by Schmidt equation (Martini, 1981). Nonetheless, the Schmidt analysis allows closed form solutions to the performance prediction and then is useful in providing insights in the engine development regardless its inaccuracy. Well established for almost a decade, the Schmidt formula–also known as the first-order analysis–had superseded by the adiabatic model first proposed by Ted Finklestein in 1959.

Formally, there are four levels of analysis available for the Stirling engine performance predictions. Each levels are titled by the level of complexity and expected accuracy. Zeroth-order analysis is the most fundamental. The analysis makes use of the experience data in the preliminary determination of basic performance parameters such as the output power.

William Beale gave an estimation of the power output for the Stirling engine in the form: (Reader, 1983)

$$P = Z \cdot \beta \cdot V_{sw} \cdot p_m \cdot N / 6000 \qquad (2.1)$$

where P = Power output in kW

Z = number of separate thermodynamic cycles

V_{sw} = compression space swept volume, cc

p_m = Mean value of the working pressure in MPa

N = Operating speed in rev/min

β = $0.034-0.052*\tau$, and

τ = cooler temperature(T_k)/heater temperature(T_h, in Kelvin).

This relation is found to be true approximately for the machine of all type and sizes (Martini, 1983) including free-piston type and crank mechanism type.

West (Walker, 1985) took the temperature effect into account in another way,

$$P = F * p_m * V_o * f * (T_h - T_k) / (T_h + T_k) \tag{2.2}$$

where p_m = mean cycle pressure, bar f = cycle frequency, Hz

V_o = displacement of the power piston, cm^3

F = 0.35 in SI unit.

Senft has been able to deduct this form directly from ideal Stirling cycle (ideal cycle gives F=2.0). Thus this formula is applicable to all Stirling engines.

There is no such a correlation for the Stirling refrigerator having capacities of less than 1 kW. However, the experience chart prepared by Strobridge (Walker, 1989) suggests that miniature refrigerators achieve a coefficient of performance based on the available refrigeration of 1 to 5 percent of the Carnot value.

The second level is the first order analysis. It is customarily called the Schmidt analysis as it employ the theoretical analysis derived by Gustav Schmidt in 1871. The Schmidt analysis is essentially a special case of methods called the isothermal analysis in which the compression and expansion of the working fluid is assumed to be isothermal. The cycle described by Schmidt has become the classic Stirling cycle (the detailed derivation of Schmidt analysis can be found in Urieli (1986)). Its sinusoidal volume variation produces the P-V diagram that looks like the actual P-V diagram. The closed form solution makes possible the calculation of the design parameters such as the pressure ratio, the amount of heat required to be supplied and extracted. The analysis also provides a mean to explore the optimized engine configuration for a particular purpose. Notwithstanding all those advantages, the Schmidt analysis is obviously highly idealized. The analysis gives the value of the coefficient of performance equals to those of ideal Stirling and Carnot cycle which is not available in practice.

The second-order analysis employs simple equations such as those available through the Schmidt analysis to determine basic power output and heat input. Various power losses are calculated by simple formula and do not interact with other processes. All losses are then added to the basic heat input to provide the required heat input. A practical introduction to the second-order analysis can be found in Martini (1983).

While the first and second-order analysis assume that all of the working fluid in every part of the machine undergo the same process at each instant, the next level of analysis try to model the actual energy and fluid flows occurring at each locations in the machine simultaneously. In the third-order analysis–also known as nodal analysis–the

working space is subdivided into segments called nodal elements (see Fig. 2.10). Within each node, all properties are assumed constant and a set of partial differential equations is derived in account of the continuity, energy and momentum equations (Ho, 1980). Advanced numerical procedure is required for the solutions of the equations. Although the complexity of the numerical scheme is rather involved, it is the level of analysis resorted as a diagnostic tool and when the detailed design trade-off study is required.

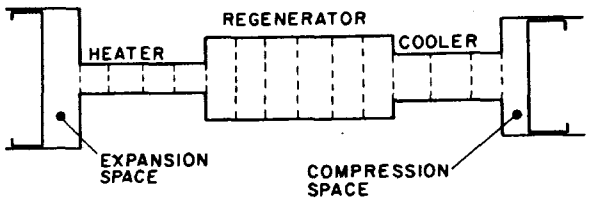

Fig. 2.10 Partition of the basic Stirling engine into cells
(from Walker and Senft, 1985)

CHAPTER 3
RCAS COOLER

3.1) Design and construction

3.1.1) Alpha configuration

Of all five main components of the Stirling engine-compression cylinder, heater, regenerator, cooler and expansion cylinder–three major arrangements were illustrated in Fig. 3.1. In the alpha-type, there are two separate cylinders in which two pistons mutually move in a specific phase shift. Invented by A. K. Ryder, this type of arrangement was used in many early engines (Martini, 1975). Due to its simplified arrangement, it can be assembled into a multiple-cylinder unit giving an extremely high specific output. This advantage was well adopted in later developments of Stirling engines for automotive power plants.

The other two arrangements are of the piston-displacer type. The piston is responsible for the compression and the expansion of the gas while the displacer performs the transfer of gas between the hot and the cold space. The beta-configuration has both piston and displacer in the same cylinder, and it was used by the Stirling brothers in the original Stirling engine. This arrangement is still the choice for most present day engines. Unlike the beta configuration, the gamma configuration has two separate cylinders. The passage needed to link the piston and the displacer cylinder in the gamma configuration leads to larger dead volume. However, there are many applications where the advantage

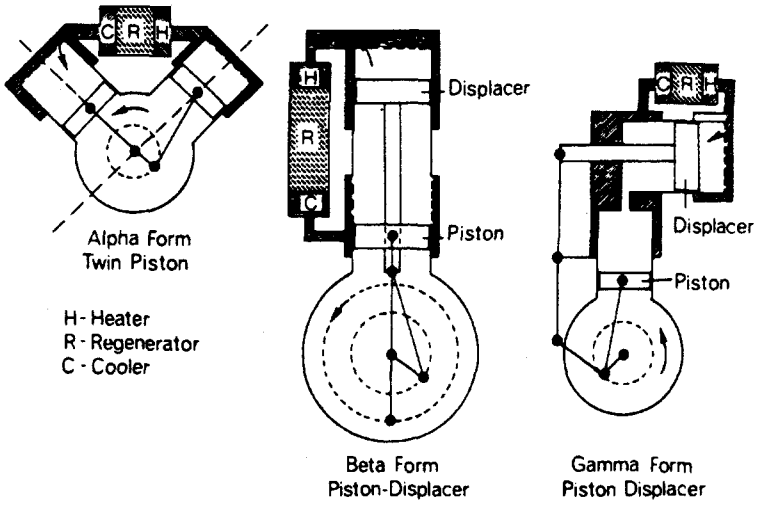

Fig. 3.1 Three major Stirling engine arrangements (From Reader and Hooper, 1983).

of having separate cylinders is preferred to the higher specific output power the gamma configuration offers.

In this development the alpha-configuration was studied. Its simplicity is of prime importance. The two-piston arrangement facilitates the use of steel bellows in place of pistons. As the RCAS cooler operates in the free-piston fashion, the obvious choice is the opposed two-piston configuration. This arrangement also helps minimize the dead volume with higher performance anticipated.

3.1.2) Use of Stainless steel bellows

Stainless steel bellows were used in place of pistons in this investigation. The bellows is made of rippled stainless steel diaphragms welded together circumferentially to

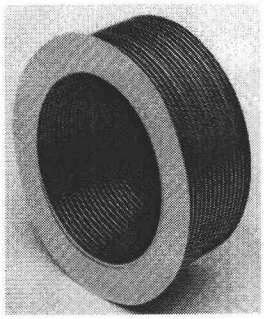

Fig. 3.2 Stainless steel bellows.

form a cylindrical bellow. With limited ranges of compression and extension, long operating life of the bellows is anticipated.

The use of bellows eliminates the problem (in terms of cost and installation requirements) associated with sliding seals. As a result, most of the seals used in this development are static seals. The construction and assembly tolerance are greatly relaxed. Static friction is also minimized.

One problem that arises from the use of a bellows is the lack of guiding rods (available in the form of piston rods in other configurations). This was found to be a problem in the cold-side bellows. When the cold-side bellows oscillates at the resonance frequency, without the guiding rod, the bellows sometimes wobbles rather than oscillates. The cooling effect is deteriorated. Therefore guiding rods were later installed on the cold-side bellows arrangement.

3.1.3) Use of voice coil actuator as a driver

Energy input to the cooler comes from the voice coil actuator to excite the

oscillatory motion of the hot side bellows. The frequency and magnitude of the hot-side bellows motion can be controlled from a function generator and a power amplifier respectively. The function generator feeds a predetermined frequency into the power amplifier. The resulting motion then oscillates at that frequency regardless of the magnitude of the motion. The magnitude of the motion can be controlled by the power level knob on the power amplifier. However, this changes the magnitude when the frequency changes. Therefore, to vary the frequency, some adjustment must be done if constant magnitude oscillation is required. The function generator provides a frequency signal ranging from 2 to 200 Hz. The maximum amplitude of the hot-side bellows is limited by the actuator to 8 mm.

3.1.4) Sealing system

Most of the seals in the cooler are O-ring static seals. With conventional design and construction, this solution was found to provide sufficient sealing performance for helium up to 2 atm. The only dynamic seal is for the driver shaft. The original design used a small stainless steel bellows as a seal. Figure 3.3 shows the construction details of this bellows design. Both ends were sealed with O-rings. Semi-circular split collars were used to secure the flanges of the bellows to the O-rings. The design performed satisfactorily, but it was found later that due to its small size and ductile material behavior, the bellows had its fatigue life that was much shorter than larger bellows used in place of working pistons. (note that in this investigation, the bellows making up the hot

and the cold spaces also failed from fatigue. But the operating life was approximately 2-3 times longer than that of the bellows used for the seal.)

After approximately six million cycles (for 60 Hz operating frequency, this allows only 25 hours of testing), the bellows seal failed: Fatigue cracks formed along the welded seams. The alternative design using tight-fit elastomeric membrane served as a substitute seal and allowed the completion of this study.

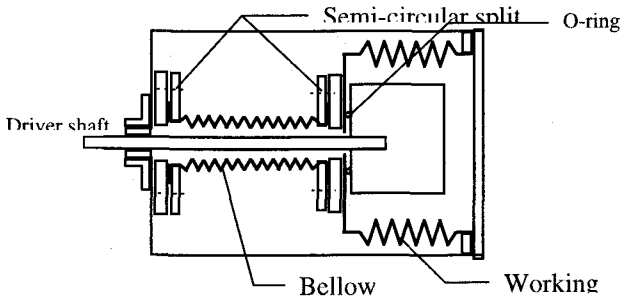

Fig. 3.3 Detailed design of the bellows seal.

The tight-fit elastomeric membrane seal utilizes the combination of a small diameter, high strength shaft and an elastic membrane. A small shaft diameter is needed for minimal axial force resulting from the pressure difference across the membrane. This requirement necessitates the use of high strength material for the shaft to withstand the power transmission from the voice coil actuator to the cooler. A drill blank was used for this purpose and proved satisfactory. A hole in the membrane was needed for the design to work. It had to be of smaller diameter than the shaft. This tight-fitting tolerance provided one step in the sealing. The second step used silicone grease applied to the rubbing surface to reduce the sliding friction and further minimize leakage. The size of

the membrane hole was determined on a trial-and-error basis. A size that gave minimal sliding friction while retaining the sealing performance was employed.

An improved seal design was employed during the later stages of the project. This was because the membrane seal was found to deteriorate with time and could not sustain a number of tests for one operating condition. The improved design used molded silicone sealant. The silicone sealant was pasted into a mold and leaved to set. The molded silicone sealant was then drilled to the size of the shaft. The resulting seal performed satisfactorily for more than 3 tests set and could sustain the pressure up to 2 atm.

Thermocouples were connected from the interior working space of the cooler to the outside readout units. Sealing the signal leads also posed a number of problems. Under pressure, there was leakage through the small passage between the thermocouple wires and their insulation. The epoxy resin used to seal the thermocouple hole did not compatible with the Teflon insulation covering the thermocouple wires. The solution was to cut the thermocouple leads and expose bare wire. The epoxy resin was then applied to the bare wires to form a resin insulation to replace the original Teflon insulation. The thermocouple was inserted through a drilled hole in the cover cooler plate. The hole was finally sealed with epoxy resin. This type of seal performed adequately at the preessure up to 2 atm during this investigation.

3.1.5) Heat exchanger

In the Stirling engine, three heat exchangers of concern: 1) the heater, 2) the cooler, and 3) the regenerator. The design concept of the heater and the cooler are similar

and was discussed in this section. The regenerator design concept is more involved and was covered in the next section. For any heat exchanger, common heat transfer problems exist; larger heat exchangers make the gas temperature approach the wall temperature, but they produce larger flow friction losses and larger dead volumes. Large Stirling engines usually use fins or tube bundles in the heater and the cooler section. Tubes are widely used because the heat fluxes are high and the temperature drop through the wall is manageable. Fins are cheaper but the temperature drop along the fins may not be negligible.

For the cooler, it is usually made from very large number of tiny tubes with water in cross flow (Martini, 1981). For most machine of capacity less than 100 watts, the annular gap between displacer and cylinder suffices for heater, regenerator and cooler (Beale et al., 1973). For example, in the work of Beale et al.(1973), a gap of 0.3-0.5 mm can be used for 80 mm long displacer and a 32 mm bore.

In this investigation, the simple heat exchanger design of a plain cylinder wall is chosen. There are many ways to improve the heat transfer between the gas and the cylinder wall. The usual approach is to increase the heat transfer area; one example is the adoption of very short stroke and shallow cylinder. In this investigation, the heat transfer is improved by another method: an increase in the heat transfer coefficient. The extension and the compression of the rippled bellows results in an air jet in the shape of a ring. This form of jet emerges from the wall of the bellows and give rise to swirling flow of the working gas inside the bellow structure. The plate directly in contact with the bellows is made of copper to promote the heat conduction. The cylinder wall next to the bellows is

made of aluminum for the same reason. Acceptable heat transfer performance is therefore anticipated by using the steel bellows.

3.1.6) Regenerator

A regenerator is an energy storage heat exchanger that acts as a temperature barrier between the hot and the cold space. It is typically a porous mass of finely divided material alternatively accepting and rejecting heat to and from the working fluid (Walker, 1983) so that the heat removed during the constant volume cooling process is not lost and internally transferred to the constant volume heating process. In case of engines, the reduced regenerator effectiveness results in an extra heat load placed on the heater along with the increased cooling load burdened on the cooler. The regenerator was invented by Robert Stirling as a part of his original patent in 1816. The inclusion of the regenerator significantly improved the efficiency of his engine.

Although the regenerator seems to perform simply like a thermal sponge, the process of regenerative heating and cooling is extremely complex. Moreover, if the time interval between flow direction reversal is short enough, there may be no particle ever passes right through the matrix. Instead particles drift from one local region to another in oscillatory fashion. This type of flow is thus called 'tidal regenerative flow' (Walker, 1983). It is little understood and there are no well established heat transfer or fluid flow correlation. Extensive research has continued to gain understanding in this type of flow.

The design of the regenerator matrix is a trade-off between pumping, thermal and dead volume loss. The regenerator performance depends on the choices of optimal

geometry, porosity, size and weight. Martini (1975) showed that a suitable parameter to evaluate the regenerator matrix is the product of the Prandtl number and the Stanton number divided by the friction factor–*PrSt/f*. The higher *PrSt/f*, the better the matrix. For wire mesh regenerator matrices, the turbulence induced may seem beneficial for heat transfer but the turbulence decays not only at the wall but within the fluid. This decay is not useful in the transport of heat but a significant source of entropy generation (Colgate and Petschek, 1994). The result is obvious from the fact that conventional beds of wire screens (0.6-0.8 porosity) possess *PrSt/f* value of just 0.06-0.12 (Martini, 1975). The bed of packed spheres are less advantageous with a lower *PrSt/f* value of 0.05. The triangular, square and circular flow passages give the *PrSt/f* values of 0.22, 0.26 and 0.27 respectively. The best form of the flow passage is the slot. It offers the *PrSt/f* value of 0.29, 0.32 and 0.34 for the slot of length per width ratio equals 4, 8 and infinite respectively. Since hydrogen, helium and air all have Prandtl number of approximately 0.7, they are equivalent in regenerator design. However, in the heater and the cooler, high thermal conductivity of hydrogen or helium is beneficial.

Various geometry of regenerator matrices was tried in past investigations. One example of slot regenerator can be found in the work of Heiden and Reich (1991) on small cryocoolers. The gap between the displacer and the cylinder is employed as a regenerator. With the radial clearance of 30 micron, the regenerator surface is enlarged by making grooves of 0.1 mm width and 4 mm depth. The cooling performance appears to be satisfactory. Annular regenerators are sometimes favored for larger Stirling cryocoolers for they allow the use of materials having lower cost than fine wires.

Materials used include fine straws arranged coaxially with the cylinder. A ribbon of fine stainless steel shim, lightly corrugated or die-formed, may be wound in a helical coil to fill the regenerator space. Both straws and crimped helical coils provide very fine passages with laminar gas flow and high rates of heat transfer. Remarkably high regenerator performance were observed in some machines with straw and crimped coil regenerators (Walker, 1983).

To reduce the conduction heat loss while maximize the effectiveness, the regenerator should have infinite thermal conductivity in the radial direction and zero conductivity in the axial direction. This requirement may be closely reached with stack of woven wire cloth disc (Walker, 1989).

Temperature swing in the regenerator matrix is another consideration for reducing losses. As heat is stored and recovered, the temperature of the regenerator matrix changes. Consider a stainless steel regenerator matrix of 3 kg mass and the specific heat at the regenerator operating temperature of approximately 500 J/kg C; the total thermal capacity is 1500 J/C. For example at 66.7 Hz, with a heat flow of 600 kW, the regenerator must store and return 600000/66.7 or 9000 J in each cycle. So as the heat is stored and removed the regenerator temperature will raise and fall by 9000/1500 or 6 C. For cooler/heater temperature difference say 700 C, such variation will reduce the regenerator effectiveness by 6/700 or 1% (West, 1986). Therefore, although the volume of regenerator can be changed by changing matrix porosity, sufficient amount of material relative to gas mass should remain in order to limit the temperature swing and the ensuing loss (Vincent, 1980).

Flow friction in the regenerator gives rise to both the pressure difference and the phase lag of the pressure characteristic in the expansion space compared with the compression space (Walker, 1983). Made from a stack of wire screens with a pore size of 100 micron, a typical regenerator performs with a peak Reynolds number in the order of only 100. In such a case, the regenerator pressure drop is approximately proportional to flow rate (West, 1986) as would expect for laminar flow. Guo et al. (1987) experimented on metallic screen regenerators and showed that the amplitude of the pressure drop has an extremum at certain frequency while the phase shift is monotonically increased with the frequency.

The dead volume associated with the regenerator is also important. It does not affect efficiency but reduces cooling power in case of refrigerating machine. The larger dead volume fraction, the more gas must be processed by the regenerator to attain a given performance. Higher gas temperature means there is more mass of gas in the void volume and the overall pressure ratio is reduced (Louie and Radebaugh, 1984). In the cryogenic application, the dead volume is even more critical because average regenerator temperature is much lower than compression temperature.

In practice, Walker (1983) suggested that the matrix of 5 cm long is adequate to sustain the temperature difference ranging from 70-320 K. There are wide ranges of choices for the matrix materials. Woven wire clothes of copper, phosphor bronze or stainless steel wire of 0.025 mm diameter with mesh densities of 200×200 strands/cm were found effective in miniature Stirling cryocoolers with helium as the working fluid

(Walker, 1983). Fine mesh of wires is used at the cold end, coarser mesh is used at the warm end to limit the pressure drop through the regenerator (Davey and Orlowska, 1987).

3.1.7) Parasitic losses

Two types of losses are constituted to the reduction of the cooling capacity of the cooler–static loss and dynamic losses. Static loss is primarily the conduction heat loss occurs along the wall, porous matrix of regenerator and electrical leads coupled to the sensors. Combination of material selections, minimized heat flow paths and use of contact resistance help reducing conduction loss. Dynamic losses consist of shuttle heat loss, hysteresis loss, fluid friction loss and imperfect heat transfer loss. Shuttle heat loss is a combination of conduction and convection plus radiation heat transfer to a minor extent. It depends primarily on the thermal conductivity of the gas, length of travel of the piston and time allowed for the heat transfer to occur. With helium as the working fluid, the shuttle loss may become very significant because helium is an excellent heat transfer fluid (at 300 K, the thermal conductivity of helium is 6 times that of the air). In this RCAS arrangement however, the use of stainless steel bellows in place of closed fitted piston and small bellows motion should significantly reduce the shuttle heat loss. Thermodynamics irreversibility during heat absorption and rejection can be estimated implicitly by integrating the work performed over a cycle. From the measurement of pressure variation in the working spaces, the pressure drop loss can also be quantified.

3.1.8) Pictorial description of the RCAS cooler construction

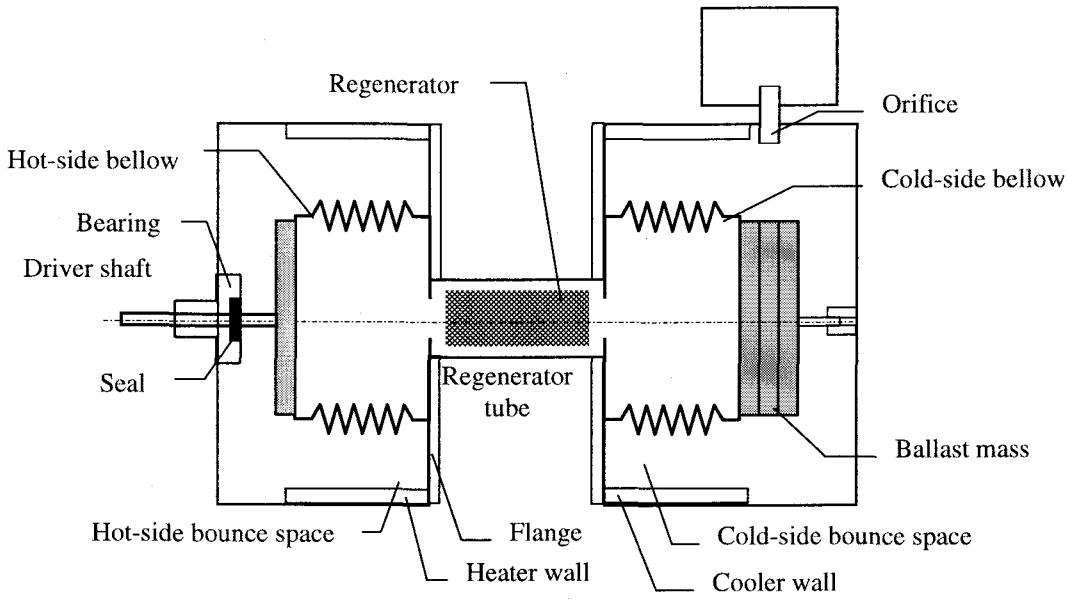

Fig. 3.4 RCAS cooler construction.

3.2) Experimental parameter optimization

3.2.1) Taguchi method

In this investigation, besides the study of the frequency and phase response of the RCAS design, another objective was to produce measurable cooling effect. The best approach to accomplishing this is through the variation of the design parameters until optimal cooling effect is reached. The problem arises when there are many factors affecting the performance of the machine–both thermodynamics and dynamics of motion. To make the cooler performs best under these influences, optimization must be performed.

In the optimization procedure, if the functional relationships between the factors under consideration are known, a parametric optimization procedure can be brought in. For the type of free-piston machine being studied here, the performance of the cooler depends on the response of both thermodynamics and dynamics. Moreover, many design parameters are specified in discrete fashion. For example, the diameter of steel wool is typically designated as fine, medium and coarse. This qualitative description make the parameter optimization which is based on quantitative values awkward to use. Therefore, the experimental parameter optimization was adopted in this investigation.

The classical approach to experimental optimization is to modify one parameter while keeping all the others fixed. After testing all possible combination of parameters, the set that performs can be picked. This conventional approach consumes considerable time and effort in order to achieve a satisfactory performance goal. For example, with five design parameters with four different levels for each parameter, the optimization requires 4^5 or 1024 experiments. This may take years of experiments in quest for an optimized condition. This approach is a traditional method for scientist and engineers. It is slow, and more importantly, it does not account for interactions between parameters. Better approach is adopted in this investigation–the Taguchi optimization technique.

The Taguchi method is a preferred way to optimize a design because it offers an efficient and systematic way to improve the system. This method is also called quality engineering as it is used in industry to improve the robustness of a system subjected to variabilities in manufacturing and product use. In this investigation, another aspect of the Taguchi method was employed. The use of a specific arrangement of parameters-the

orthogonal array provides sufficient information to determine the effects of design parameters with a minimum number of experiments. The optimum condition can be predicted using analysis of the mean (ANOM).

The basic idea of ANOM is based on the assumed linear combination of the parameter effects on the overall performance of the system. This approach brings down the number of experiments to a reasonable level. For example, the use of an L9 orthogonal array (total of 9 experimental runs) can explore the effect of 4 parameters with 3 levels each. The optimized solution may then be approximated using ANOM. Despite the assumption of linearity, the Taguchi method provides a systematic way of assessing the interactions between the quantifiable parameters.

3.2.2) Problem formulation

The Taguchi method for design of experiments starts with the identification of the ideal system through the parameter diagram (Fig. 3.5). Even though a system is complex and hard to model, the method approaches the problem by thinking of the intended behavior of the system functioning in an ideal manner so called ideal function. The 'signal' as an input to the system is identified. Through the ideal function, the input energy, information, or material is transformed into the 'response' which is a measure of system performance. System behavior is controlled by choices of control factors. Non-ideal behavior is taken into account by noise factors. Deviations from the ideal function are to be measured with response characteristics.

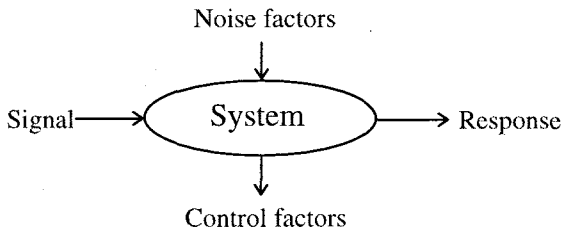

Fig. 3.5 Parameter diagram.

The Stirling cooler under consideration is a two-piston, alpha-configuration operating in the free-piston mode. As the hot-side bellows is driven by the voice coil actuator, pressure variations are transferred to the cold side. This pressure causes the cold-side bellows to oscillate in response with the same frequency but with different phase. The phase and amplitude of motion of the cold-side bellows are a result of the coupled action between dynamics and thermodynamics of the system.

Driven at the natural frequency of the cold-side bellows, the machine will theoretically operate with a 90 degree phase shift between the cold and hot-side bellows motion. Under this condition, the gas will be compressed and heated in the hot-side bellow. The hot gas is then transferred through the regenerator. The gas gives up heat to the regenerator and cools down. Arrived at the cold-side bellows, the gas is expanded and cools down further. After this, the gas is passed back through the regenerator where the heat is transferred back to the gas. The gas is further compressed and heated in the hot-side bellow. This process completes the Stirling cooler cycle.

Driven by the voice coil actuator, the cooler removes heat from the cold bellows and rejects it to the hot bellows residing at room temperature. The ideal function of the

cooler adopted here is to process a given amount of working fluid to produce a cooling effect. Therefore the output of the system can be written as:

$$\text{Cooling Power, } P_{cooling} = mc_p(T_{amb} - T_{cooling}) \cdot \omega \quad \text{watts} \tag{3.1}$$

From the study of free-piston Stirling refrigerators driven by linear electric motor, de Jonge (1979) derived the electric input power to the motor in the form:

$$P_{el} = \frac{V^2}{R_i} + (\omega V y)(B_g l_v \sin\varphi / 2R_i) \tag{3.2}$$

where V = voltage of the source

R_i = resistance of the coil

B_g = magnetic field in the gap

l_v = length of the wire present in the gap

φ = phase shift between piston and applied voltage

and y = the displacement amplitude expressed by

$$y = \frac{B_u V \sin\varphi}{B_c \omega + S_p C_x C_{pd} \sin\varphi_{dr} \cos\varphi_{dr}} \tag{3.3}$$

where B_u and B_c = constant for a given linear motor, φ_{dr} = phase shift between piston and displacer, and $S_pC_xC_{pd}$ = a product of constants of piston area and pressure variation

The V^2/R term in the power input is essentially the Joule heating loss in the motor coil. As a first approximation, with the cooler operating at resonant frequency, the piston displacement would vary linearly with the input voltage,

$$y = kV \tag{3.4}$$

where k = constant for a cooler driven by a linear motor. As a result, the input power to the cooler is given by:

$$P_{ideal} = (\omega V y)(k') \tag{3.5}$$

Substituting into this expression for the displacement yields,

$$P_{ideal} = (\omega V^2)(k'') \tag{3.6}$$

Finally, the ideal function describing the transformation of energy from input to output was the form:

$$k'' \cdot \omega V^2 = mc_p (T_{room} - T_{cooling}) \cdot \omega \tag{3.7}$$

or $$y = \beta m \tag{3.8}$$

where y = the signal factor, V^2

β = the linear proportionality factor of the system, mc_p/k''

m = the response, temperature difference T_{room}-$T_{cooling}$

3.2.3) Choices of control factors and noise factors

After the signal and quality characteristics were given for the ideal function, an attempt was made in listing all factors that affect system performance. This experimental parameter optimization was done as a part of Robust design (ME 519) course at the OSU. Although the noise factors are presented, it should be noted that it is essentially irrelevant in this investigation. Among the parameters generated, the control factors and noise factors are selected as follows.

Four control factors were considered important in this investigation. Two of them concern the regenerator and affect primarily the thermodynamics of operation. The control factors are the size of the regenerator wire and the mass of the wire packed in the regenerator volume. The other two control factors focus on the dynamics of the operation. They are the vibrating mass on the cold-side bellows and the size of the orifice installed on the cold-side bounce space. The mass of the cold-side bellows affects directly to the natural frequency. The size of the orifice influences the damping coefficient of the gas spring-damper in the bounce space. For all four control factors, three levels were investigated which will provide discernable trends of the response. The details on the levels of each control factor were listed on the Table 3.1.

There are three types of noise factors; unit-to-unit, deterioration, and environmental noise. Because the cooler is in development, there is only one machine and no unit-to-unit noise factor is available. For the variation in subcomponents due to deterioration effect, because it is not possible to force the aging effect or to change the

Table 3.1 Control factors

	Control Factors	Level 1	2	3
1	Regenerator wire diameter	fine	medium	coarse
2	Regenerator mass (grams)	1	3	6
3	Ballast mass on cold bellow	1	2	3
4	Size of the orifice on cold bounce space	Closed	Small	Open

deterioration effect, because it is not possible to force the aging effect or to change the component to simulate the aging effect, no deterioration factor will be included. The only noise taken into consideration in this study is the environmental noise. Two noise factors of choice that can be used are the ambient temperature and the initial position of the bellow. The ambient temperature is set at two levels that are the nominal ambient temperature and the lower ambient temperature simulated by blowing compressed air on to the hot-side bellows. The initial position of the bellows affects the total volume of gas to be processed. The nominal setting and extended positions are investigated. These two noise factors are compounded into two levels: 1) nominal ambient temperature/extended position, and 2) lower ambient temperature/nominal position. The first level is supposed to give inferior performance due to the increased total volume of gas to be processed while the increased heat transfer from the hot-side bellows should enhance the second level performance.

Note: The driving frequency is set to the system's natural frequency for each operating point. This is because the free-piston machine normally operates at the natural frequency

of the second piston. Therefore, the driving frequency is not chosen as one of the control factors.

3.2.4) Optimized parameter and fractional factorial experimental array

For 4 control factors and 3 levels, the L9 orthogonal array is applicable. Nine experimental runs were listed with specific setting of control factors shown in Table 3.2. Note that each level of each control factor shows up the same number of times.

At this point, it should be noted that in this investigation, the Taguchi orthogonal array was applied solely for rapid parameter optimization. The method was found later to give satisfactory result. Therefore, to avoid unnecessary complications, the interaction

Table 3.2 Setting of control factors in each experimental run

Control Set	Control Factors				Signal, M1		M2		M3	
	1	2	3	4	Noise1	Noise2	N1	N2	N1	N2
1	1	1	1	1						
2	1	2	2	2						
3	1	3	3	3						
4	2	1	2	3						
5	2	2	3	1						
6	2	3	1	2						
7	3	1	3	2						
8	3	2	1	3						
9	3	3	2	1						

between control factors which were known to present were neglected. The optimized solutions from the analysis of mean were used directly.

3.2.5) Results and optimized solution: Air as a working fluid

The details of ANOM formulation and experimental data are included in the Appendix 1 and 2, respectively. The average effects of each control factor on the temperature difference factor (β) are illustrated in Fig.3.6.

From the average effect of the control factors, the optimized set of control factors was selected. The result is the set of coarse wire, with three grams of regenerator weight, two ballast masses and closed orifice. This came from the additional ANOM on the cold-side temperature (Fig. 3.7). While the ANOM on the temperature difference given above proposed the use of medium wire, the ANOM on the cold-side temperature suggested the use of coarse wire with other parameters the same for lower cold-side temperature. A

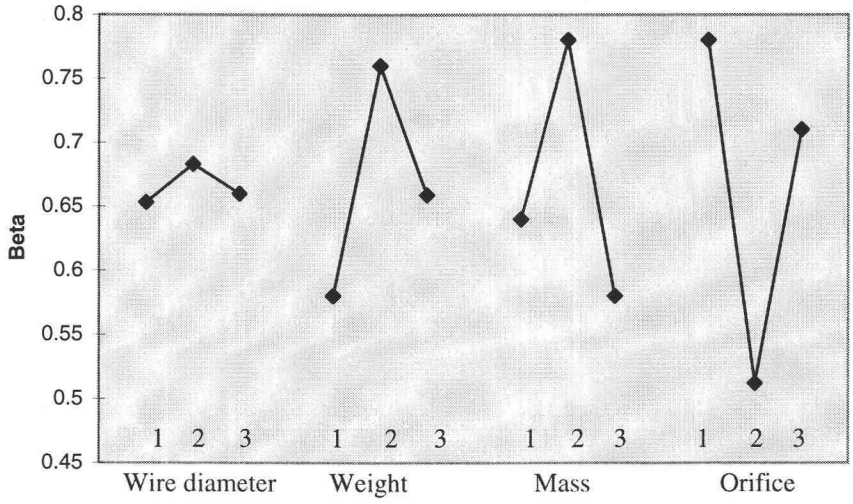

Fig.3.6 Average effect of control factors on the temperature difference factors (for Air). (Note: larger beta, better performance)

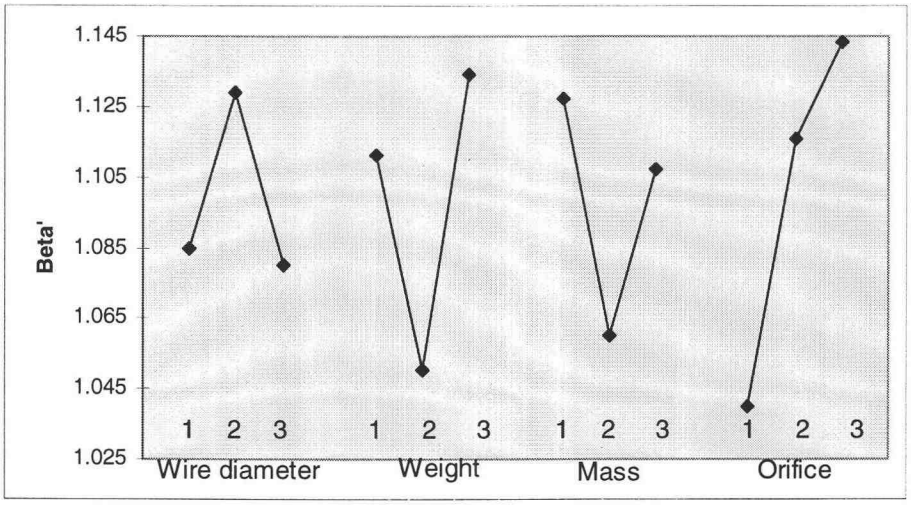

Fig. 3.7 Average effect of control factors on the cold-side temperature factors (for Air). (Note: smaller beta, better performance)

trade-off for a little less temperature difference was made and the choice is the use of coarse wire. The optimized performance in terms of β for the temperature difference was predicted to be 0.912. It should be noted that this set of control factors had never been tested before, but it was expected to give the optimum performance.

The verification test was done on the optimum set of control factors. The resulting performance in term of beta is 0.937. The prediction is quite accurate and the performance improves from a maximum of 0.87 to 0.937, or an 8 % improvement.

In conclusion, for the RCAS cooler operating with air as the working fluid, the optimum set of operating parameters is the set of coarse wire, with three grams of regenerator weight, two ballast masses on the cold-side bellows and closed orifice. This optimum set was used in the investigation of frequency and phase response of the RCAS cooler in the following chapter.

3.2.6) Results and optimized solution: Helium as a working fluid

The experimental data and details of ANOM formulation are included in Appendix 3. Note that in this case, the control factor 4 (effect of the orifice) was not tested because when helium was used the system must be sealed and the application of the damping effect using the orifice was complicated. This effect was investigated separately and also included in Appendix 3.

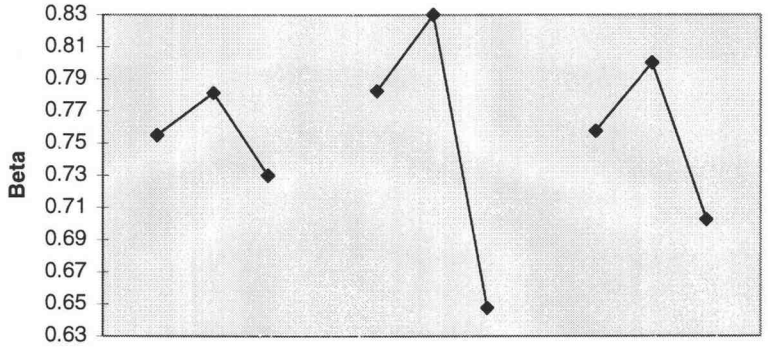

Fig. 3.8 Average effect of control factors on the temperature difference factors (for Helium). (Note: larger beta, better performance)

The results of the helium tests are similar to those for air. From the average effect of the control factors, an optimized set of control factors was selected. The result is the set of medium wire, with three grams of regenerator weight, two ballast masses and open orifice. This came from the additional ANOM on the cold-side temperature (Fig. 3.9). While the ANOM on the temperature difference given above proposed the use of medium wire, the ANOM on the cold-side temperature (Fig. 3.10) suggested the use of coarse

wire with other parameters the same. However, the advantage of using the coarse wire over the medium wire is minimal on the cold-side temperature compared with the loss in temperature difference. The choice is the use of medium wire which is different than that of the previous tests (with air). The optimized performance in terms of β for the temperature difference was predicted to be 0.952 for the optimum control factor setting discussed above.

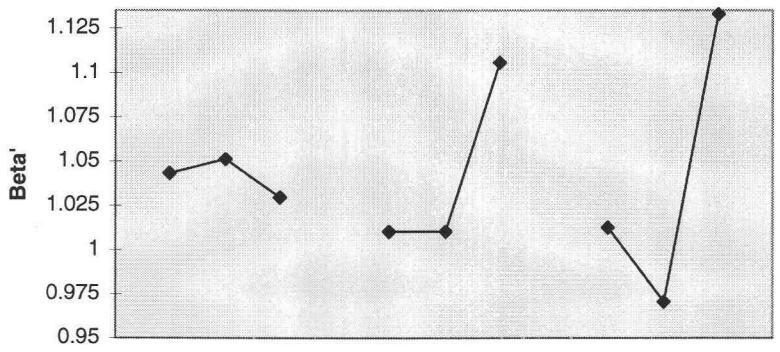

Fig. 3.9 Average effect of control factors on the cold-side temperature factors (for Helium). (Note: smaller beta, better performance)

The verification test was done on the optimum set of control factors. For checking the result, an additional test was done on the setting: medium wire/3 grams/2 ballast mass ($\beta_{predicted}$ = 0.898). The resulting performance in terms of beta is 0.698 and 0.883 for the optimized set and the additional test, respectively. The accuracy of the prediction is quite poor. The trend of the performance is even reversed. The predicted performance for the fine/medium/coarse wire (with 3 grams/2 mass) is 0.927/0.952/0.898 while the test results are 0.834/0.698/0.883. For this investigation, the choice was based on the test

result and the coarse wire was used. Compared with the maximum β of 0.83 found in this test, the improvement on the temperature difference is 6 %.

Additional tests were done on the damping effect of the orifice. In this test, extra coarse wire was tested for its effect on the performance. With the control factor setting of extra coarse wire/3 grams/2 mass and 3 types of orifices: closed/small/large, the results for the temperature difference factors are 0.606/0.524/0.625. The case of small orifice performed worse than the case of no orifice while the large orifice gave almost the same level of performance as in the case of no orifice. The effect of the orifice on the cold-side temperature is also minimal.

Considering the complication of adding the damping element to the cooler with only a small temperature difference advantage (that is from $\beta = 0.606$ to 0.625), the use of the damping element is abandoned in this investigation. Compared with the level of the performance of the coarse wire, the extra coarse offers no advantage. In conclusion, the choice of control factors for the cooler using helium is: coarse wire/3 grams/2 ballast mass.

CHAPTER 4
RESEARCH APPROACH AND EXPERIMENTAL SETUP

4.1) Area of investigation and methodology

4.1.1) Effects of frequency and phase response on the cooling effect.

For a free-piston machine, the displacer amplitude and phase are not restrained by mechanical linkages. They result from thermodynamic/dynamic of motion of the entire machine. The schematic of the RCAS cooler configuration is illustrated in Fig. 4.1. The hot-side bellows motion was controlled by a voice coil actuator. Both amplitude and frequency can be set continuously within the operating range. The cold-side bellows motion however is a result of interactions between the driving force (in form of the expansion space pressure, P_e) and the dynamic conditions (the bellows spring, the gas spring, and the damper).

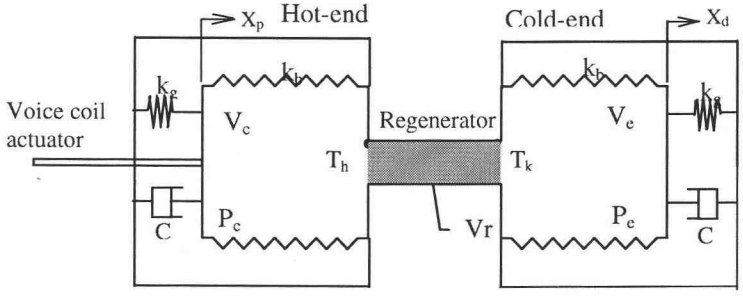

Fig. 4.1 Dynamic representation of the cooler.

The displacement amplitude ratio and the phase shift theoretically varies with the driving frequency in 1-DOF(degree of freedom) mass/spring/damper system.The

amplitude ratio and the phase shift affects the amplitude of the total volume variation and the pressure ratio. The velocity of the gas passing through the regenerator which influences the pressure drop and the phase shift as the gas is shifted from the hot to cold space are also influenced by the amplitude ratio and the phase shift. The resulting pressure variation and the phase shift between the pressure and the displacement variations affect directly the indicated work in the bellows volume. The effects of this frequency and phase response on the cooling effect will be determined.

4.1.2) Enhanced performance by using pressurized helium

Helium is an excellent heat transfer fluid. The Prandtl number and heat capacity ratio, γ, for air and helium at 300 K are approximately the same but the thermal conductivity of the helium is much higher. Enhanced performance of the cooler is therefore anticipated through better heat transfer within heat exchangers. The molecular weight of air and helium are 28.97 and 4, respectively. Therefore, the mass of gas to be cooled is much less in the helium case. Moreover, the ratio of heat transfer to pumping loss is a function of the molecular weight of the fluid. All of these advantages lead to the use of helium.

For the study of system dynamics, the heat capacity ratio hardly changes from helium to air, and the spring constant for linear gas springs remains the same for the similar charge pressure level. Therefore the natural frequency should be the same in both air and helium cases. The phase shift between the hot and the cold bellows are then

expected to be the same when using either air or helium. The difference in the pressure drop and the phase shift of pressure across the regenerator was investigated.

4.1.3) Energy Balance

An energy balance diagram for the RCAS cooler setup is illustrated in Fig. 4.2. On the driver side, the total electrical energy input must be expended into three types of losses: 1) Joule heating in the driver coil, 2) friction loss, and 3) windage loss. The power available after deducting these losses is the power available for the cooler.

$$W_{Electric(-)} - W_{Joule(+)} - W_{friction,windage(+)} = W_{cooler(-)} \quad (4.1)$$

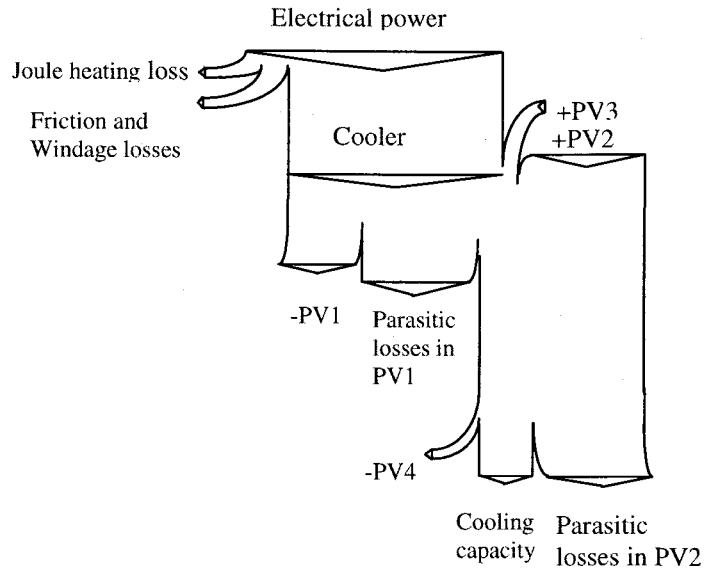

Fig. 4.2 Energy balance diagram.

The total electrical energy input is the product of root mean squared (rms) voltage and current. The Joule heating was estimated by measuring the rms current and the coil electrical resistance when the coil was still hot. The friction and windage loss depend on the amplitude and the frequency of the hot-side bellows motion and also on the working fluid (type, pressure, and temperature). The determination of the friction and windage loss were described in section 4.2.5.

The non-ideal behavior of the gas spring in the bounce spaces results in hysteresis losses. This irreversible loss in both bounce spaces can be quantified by measuring the P-V diagram.

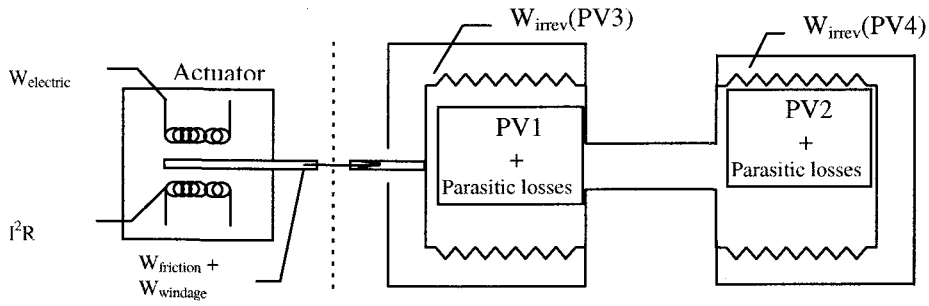

Fig. 4.3 Energy losses on the way from the actuator to the cooler working spaces.

In the Stirling cooler, there are three P-V diagrams that can be constructed; one for the compression space, one for the expansion space and one for the total volume. The P-V diagram for the compression space (proceeds in the CCW direction) indicates the work done by the bellows on the gas (negative indicated work). The P-V diagram for the expansion space (proceeds in the CW direction) indicates the work done by gas expansion on the bellows (positive indicated work). The area of the P-V diagram from the total

volume should be negative and equal to the difference between the area of the positive expansion work and the negative compression work. The negative indicated total work means the input work is required to drive the machine as a cooler.

$$W_{ind,total} = W_{ind,exp(+)} + W_{ind,comp(-)} \tag{4.2}$$

In practice, the flow friction causes the pressure drop as the gas is shifted from the compression to the expansion space. This reduces the total refrigeration available in the expansion space. The total refrigeration produced comes from the P-V diagram from the expansion volume. But the P-V diagram of the total working space may not be available.

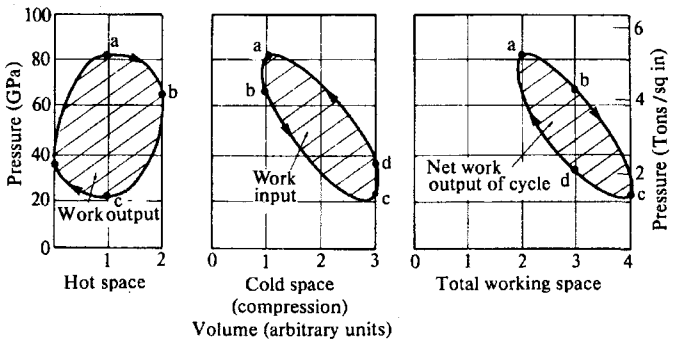

Fig. 4.4 Pressure-Volume diagrams for the working spaces: the case of engine operation (from Walker, 1980).

In the expansion volume, not all expansion work results in a cooling effect. The parasitic loss including static and dynamic losses deducts large portions of energy from the indicated work. Static loss in the form of heat conduction also reduces the cooling effect. Shuttle heat transfer loss comes from the combined effect of heat conduction and

radiation. An additional windage loss occurs as the bellows retracts and extends through the working fluid. The guiding rod for the cold-side bellows also causes frictional losses. Regenerator ineffectiveness gives rise to temperature swing in the regenerator matrix. All of these losses, heat transfer, regenerator ineffectiveness, windage and pressure drop are called dynamic losses.

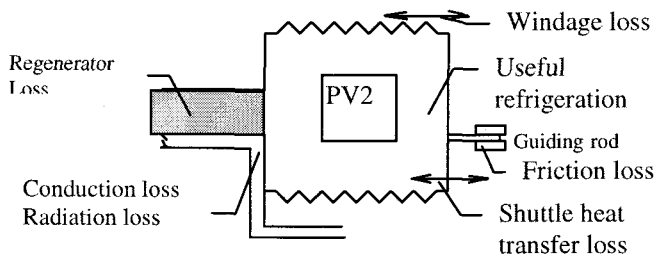

Fig. 4.5 Parasitic losses in the expansion space.

Similar to the expansion space, in the compression space the input power is expended in parasitic losses. The work from the P-V diagram in the compression space is the indicated heat rejection.

$$W_{cooler(-)} = PV1_{(-)} + PV2_{(+)} + PV3_{(+)} + PV4 + W_{parasitic1(-)} + W_{parasitic2(-)} + W_{cooling(-)} \quad (4.3)$$

In this investigation, no attempt was made to determine these losses in detail. The P-V area in the expansion space was used as an indication of the cooling. This work focused on how the frequency and phase response of the cooler affect the cooling performance.

The indication of cooling performance typically used is the COP (coefficient of performance). It is a ratio of the cooling effect to the input power.

$$\text{Cooler COP} = \text{Cooling capacity/Motor input power}$$
$$= W_{ind,exp}/W_{motor} \quad (4.4)$$

In the case where mechanical friction losses are present, it is more informative to indicate the thermodynamic COP which is defined as,

$$\text{Thermodynamic COP} = \text{Cooling capacity/Cooler power}$$
$$= W_{ind,exp}/W_{cooler} \quad (4.5)$$

The COP can be measured against the theoretical limit: Carnot COP. The performance of the cooler studied can also be compared with other cooler design in terms of the COP.

4.2) Instrumentation setup and calibration

4.2.1) Displacement measurement

Two Hall-effect transducers (HET) were employed to measure the displacement of each bellows assembly. The Hall effect occurs when a current-carrying conductor passed through a magnetic field. A HET utilizes this phenomenon to detect the motion of an object by using a small magnet attached to the moving object. The moving magnet

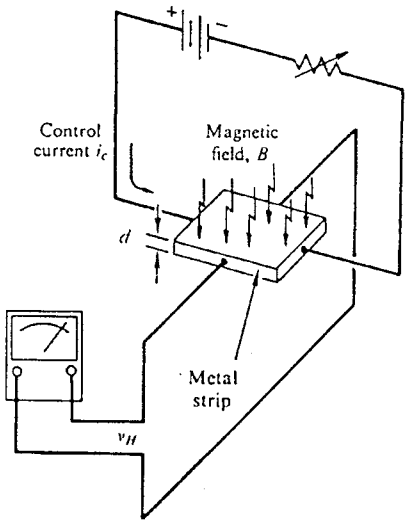

Fig. 4.6 Hall effect transducer. The Hall voltage is $v_H = ki_cB/d$ (k is the Hall coefficient).

causes a change in magnetic field, which in turn, produces a voltage output from the HET. The voltage can be related to the distance travelled by the magnet.

A bipolar slide-by arrangement was chosen where the HET was installed between a pair of rare-earth magnets of different poles as shown in Fig. 4.7. The HET is stationary with the pair of magnets moving with the bellows. A long linear range between the displacement and the voltage readout can be achieved with this configuration and the system can be acccurately and repeatably calibrated.

A HET however responds to all magnetic fields including electronic appliances and the earth's magnetic field. Therefore an AD524 instrumentation amplifier together with a filter circuit were used to reject unwanted signals and raise the output level. The HET circuit used in this experiment was based on an article in the August 1996 issue of Scientific American.

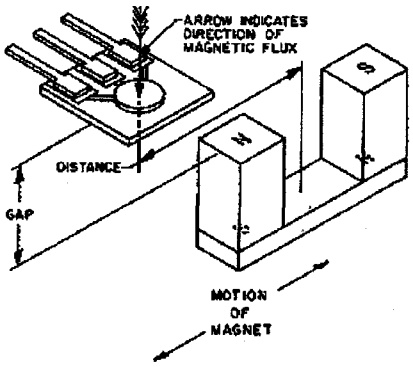

Fig. 4.7 A bipolar slide-by HET arrangement.

The compression bellows was driven sinusoidally by a voice coil actuator, as a result, the motion of the expansion bellows was found to be closely sinusoidal also. The peak value of the voltage signal from the HET was measured in both positive and negative direction. The peak-to-peak value was calculated and the amplitude of the displacement could be obtained from a calibration curve. The time interval between two peaks of the sinusoidal signal gave the actual operating frequency,

$$Hz = 1000\frac{ms}{\sec} / t_{pk-pk}\frac{ms}{cycle} = \frac{1000}{t_{pk-pk}}\frac{cycle}{\sec} \tag{4.5}$$

The HET transducer had extremely high sensitivity and the readout was affected by the relative position of the transducer and the magnets. Therefore the calibration of the HET setup was needed every time the setup was changed. The calibration was done dynamically by limiting the displacement using a physical stop and recording the reading. The HET calibration is described in Appendix 6. For the present setup, the HET gave the displacement direction as illustrated in Fig. 4.8.

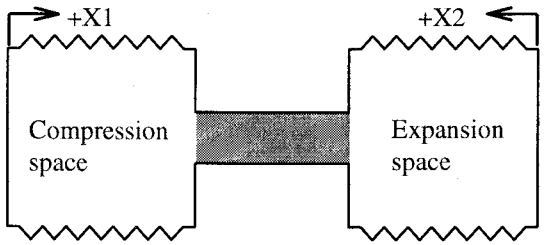

Fig. 4.8 The positive directions of the HET signals.

4.2.2) Pressure measurement

The pressure variations in the hot and the cold end, and also in the bounce spaces, were measured using two silicon pressure transducers. One transducer was installed on the hot side, another on the cold side. Short plastic tubes connected the bellows space and the bounce space with a three-way valve to the pressure transducer port. An AD 524 instrumentation amplifier boosted the signal by 100 times and sent the signal directly to the oscilloscope for readout.

The pressure transducer was calibrated statically with a precision pressure transfer standard from zero to 30 psig. Good linearlity was shown and the average error was no more than 2 percent. The published response time was 1 ms.

The pressure variations in both hot and cold side bellows are not perfect sinusoids. Example plots of the displacement variation compared with pressure are displayed in Fig. 4.9. Only the peak signal in the positive and the negative direction together with the phase difference relative to the hot bellows motion were recorded.

From the calibration curve, the gage pressure value can be obtained from

$$P_g = K_p \cdot mV \tag{4.6}$$

where P_g is the gauge pressure in N/m^2, the transducer constant, K_p is equal to either 61.46 or 60.76 for transducer number 1 or 2, respectively, and mV is the signal output in millivolts.

The oscilloscope, however, displayed the signal in 10 times scale. The actual amplitude of the pressure variation (in N/m^2) was thus,

$$P_g = K_p \cdot V_{pk-pk} \cdot 1000 \frac{mV}{V} \cdot \frac{1}{10} = 100 K_p \cdot V_{pk-pk} \tag{4.7}$$

The phase difference (in degree) was calculated from

$$\phi = 360 \cdot \frac{t_{pk-pk}}{t_{phase-diff}} \tag{4.8}$$

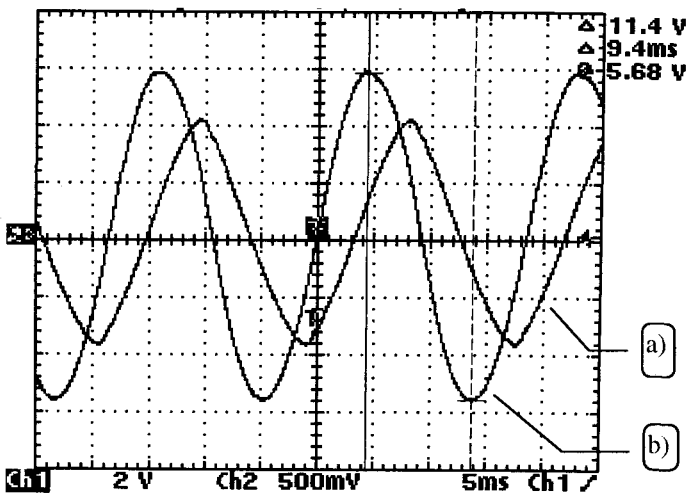

Fig. 4.9 Typical shape of a) pressure variation, b) volume variation.

4.2.3) Pressure-volume diagram area measurement

In general, the sinusoidal variation in the pressure and the volume for a Stirling engine produces an egg-shaped P-V diagram. With the amplitude of both the pressure and the volume variation together with the phase shift between these variations, the indicated work can be calculated. The shape of the pressure variation in the actual working space however, was found to deviate from a perfect sinusoid. These observations suggested that the actual indicated diagram may deviate considerably from an egg-shaped diagram based on the sinusoidal variation in pressure and displacement.

The P-V diagram was displayed on the oscilloscope using the x-y display mode. The diagram was then printed directly for a hardcopy. For the determination of the area of the diagram, it was necessary to digitized the curves manually (Orlowska and Davey (1987), Bradshaw, et al.(1986)).

With the xy-display mode, the displacement signal from the HET went to channel 1, while the pressure signal went to the channel 2. This arrangement resulted in a pressure-displacement diagram that can be interpreted later to be a pressure-volume diagram. The P-V diagram was plotted out as a hard copy and the area of the diagram determined. The indicated area was converted into the thermal work using the following relationships.

With a scale of X mV/division, 1 division in the x-axis corresponds to X mV of the HET signal. In the form of a displacement variation, dX;

$$dX = X \cdot mV \cdot \frac{1V}{1000mV} \cdot a \cdot \frac{mm}{V} \cdot \frac{1m}{1000mm} = \frac{X \cdot a}{10^6} \cdot metres \qquad (4.9)$$

where a is a HET constant available from the calibration curve. For the volume variation,

$$dV = A \cdot dX = \frac{\pi}{4} \cdot (1.637 * 0.0254)^2 \cdot dX = 1.358 \cdot 10^{-9} \cdot X \cdot a \tag{4.10}$$

With a scale of Y mV/division, 1 division in the y-axis corresponds to Y mV of the pressure signal. In the form of a pressure variation,

$$dp = Y \cdot mV \cdot \frac{1V}{1000mV} \cdot c \cdot \frac{N/m^2}{V} = \frac{Y \cdot c}{1000} N/m^2 \tag{4.11}$$

where c is a pressure transducer constant available from the calibration curve. Therefore a square division of the P-V area in the diagram is equivalent to

$$1 \cdot PV = 1.358 \cdot 10^{-12} \cdot X \cdot a \cdot Y \cdot c \cdot (N \cdot m) \qquad \text{or } Joule \tag{4.12}$$

Note that the pressure transducer gave a correct direction of pressure variation. That is the increased pressure was displayed as a positive voltage signal. The problematic signal is the displacement direction. For the P-V area determination, the direction where the pressure and volume is increasing is considered a positive direction.

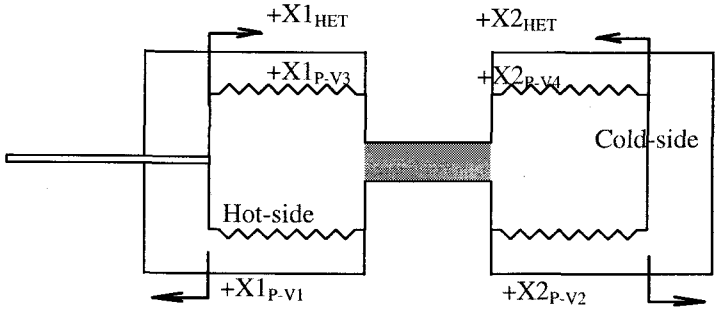

Fig. 4.10 Sign convention for the volume variations.

For the compression volume, the phase difference where the pressure variation (*P1*) leads the bellows displacement variation (*X1*) was given by

$$\phi_{P1/X1} = P1\text{-}X1$$

or $$\phi_{P1/X1} = (P2\text{-}X1)+(P1\text{-}P2) \quad (4.13)$$

where the phase shift term *(P2-X1)* and *(P1-P2)* are the parameters that are easier to measure than *(P1-X1)*.

For the determination of the indicated work, the positive direction of both pressure and volume variation are the direction where the pressure and the volume are increasing. To make the *X1* signal shows the displacement in the increased volume direction,

$$X1_{P\text{-}V1} = X1_{HET} - 180 \text{ degree} \quad (4.14)$$

or

$$\phi_{P1/X1} = (P2\text{-}X1_{HET})+(P1\text{-}P2)+180 \text{ degree} \quad (4.15)$$

For the expansion volume, the phase difference where the pressure variation (*P2*) leads the bellow displacement variation (*X2*) was given by

$$\phi_{P2/X2} = P2\text{-}X2_{P\text{-}V2} = (P2\text{-}X1_{HET})\text{-}(X2_{HET}\text{-}X1_{HET})+180 \quad (4.16)$$

where $X2_{P\text{-}V2} = X2_{HET} - 180$

For the bounce space on the hot-side bellow, because *X1* is already in the direction of increasing volume, the phase difference is simply

$$\phi_{P3/X1} = P3\text{-}X1_{P\text{-}V3} = (P3\text{-}P2)+(P2\text{-}X1_{HET}) \tag{4.17}$$

For the bounce space on the cold-side bellow,

$$\phi_{P4/X2} = (P4\text{-}P2)+(P2\text{-}X2) \tag{4.18}$$

or from (4.16)

$$\phi_{P4/X2} = (P4\text{-}P1)+(P1\text{-}P2)+(P2\text{-}X1_{HET})\text{-}(X2_{HET}\text{-}X1_{HET}) \tag{4.19}$$

The area of the P-V diagram in which the displacement variation leads the pressure variation is noted as a positive value (piston does work on the gas). When the pressure variation leads the displacement variation, the gas performs work (expansion work) on the piston and the area of the P-V diagram is designated as a negative value.

4.2.4) Gas temperature measurement

Type K thermocouples (Chromel/Alumel) were installed on both ends of the regenerator. The thermocouples were connected to a digital thermometer to display the average gas temperature in the compression and expansion bellows. The red wire (NiAl) and the yellow wire (NiCr) were connected to the negative and positive terminals of the digital thermometer, respectively.

4.2.5) Electrical power input measurement

The supply voltage and current fed into the driver was measured by two multimeters. The product of the rms voltage and current gives the electrical power input to the driver. With the measurement of the current and the coil resistance (measured when the coil is still hot after the operation), the Joule heating (I^2R) loss in the driver was measured. Bradshaw (1986) suggested that if the drive current is not sinusoidal, the true rms current meter is needed for the precise I^2R calculation. Therefore all measurements were done with rms multimeters.

$$W_{Electric} = I_{rms} \cdot V_{rms} \tag{4.20}$$

$$W_{Joule} = I_{rms}^2 \cdot R \tag{4.21}$$

The electrical power input is consumed by Joule heating losses in the driver coil, friction loss in the seal contact, and thermal irreversibility in the bounce space. The rest of the power goes to the cooler. The Joule heating loss can be calculated directly from the rms current if the coil resistance is known. The irreversibility loss was determined from the area of the P-V diagram recorded from the bounce space. The friction loss was estimated for each operating frequency and driver side displacement amplitude. This last quantity was determined as follows.

The cooler was driven with a closed regenerator tube so that the cold-side bellows did not move. With this configuration, the cooler produced no cooling effect. The total input power was assumed to be consumed for the Joule heating loss, hysteresis loss and

friction loss. Using the indicated power from the P-V diagram for an estimate of the hysteresis loss, the friction loss could be approximated.

4.2.6) Pictorial description of the experimental setup.

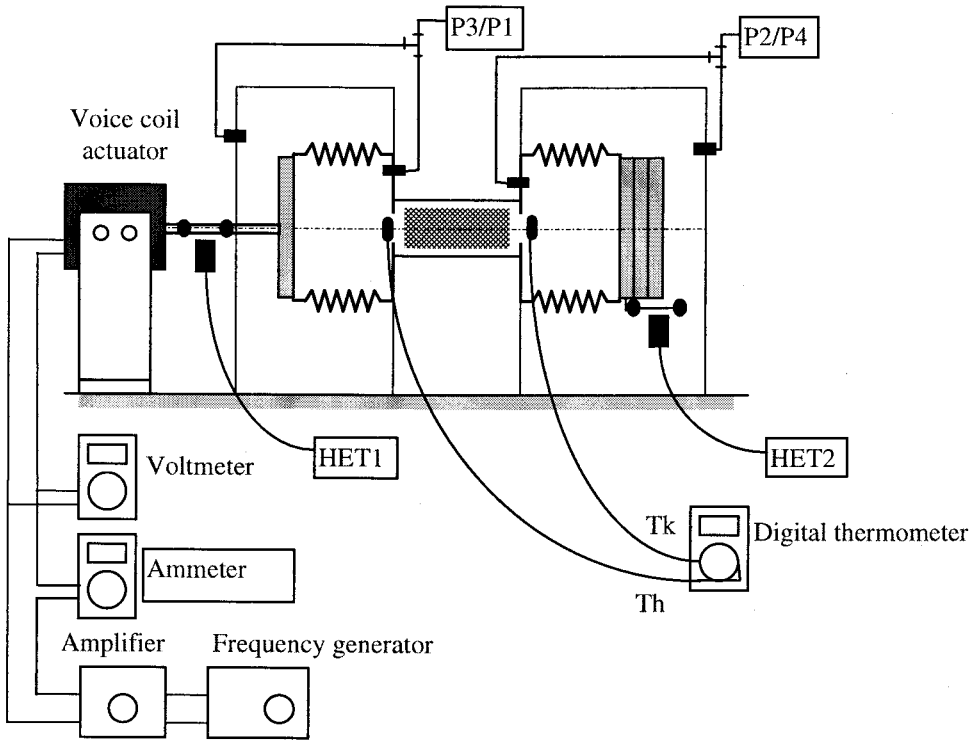

Fig. 4.11 Instrument setup for the RCAS cooler.

CHAPTER 5
TEST RESULTS AND DISCUSSIONS

5.1) RCAS cooler test with air at 1 atm for 3 hot-side bellows displacement amplitudes

5.1.1) Experimental setup

The RCAS cooler was charged with air at atmospheric pressure and room temperature. It was operated with a constant hot-side bellows displacement while the frequency was varied for each data set. Three hot-side bellows displacements were studied, 2.35, 3.25 and 5.5 mm. The amplitude of 2.35 and 3.25 mm were used over the full range of frequencies including the natural frequency where the cold-side bellows amplitude reached its maximum value. The amplitude of 5.5 mm was the maximum possible displacement for the hot-side bellows. However, operation near the natural frequency was not possible for this amplitude because the maximum cold-side amplitude was limited to approximately 8 mm.

For this test set, the displacement measurements consisted of a hot-side HET (*mm=V*1.955+0.522*) and a cold-side HET (*mm=V*0.5271-0.1555*) that were used through all three test sets. Because the elastomer membrane used as a seal deteriorated with time, a new one was used for each data set. The complete data were tabulated in Appendix 8.

5.1.2) Phase shift and natural frequency

With the sign convention adopted in this investigation (see theoretical analysis of the Stirling cycle in section 2.2), cooler operation must have the hot-end displacement (*X1*) leading the cold-end displacement (*X2*). For all experiments described here, this was the case.

The operating frequency (ω) where a 90 degree phase shift occurs between *X1* and *X2* was chosen as the natural frequency, ω_n. For this setup, in all three *X1* settings, the natural frequency was 51.5 Hz. The phase shift ranged from 15 to 160 degrees giving frequency ratios (ω/ω_n) from 0.82 to 1.22. The test data for the cooler without a regenerator matrix revealed that the response of the cold-side bellows follows similar trends. Also, within the experimental uncertainty, the natural frequency was the same. This trend suggested that the phase shift results primarily from the dynamic response of the system.

Some observations should be noted in relation to the natural frequency. Figure 5.2 shows the amplitude ratio as a function of frequency ratio. The amplitude ratios for all three *X1* settings follow the same general trend with the maximum value of 2.5 found at the natural frequency for *X1*=3.25mm. For *X1*=5.5 mm, the test near the natural frequency was not possible due to the physical limitations of the cold-side bellows displacement. For the case of no regenerator, the response of the amplitude ratio had a different shape from the other three cases with steeper peaks near the natural frequency.

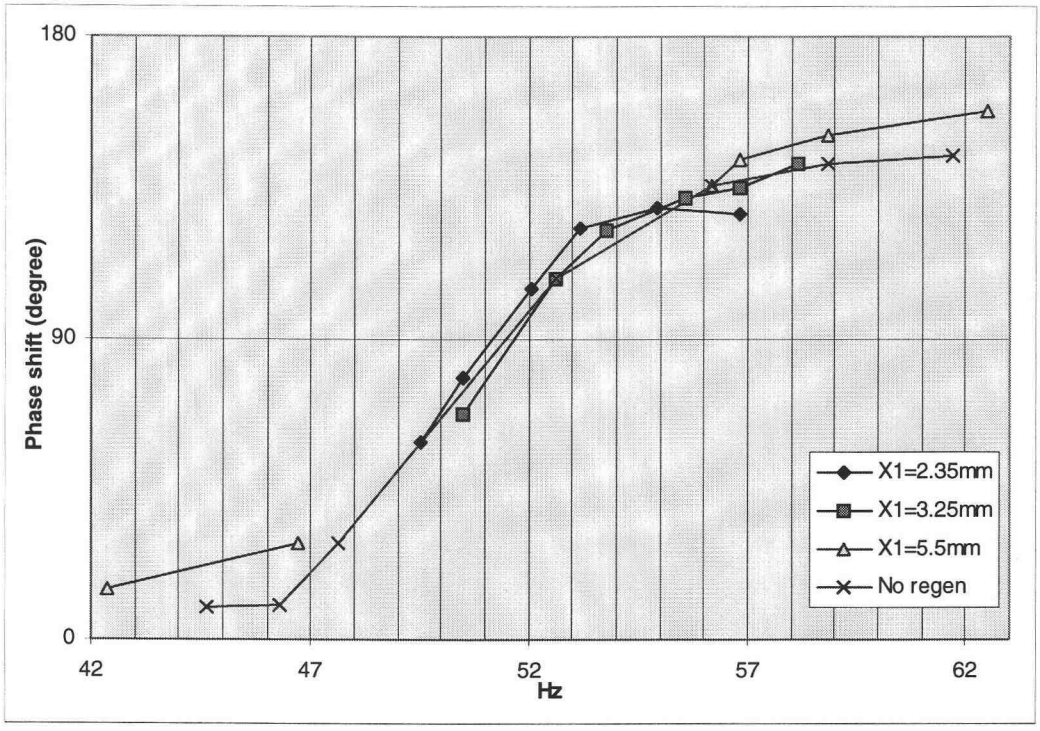

Fig. 5.1 Phase shift that *X1* leads *X2* vs. operating frequency.

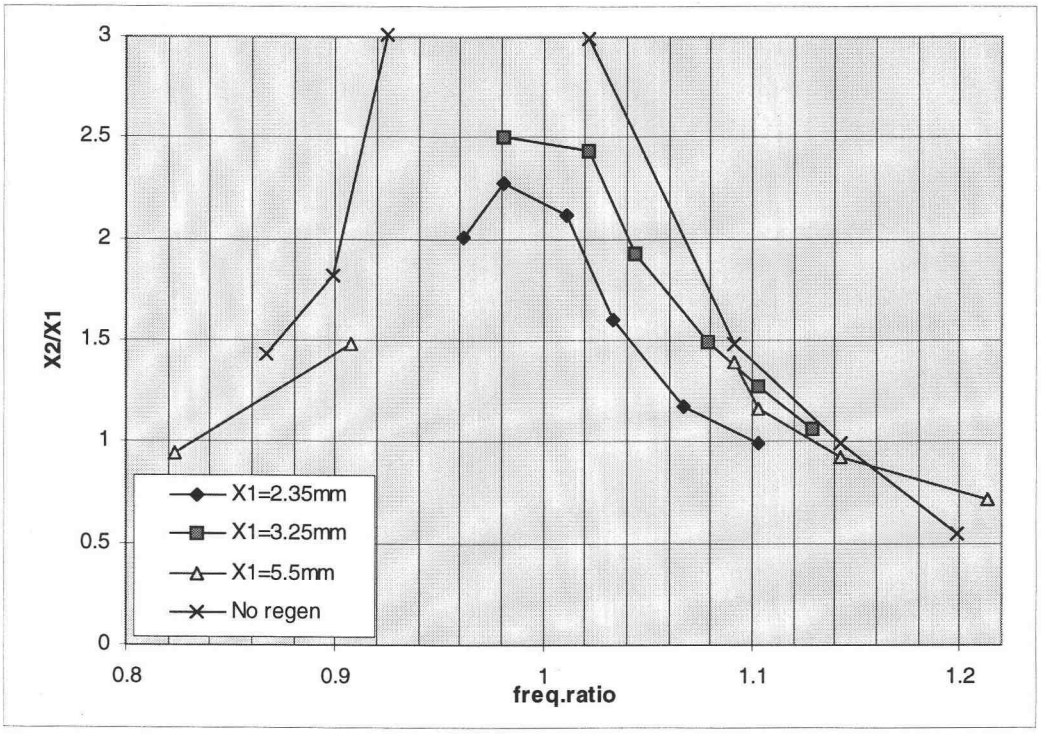

Fig. 5.2 Amplitude ratio vs. frequency ratio.
(Note: tests in the vicinity of ω/ω_n =0.94 is not possible for *X1*=5.5 mm due to the limit in *X2*)

The temperature difference developed across the regenerator increases with the driver amplitude (*X1*) and is at a maximum near the natural frequency. For this experimental setup where the amplitude *X2* is limited, the maximum temperature difference is 58 °C. The cold-side temperature decreases steadily as the frequency increases. The minimum steady state cold-side temperature is 13.9 °C.

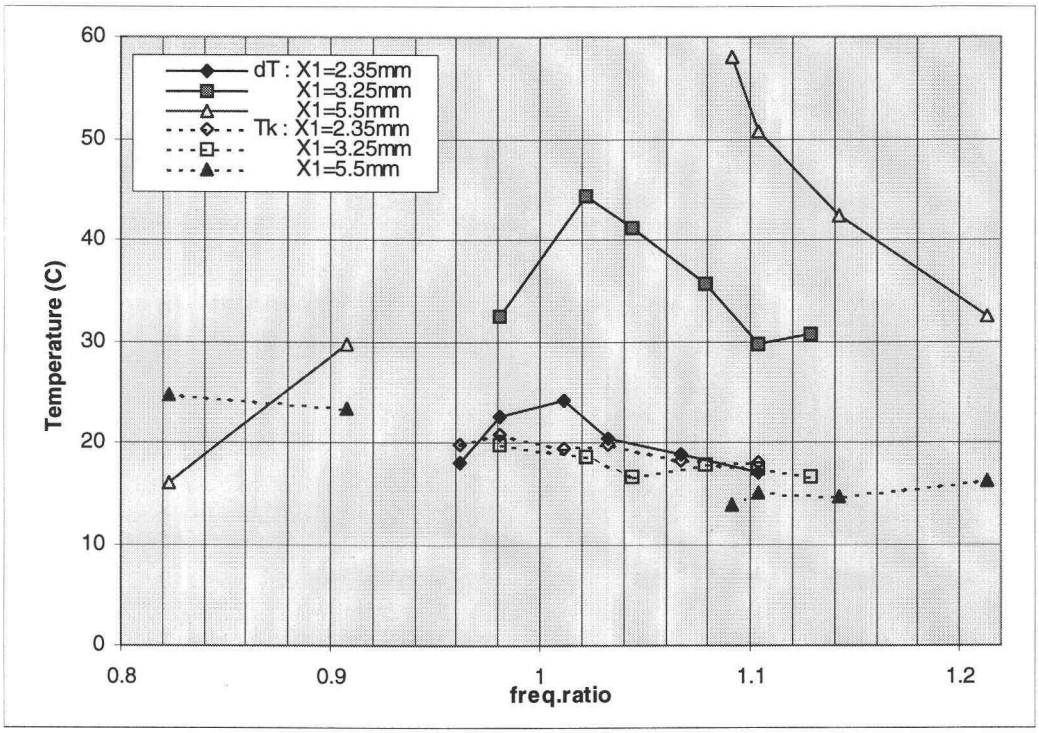

Fig. 5.3 Temperature difference developed across the regenerator and the temperature in the cold-space vs. frequency ratio.

5.1.3) Pressure amplitude and pressure ratio

The amplitude of the pressure variation peaks near the natural frequency and reaches a maximum value of 31000 N/m^2 for the compression space. This value

corresponds to the maximum cooler pressure ratio of 1.36. This peak value comes from the favorable 90 degree phase difference between *X1* and *X2* and the high cold-end bellows amplitude near the natural frequency. The level of the pressure ratio in the compression space is quite different for each *X1*; maxima of 1.15,1.30 and 1.36 were found for *X1*=2.35,3.25 and 5.5 mm, respectively.

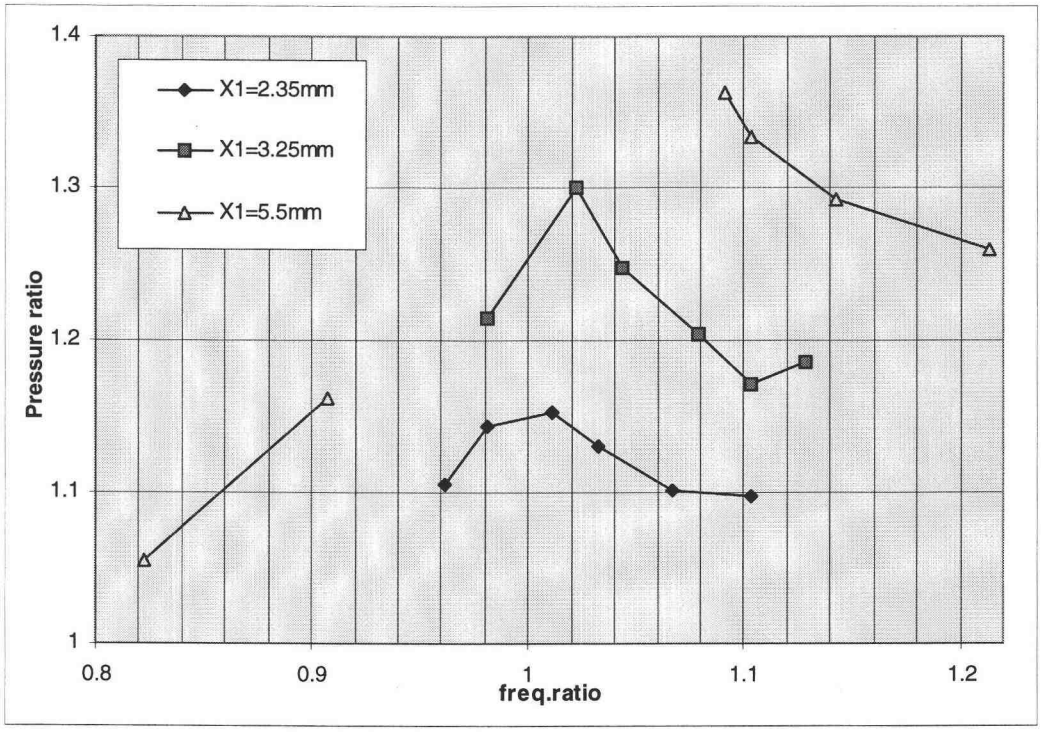

Fig. 5.4 Pressure ratio in compression space vs. frequency ratio.

A pressure drop occurs when the gas is transported from the compression space to the expansion space. The pressure increases with the driving amplitude (*X1*) and reaches 70% of the compression space pressure amplitude (*P1*) when *X1* = 5.5 mm. This maximum value also occurs near the natural frequency. Pressure ratios in the expansion

space are not much different in each of the three cases and attains a value of approximately 1.1.

The phase lag of *P2* with respect to *P1* increases with the amplitude *X1*. The phase shift ranges from 10-25 degree, 25-35 degree and 35-45 degree for *X1* = 2.35,3.25 and 5.5 mm, respectively. These phase lags and pressure drops are direct results of the flow friction in the regenerator. The larger *X1* (and so larger *X2* for a given amplitude ratio) gives higher velocity through the regenerator resulting in higher flow friction. The increase in amplitude ratio near the natural frequency also gives an additional increase in flow velocity and hence loss. Comparison between the pressure drop and phase lag shows that the phase lag does not decrease with natural frequency in the same way as the pressure drop does. This suggests that the effect of increasing speed of operation is more important to the phase lag than the pressure drop.

The amplitude of the bounce space pressure (*P3* in the compression space and *P4* in the expansion space) depends primarily on the amplitude of the bellows displacement. The amplitude of *P3* is therefore almost constant for each test while the amplitude of *P4* increases with the cold-side bellows displacement, *X2*.

5.1.4) Pressure-volume diagram and indicated power

In this investigation, the P-V diagram for each working space was plotted so that the area of the P-V diagram could be determined manually. The phase differences between pressure and volume were also recorded for the determination of the sign of the indicated work. When the volume variation leads the pressure, the bellows (or piston)

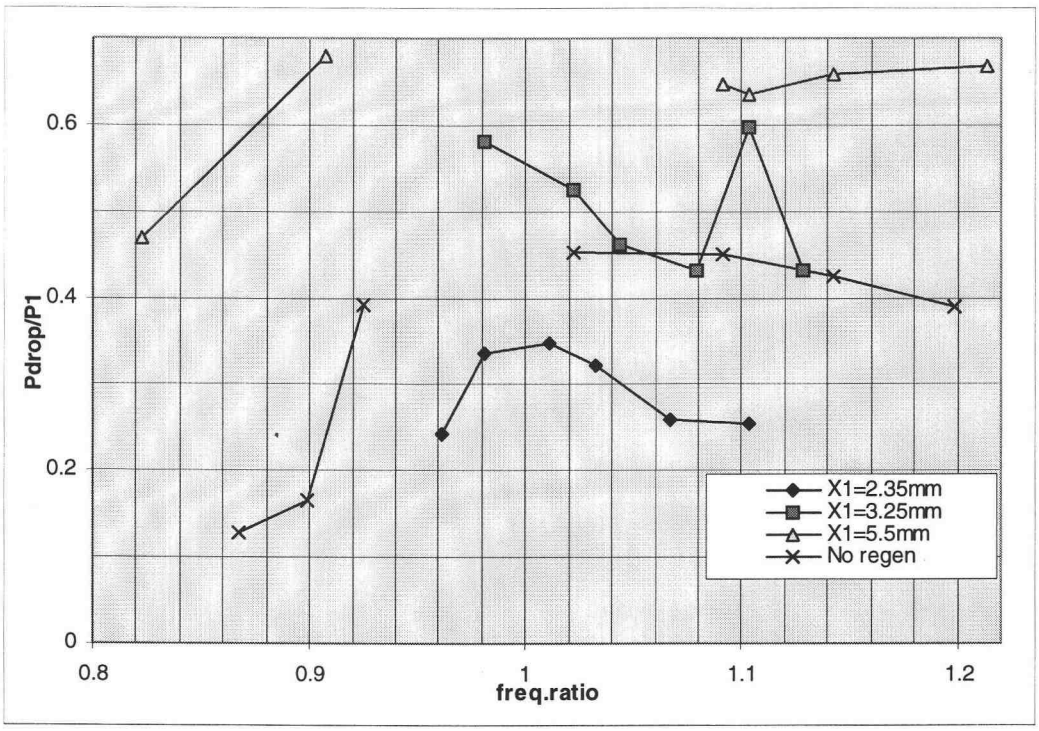

Fig. 5.5 Ratio of the pressure drop to *P1* vs. frequency ratio.

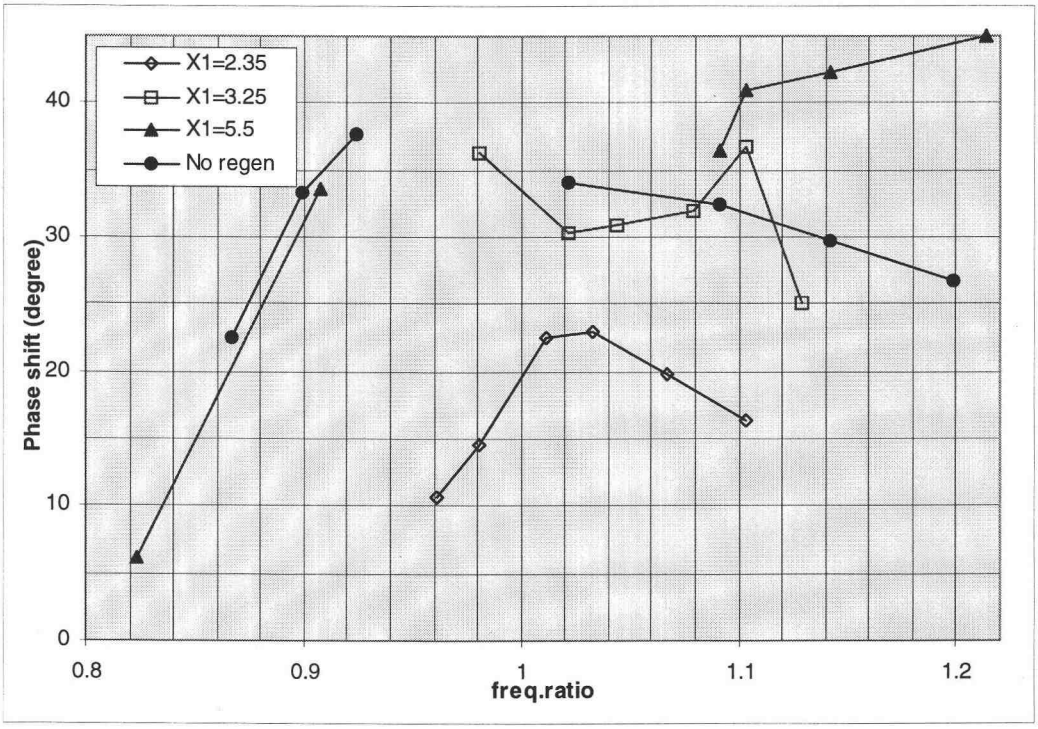

Fig. 5.6 Phase shift (*P1* leads *P2*) vs. frequency ratio.

does work on the system (the working fluid of the cooler). The indicated work is considered negative. On the other hand, when the pressure leads the volume variation, the expansion work is positive with the gas performing work on the bellows.

In the compression space (hot-side bellows), *X1* was found to lead the pressure variation (*P1*). This means that the compression work is being done by the driver. The phase shift ranges from 70 to 195 degrees. The work is negative except when the phase shift exceeds 180 degrees. Then, *P1* leads *X1* and the work is positive. At the natural frequency, *X1* leads *P1* by 130 degree. For the case of no regenerator, the phase shift shows the same trend but with lower values.

The P-V diagrams change shape as the phase shift changes. Figure 5.7 illustrates typical P-V diagrams from the compression volume (PV1).

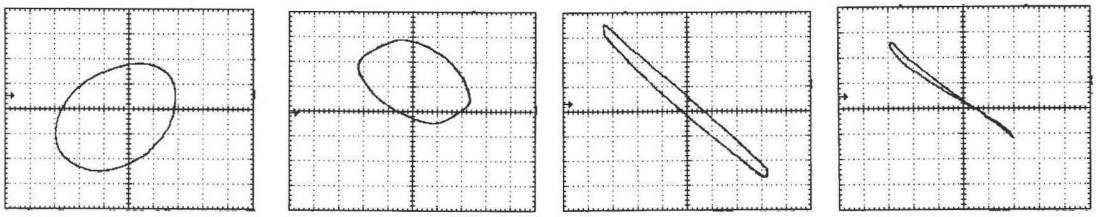

Fig. 5.7 Typical shapes of the P-V diagram in compression space (PV1)
(Note: not in the same scale)

In the cold end, the pressure *P2* was found to lead *X2*. This means that the expansion work is being done by the gas. The work is positive. The phase shift is almost constant for each *X1* and decreases from 120, 110 to 100 degree as *X1* increases from

2.35, 3.25 to 5.5 mm, respectively. In the case of no regenerator matrix, the phase shift is constant at approximately 120 degree over the frequency range.

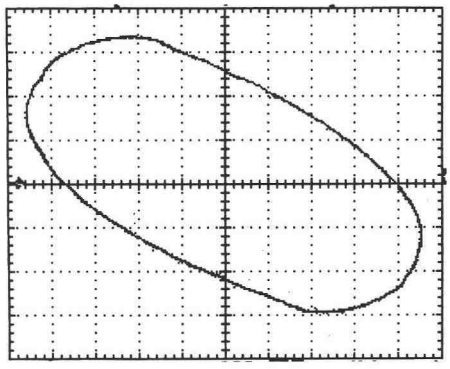

Fig. 5.8 Typical shape of the P-V diagram in the expansion space.

The expansion power and compression power shows an interesting trend. The value of expansion power, *PV2* always has larger values than the compression power, *PV1* except one data point: *X1*=5.5 mm at the frequency ratio less than unity. The approximately-constant 100 degree phase shift in the cold-end makes *PV2* depend primarily on the pressure and displacement amplitude in the expansion space. Because the pressure drop is not large compared with the displacement ratio, *PV2* shows a large magnitude through out the frequency range and is in the order of 2 to 4 watts of cooling potential. For the compression power, as the displacement *X1* is kept constant, *PV1* depends primarily on *P1* and the phase shift. The amplitude *P1* is at a maximum near the natural frequency and the phase shift ranges from 70 to 195 degree. The 90 degree phase shift occurs at the frequency ratio 0.95, and the 195 degree phase shift giving a negative indicated work occurs at the frequency ratio of 1.22. As a result, the compression power

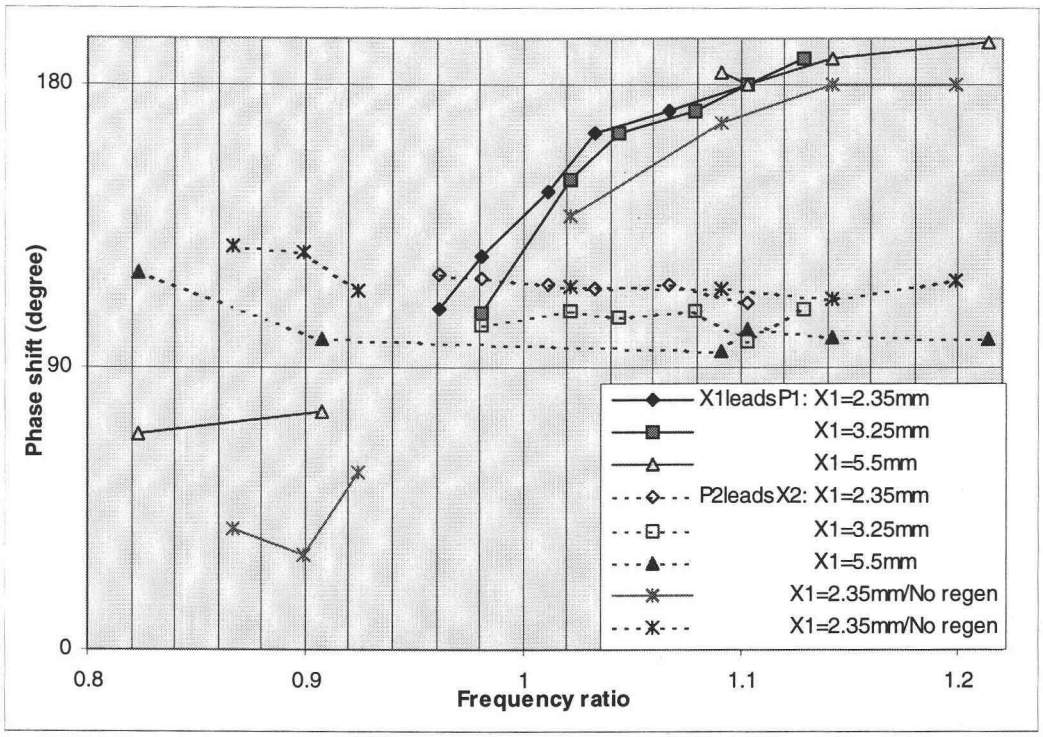

Fig. 5.9 Phase shift in hot and cold space vs. frequency ratio.

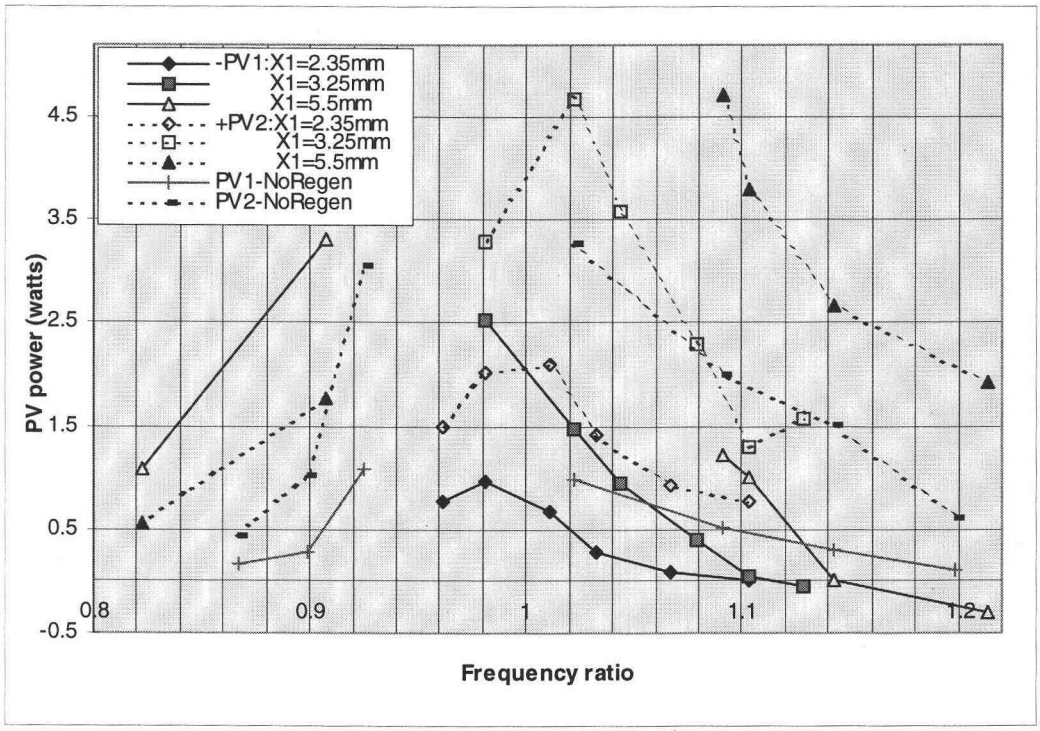

Fig. 5.10 Indicated power in hot and cold space vs. frequency ratio.

shows the maximum value at the frequency ratio between 0.95 and 1.0 and the value decreases with the increasing frequency ratio.

In the bounce space, the data for the phase difference between X and P was too erratic due to a small phase shift in the gas spring space. The actual pressure and displacement variation was plotted for some operating point where the phase shift is discernible, and the trend was figured out for the sign of the P-V diagram area.

In the cold-side bounce space, the P-V diagram area is negligibly small and can be neglected.

5.1.5) Energy balance

If the cooler is considered an isolated system, the summation of the compression power and expansion power in the two working spaces and two bounce spaces gives the indicated power of the system. In the case presented, the indicated power should be negative–meaning that input power is needed to run the cooler. However the positive *PV2* value dominates and the indicated power is positive. This trend does not mean that the cooler gives the surplus expansion power while producing cooling effects. It does mean that, for this free-piston type machine to sustain the motion and thermodynamic process, some part of the energy must be expended into various parasitic losses (discussed in section 4.1.3). With this in mind, it is apparent from Fig. 5.11 that these losses have not been taken into account. Five types of loss are important here: regenerator loss, shuttle heat transfer loss, conduction, radiation loss, windage loss, and friction loss. While the isolation of each loss for study is not possible, an attempt had been made to estimate the

magnitude of the windage and bellows spring hysteresis loss.

The bellows used in this test was driven by a shaft without an elastomer seal with displacement amplitudes of 2.4 and 4.8 mm. The friction and windage loss in the driver was isolated and the summation of the windage loss and hysteresis loss in the bellows spring was determined. Figure 5.12 shows that the loss increases rapidly with the frequency. The magnitudes of the loss reaches 0.5 and 3.0 watts for the 2.4 and 4.8 mm amplitudes respectively. This result shows that the parasitic losses attain very high values compared with the indicated power. Further experimental developments can be done to reduce these losses.

Electrical power input is consumed by Joule heating, friction, and windage losses. The remaining power goes to the cooler. The electrical power input comes from the products of rms voltage and current supplied to the voice coil actuator. For this cooler, the power level ranges from 10 to 45 watts. Figure 5.13 shows the percentage distribution of the power to each part while the input power is taken to be 100%. It shows that the Joule heating loss takes up to 50-75% of the input power. The friction loss increases with frequency and amplitude and ranges from 20-40%. The cooler, therefore, receives only 10-20% of the power input.

5.1.6) Performance indices

The expansion work in the expansion space is generally used to assess the cooling capacity of a cooler. In the same way, the rejected heat from the compression space is determined by the the compression power. For this cooler, although there are many

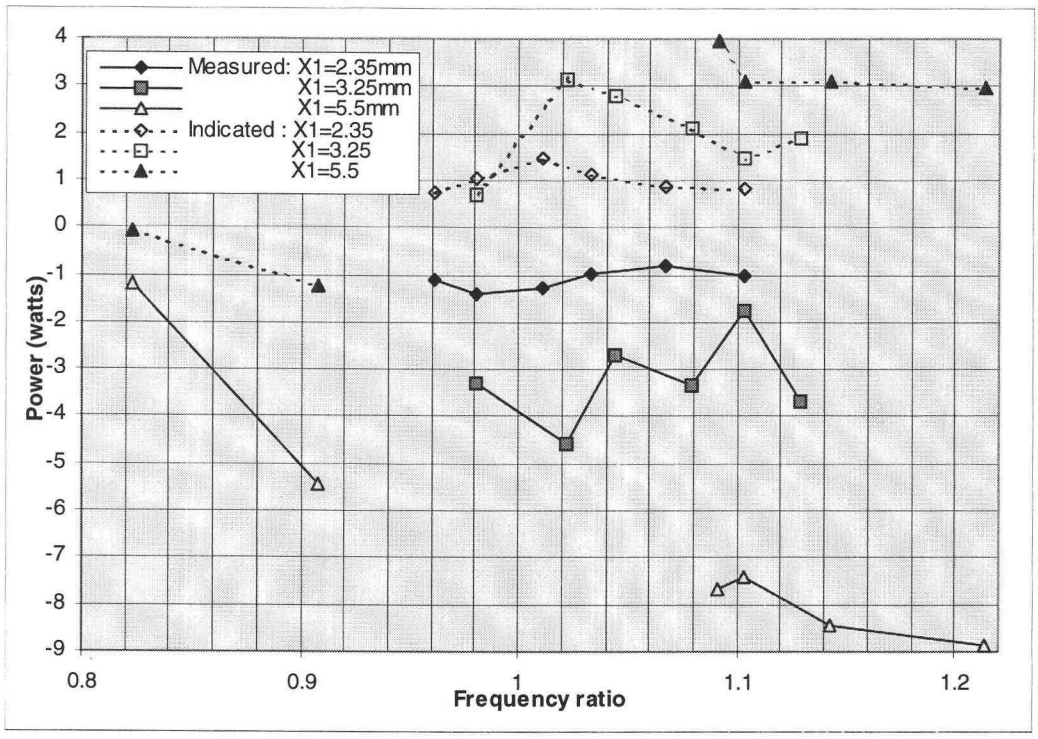

Fig. 5.11 Measured cooler power and indicated cooler power vs. frequency ratio.

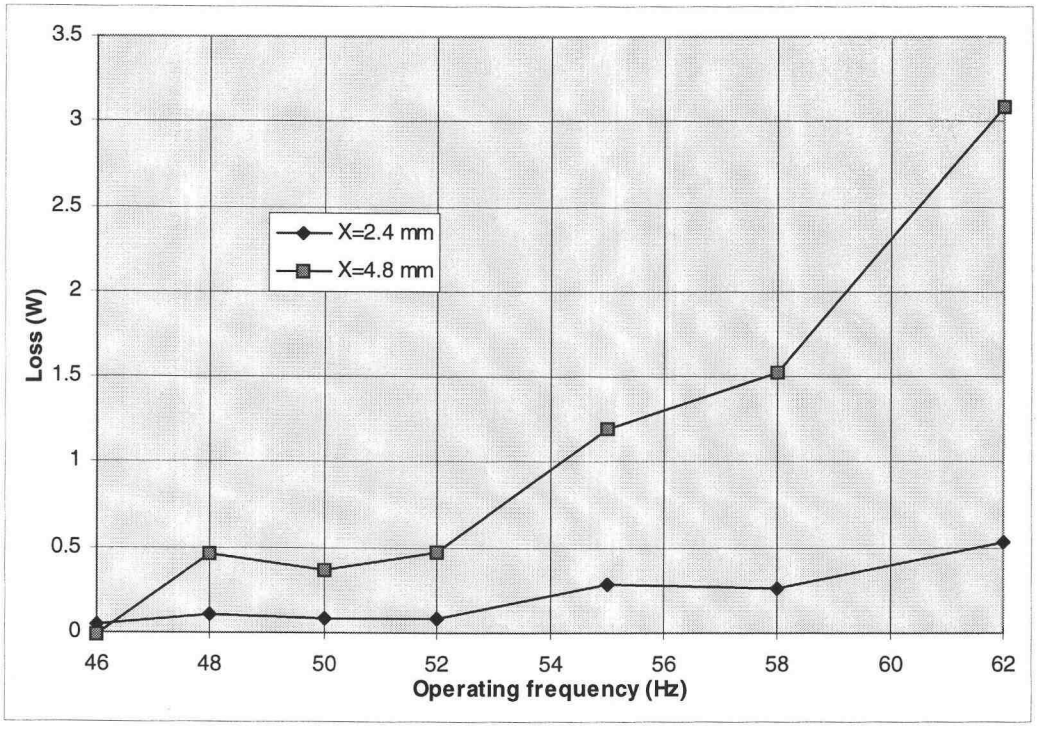

Fig 5.12 Windage and bellow spring hysteresis loss vs. operating frequency.

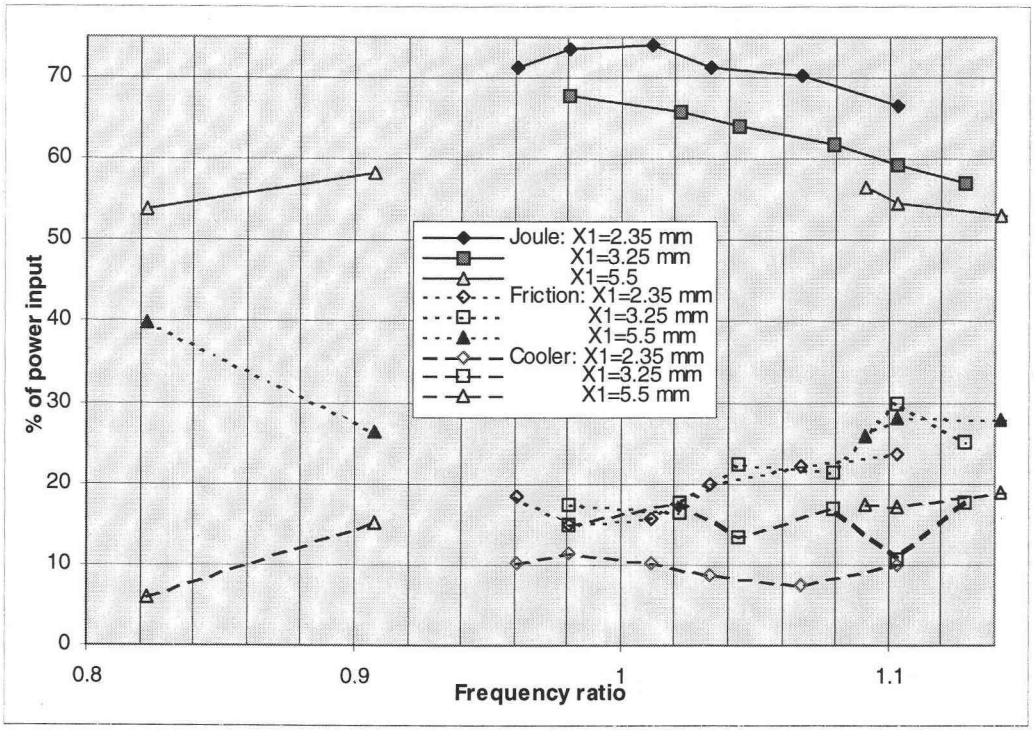

Fig. 5.13 Percentage distribution of the Joule heating loss, friction loss and cooler power vs. frequency ratio.

parasitic losses as were discussed in section 4.1.3, Figure 5.14 shows a good correlation between the indicated cooling power (*PV2*) and the temperature difference developed across the regenerator. For this cooler, however because the absorption and rejection of heat through the cooler was done with natural convection, the cold-side temperature (T_k) is not directly a cooling performance index but is a result of the performance of the cooler and the heat exchangers associated with this cooler.

From the discussion above, the expansion work can be used as a cooling capacity index. The cooler performance indices in form of the coefficient of performance (*COP*) can then be determined. Figure 5.15 shows the cooler *COP* (*PV2*/Cooler power) that

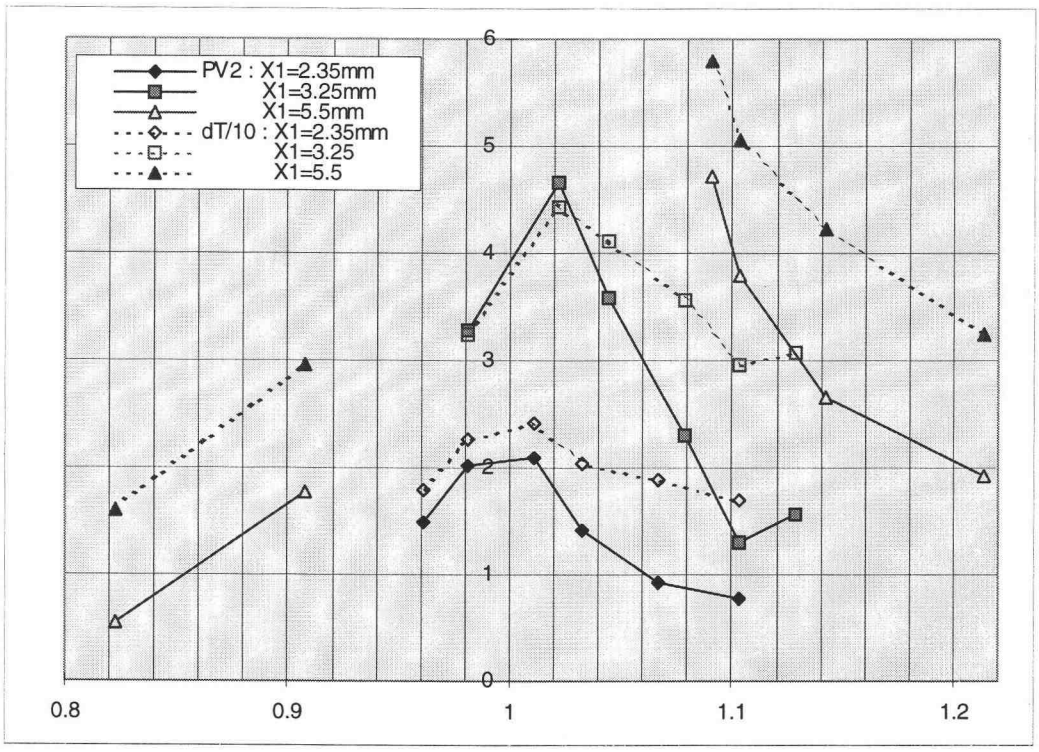

Fig. 5.14 Cooling potential (PV2, watts) and the temperature difference(in 1/10 scale) vs. frequency ratio

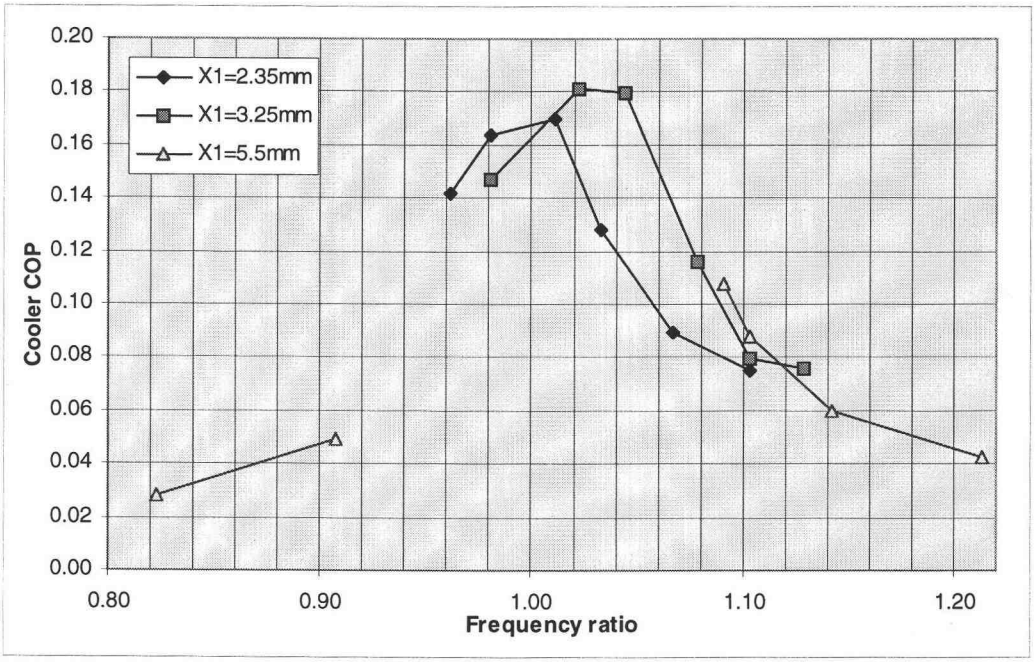

Fig. 5.15 Cooler COP vs. frequency ratio

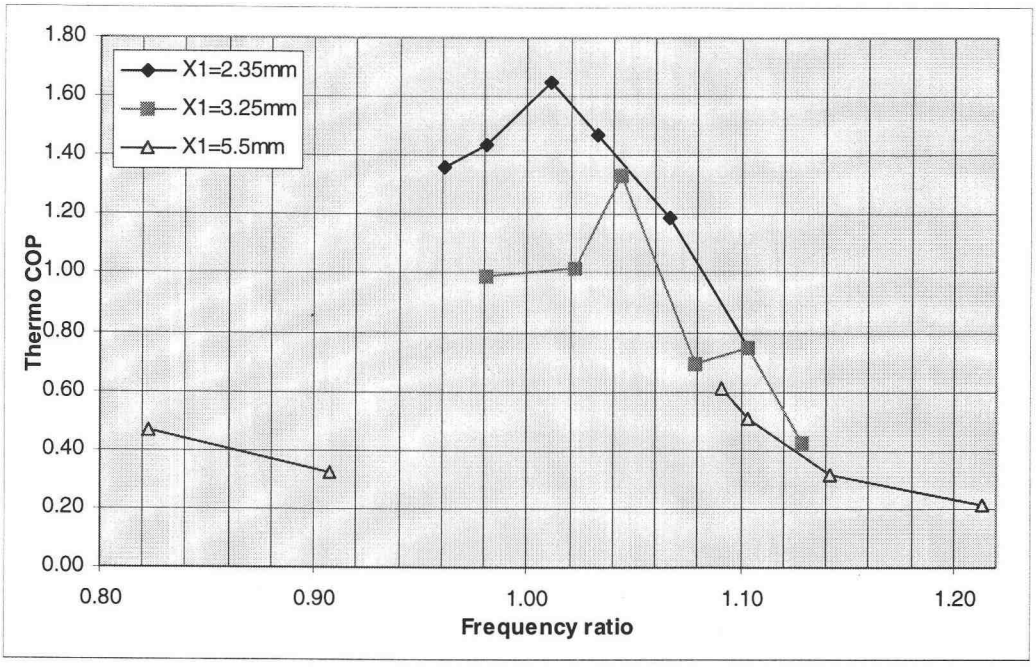

Fig. 5.16 Thermodynamic COP vs. frequency ratio

peaks near the natural frequency with the value of 0.18. Figure 5.16 shows the thermodynamic *COP* (*PV2*/Motor power) that also peaks near the natural frequency with the value of 1.6, but the trend is somewhat more erratic. For both *COP*s, all three *X1* settings follow nearly the same trend.

5.2) RCAS cooler test with helium at 1, 1.5 and 2 atm (*X1*=2.35 mm)

5.2.1) Experimental setup

The RCAS cooler was charged with helium at 1 atm pressure, 7.5 psig (designated as 1.5 atm) and 15 psig (designated as 2 atm) for each data test. It was run at a constant

hot-side bellows displacement of *X1*=2.35 mm while the frequency was varied.

For this test setup, the cold-side HET was the same as the one used in the air test (mm=*V**0.5071-0.1555). Because the increased charge pressure affects the static position of the driving shaft, the displacement, *X1* was measured separately for each test. The shaft seal was made of molded silicone sealant drilled to size. A single seal contained the working pressure for all three cases without significant leaking during the test. The complete data were tabulated in Appendix 9.

5.2.2) Phase shift and natural frequency

The phase shift between the hot- and the cold-side bellows in this helium test shows the cooler phase shift characteristic : *X1* leads *X2*. The natural frequencies where the phase shift attains 90 degrees (see Fig. 5.17) are at 52, 61 and 68 Hz for pressure of 1, 1.5 and 2 atm, respectively. When the frequency is nondimensionalized, the trends for all three phase shifts are similar. For this test the frequency ratio ranges from 0.8 to 1.14

The amplitude ratio and the temperature difference were investigated in relation to the natural frequency. Higher charge pressure with the same *X1* gives higher amplitude ratio. The maximum amplitude ratio reaches 2.5 in the 2 atm case just below the natural frequency. For the 1 atm case, the helium test gives a lower maximum amplitude ratio than the air test (with the same *X1*=2.35mm) and smaller phase shifts over the same frequency ratio range. This occurs while the natural frequency for both cases are almost equal (51.5 and 52 Hz for air and helium case). This behavior suggests that the change

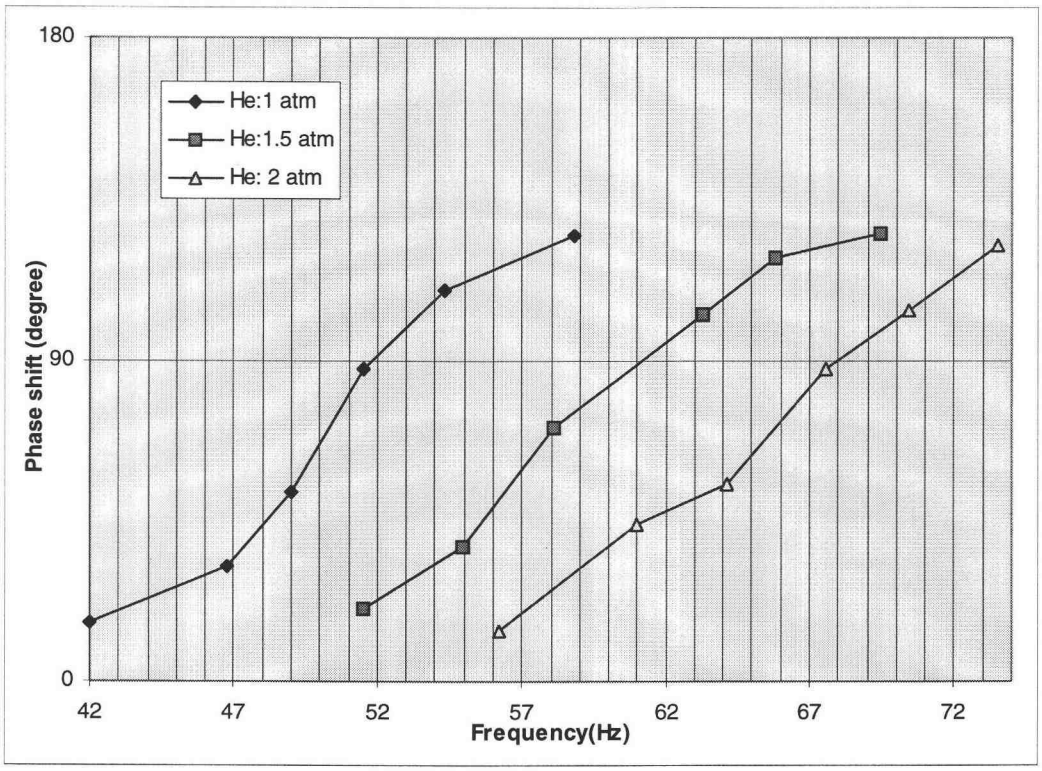

Fig. 5.17 Phase shift (*X1* leads *X2*) vs. operating frequency.

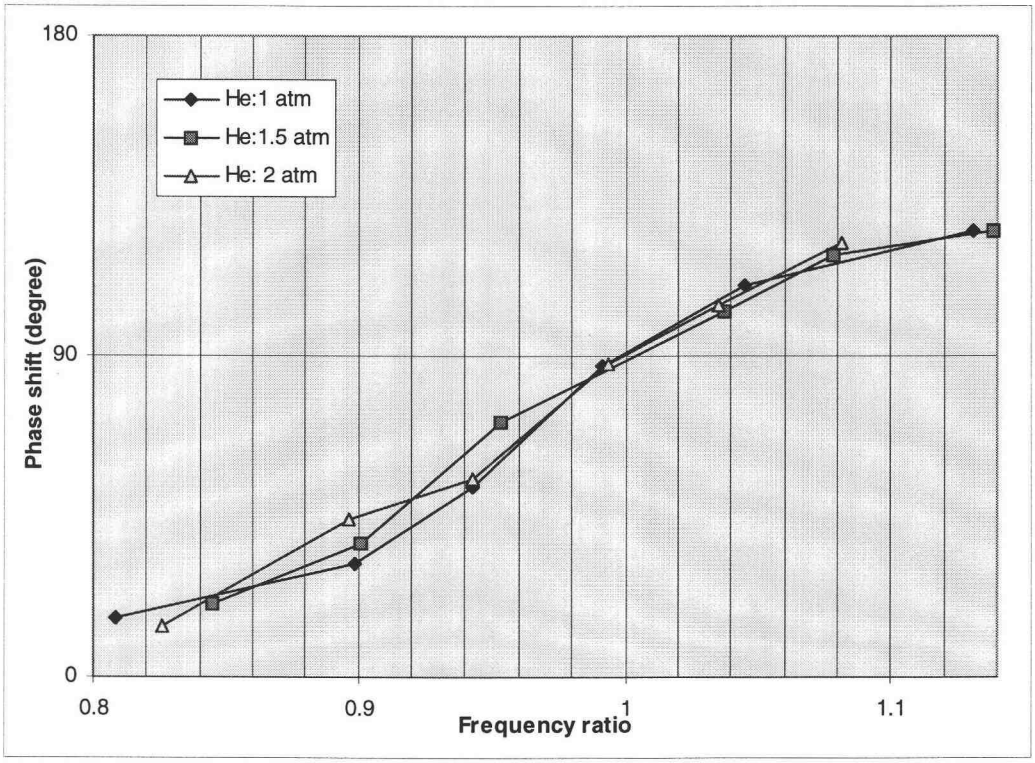

Fig. 5.18 Phase shift (*X1* leads *X2*) vs. frequency ratio.

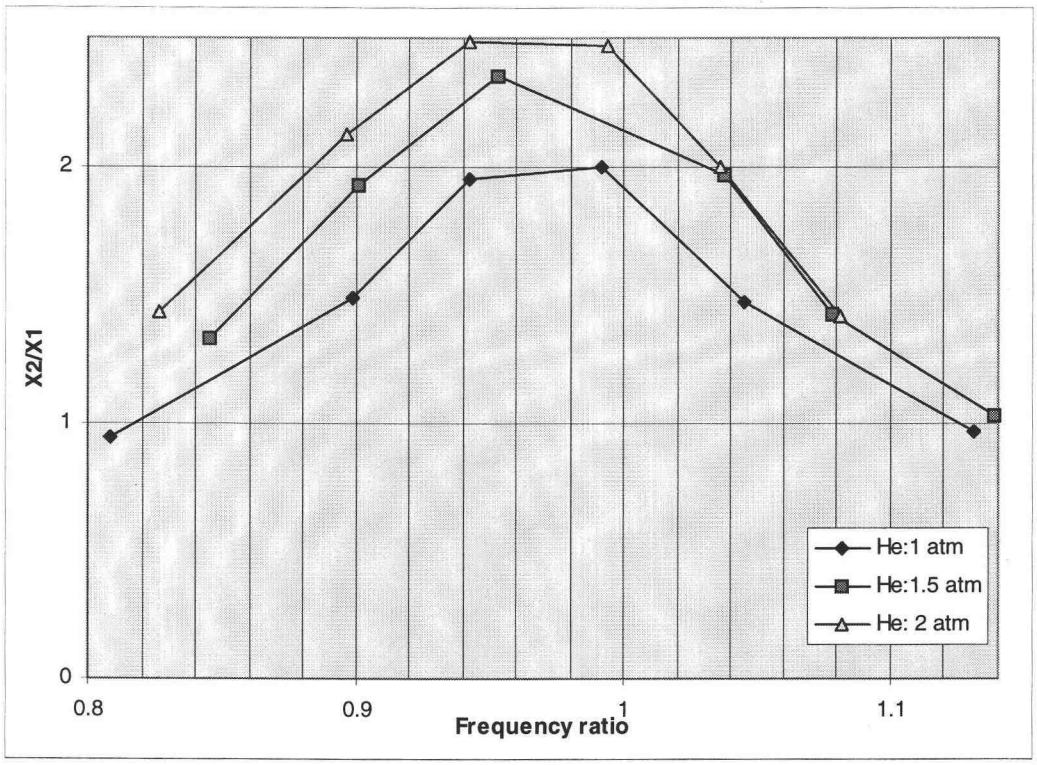

Fig. 5.19 Amplitude ratio (*X2/X1*) vs. frequency ratio.

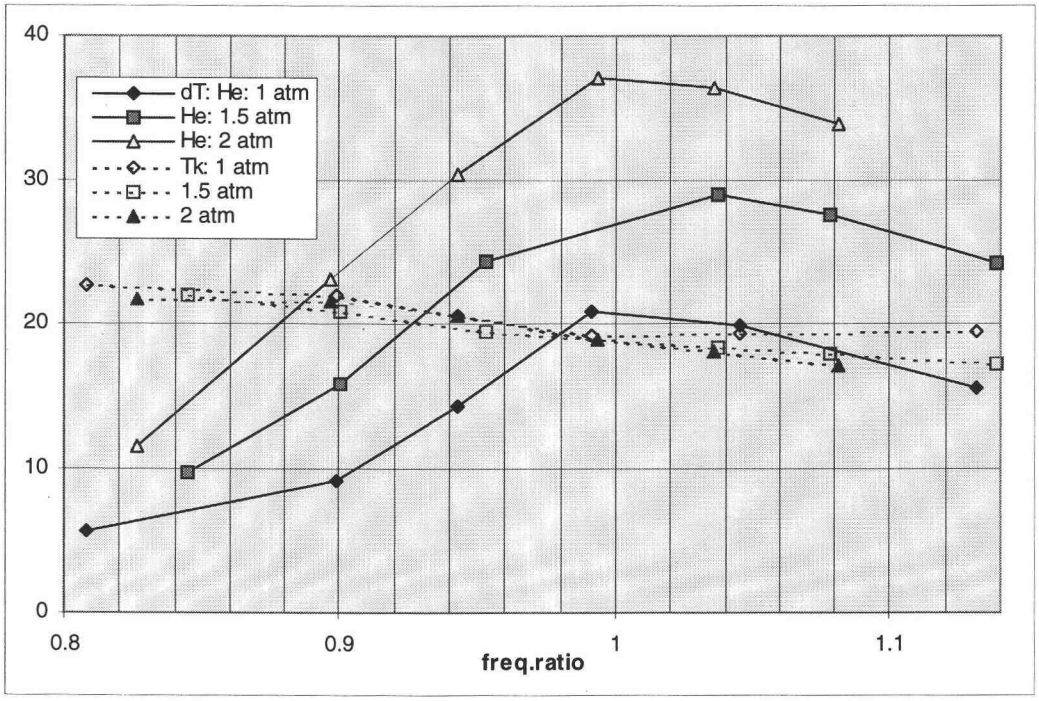

Fig. 5.20 Temperature difference developed across the regenerator and the temperature in the cold-space vs. frequency ratio.

from air to helium affects primarily the increase in damping coefficient in the dynamic model while leaving the spring element the same.

The temperature difference developed across the regenerator shows the maximum value just above the natural frequency with a maximum value of 37 °C at 2 atm. The cold-side temperature for all three cases decreases with frequency and follows similar trends. The lowest cold-side temperature is 17 °C at 2 atm. Compared with air at 1 atm, the maximum temperature differences are 24 and 21 °C and the minimum cold-side temperatures are 18 and 19 °C for the case of air and helium, respectively. The difference is minimal and it shows the potential of helium to run with higher *X1* with the same limit on *X2* (due to its lower *X2/X1* ratio) for better cooling capacity.

5.2.3) Pressure ratio and pressure drop

The amplitude of the pressure variation in the compression space peaks near the natural frequency and reaches maximum values of 15000, 24000 and 36000 N/m^2 for helium at 1, 1.5 and 2 atm, respectively. These values correspond to the maximum pressure ratio of 1.16, 1.17, and 1.20. The pressure ratio for all three cases follow a similar trend.

Pressure drops (nondimensionalized by *P1*) show different trends for each charge pressure. The pressure drop decreases with frequency at 1 atm. It increases slightly with frequency at 1.5 atm and it increases rapidly with frequency at 2 atm. The maximum

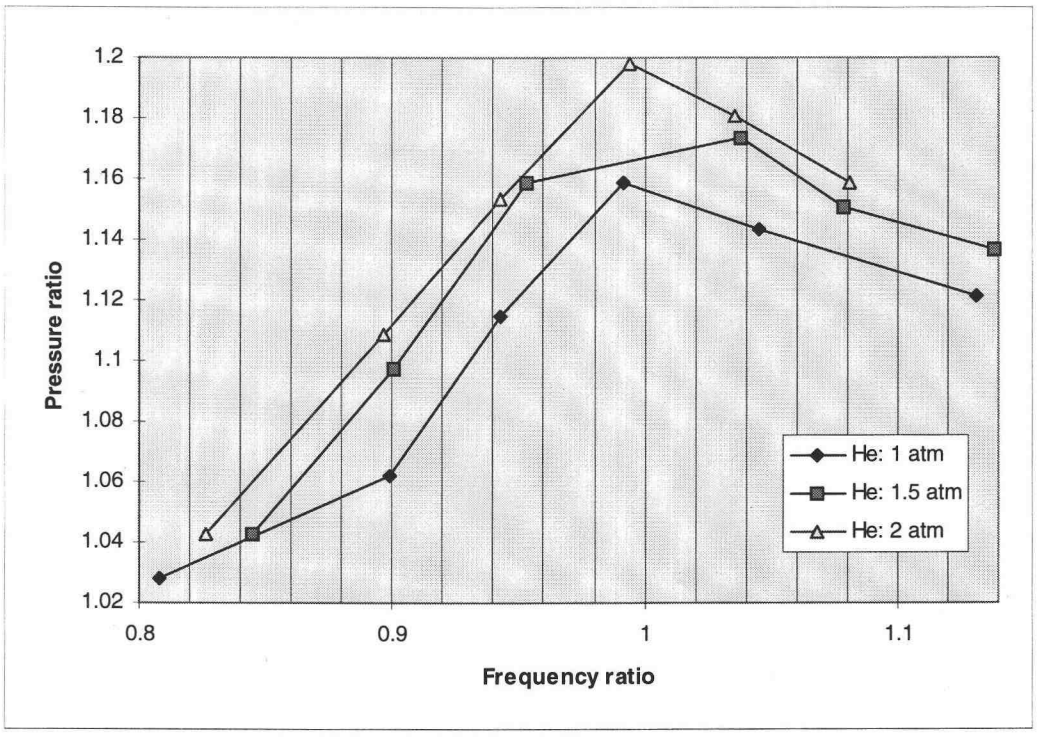

Fig. 5.21 Pressure ratio in compression space vs. frequency ratio.

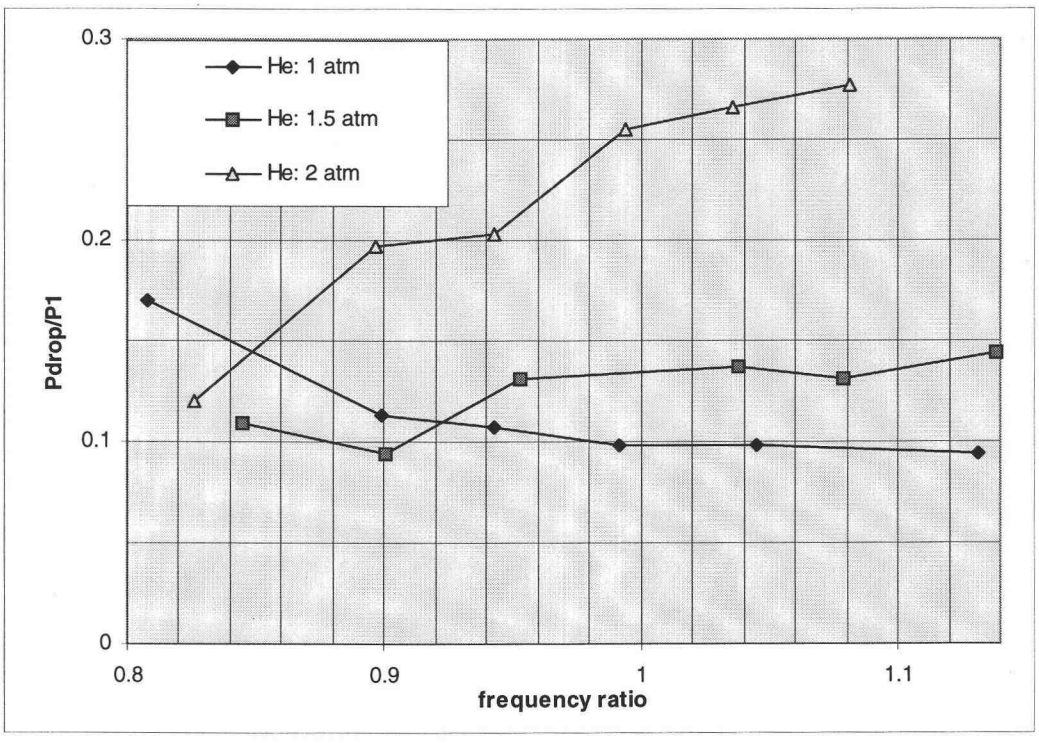

Fig. 5.22 Ratio of the pressure drop to *P1* vs. frequency ratio.

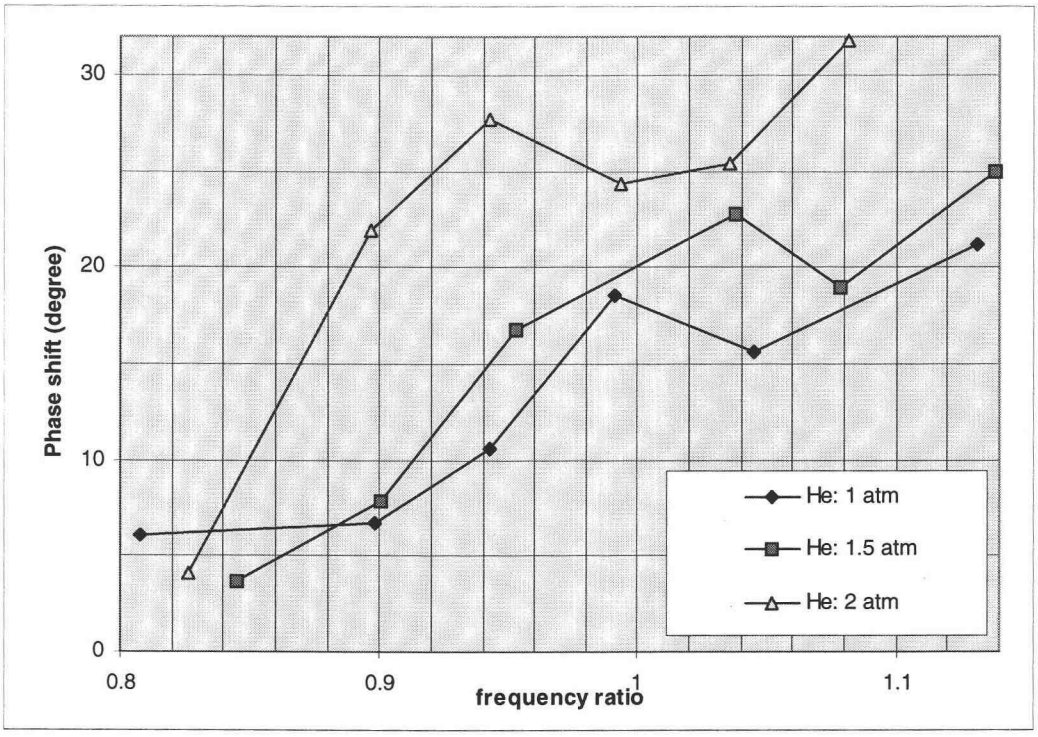

Fig. 5.23 Phase shift (*P1* leads *P2*) vs. frequency ratio.

value reaches 0.3 for the 2 atm case. Compared with air at 1 atm, the ratio of the pressure drop is much less in the helium case (0.35 vs. 0.15).

5.2.4) Pressure-volume diagram and indicated power

In the compression space, the displacement *X1* was found to lead the pressure *P1*. The phase shift ranges from 50 to 140 degree. From the 105 degree phase shift (which is close to the optimum 90 degree) and the peak in pressure ratio near the natural frequency, the indicated power *PV1* is a maximum near the natural frequency and reaches 4 watts in the 2 atm case. At 1 atm, with the same *X1*, the values of *PV1* are comparable in both the

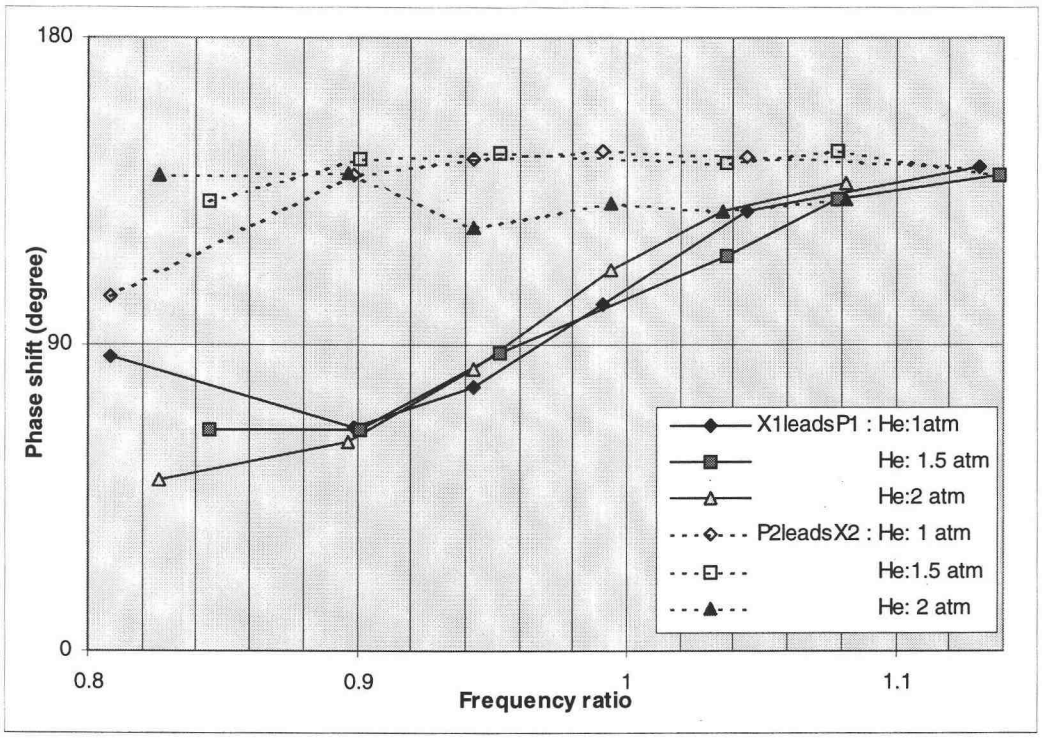

Fig. 5.24 Phase shift in hot and cold space vs. frequency ratio.

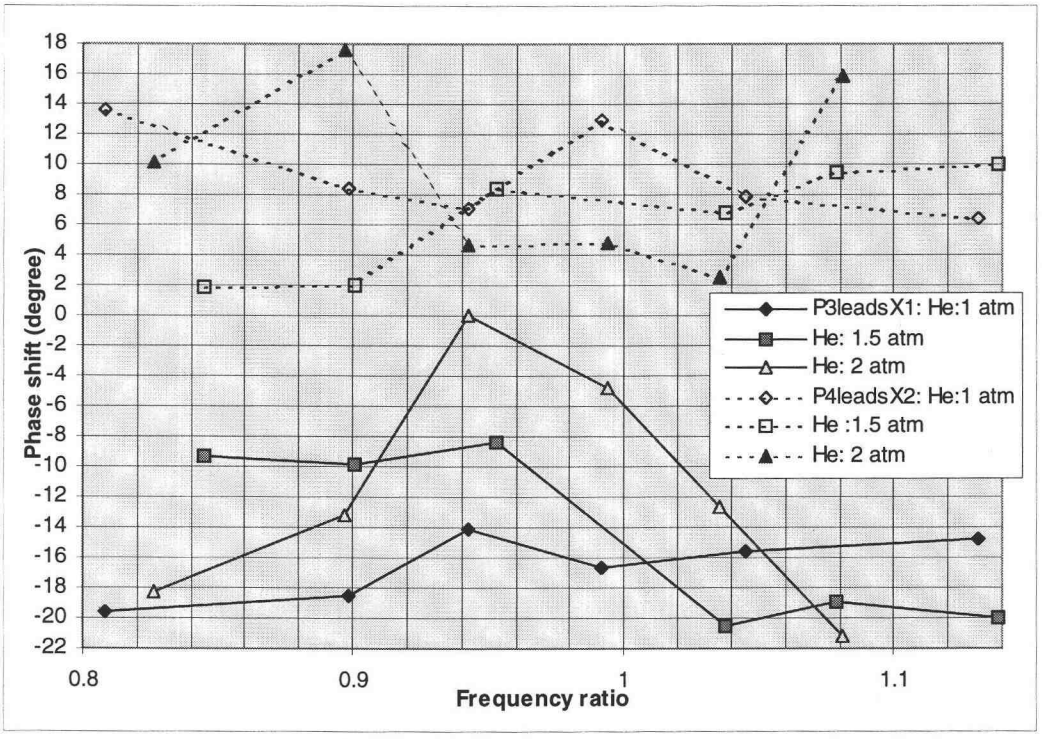

Fig. 5.25 Phase shift in hot and the cold-bounce spaces vs. frequency ratio.

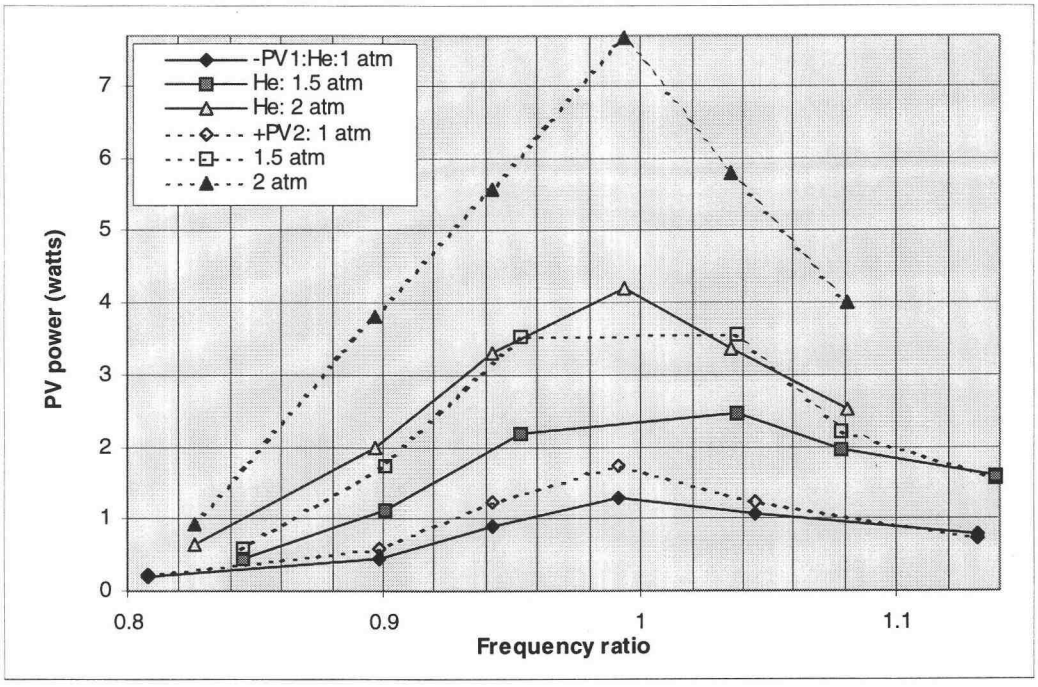

Fig. 5.26 Indicated power in hot space (negative power, PV1) and cold space (positive power, PV2) vs. frequency ratio.

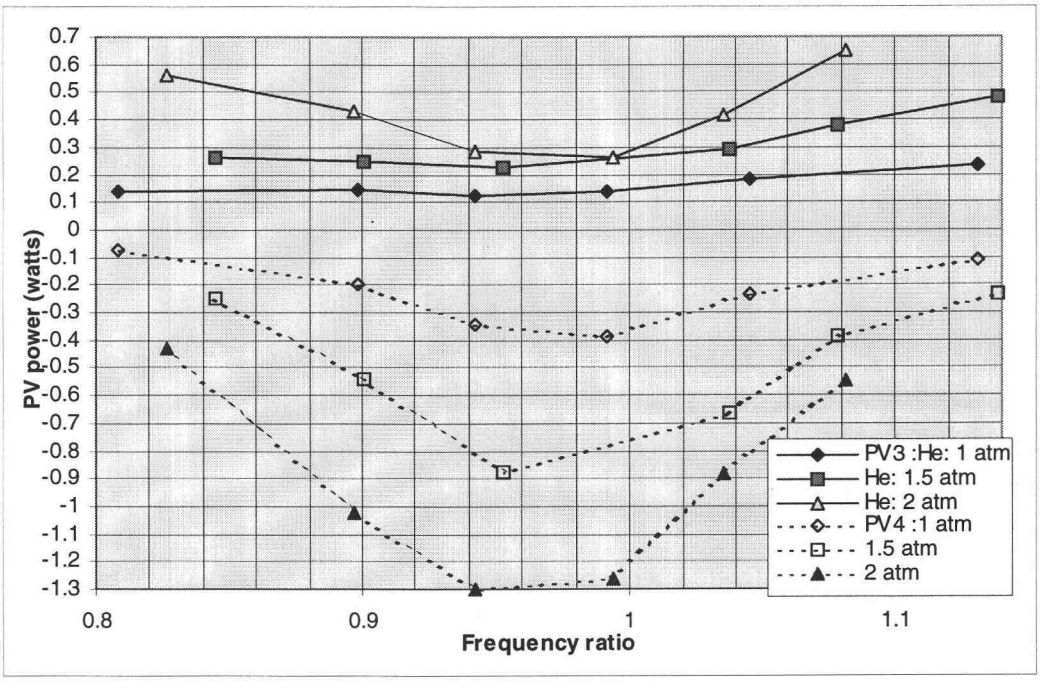

Fig. 5.27 Indicated power in hot- and cold-bounce space vs. frequency ratio.

air and helium test (maximum of 1 watts). In the expansion space, *P2* was found to lead *X2*; the positive expansion work is being done by the gas. For all cases of helium, the phase shift is almost constant in the vicinity of 130-140 degrees. With the peak in amplitude and pressure ratio, the indicated power *PV2* is a maximum near the natural frequency and reaches 7.5 watts in the 2 atm case. The *PV2* value is also comparable in both air and helium tests at 1 atm (maximum of 2 watts).

5.2.5) Energy balance

Electrical power input for the test with helium ranged from 10 to 35 watts. Figure 5.28 shows the percentage distribution of the input power. Joule heating loss takes up to 60-70 % of the input power. The friction and the remaining power going to the cooler are approximately equal at 10-20 %. For both air and helium at 1 atm, the measured cooler powers are approximately 1 watt. The energy balance, however, suggests that the parasitic losses are a maximum of 12 watts near the natural frequency.

5.2.6) Performance indices

The indicated power in the expansion space was used as a cooling capacity index. Figure 5.30 shows the behavior of this inex and compares it with the temperature difference developed across the regenerator. There is a fair correlation between the indicated power(*PV2*) and the scaled temperature difference(*dT*/10) for the helium cases. The cooler *COP* shown in Fig. 5.31 increases with the pressure and reaches a maximum

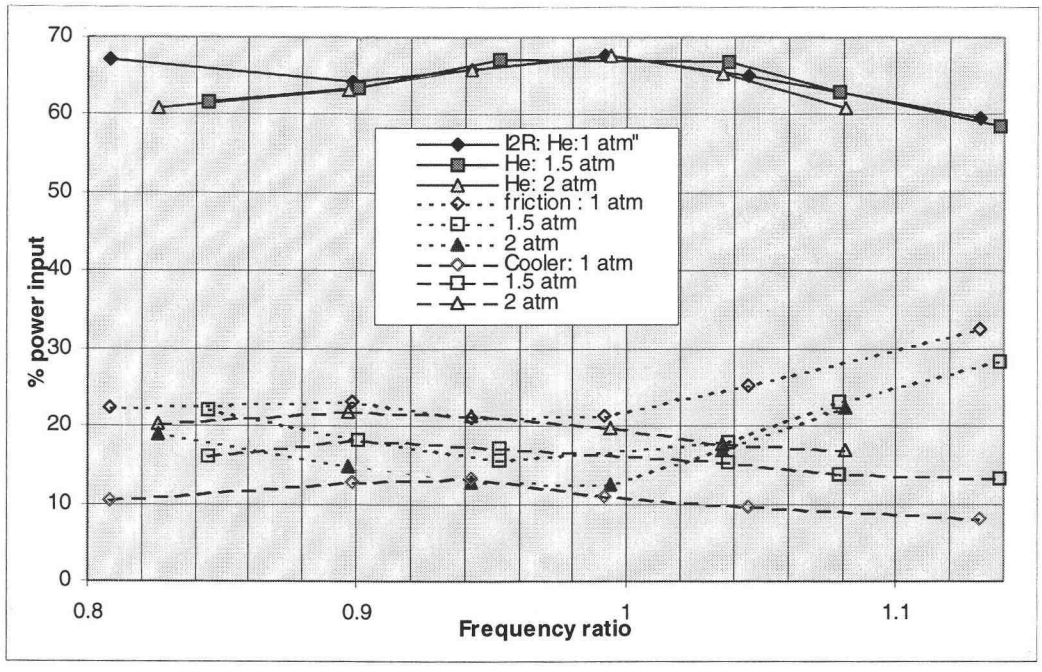

Fig. 5.28 Percentage distribution of the Joule heating loss, friction loss and cooler power vs. frequency ratio.

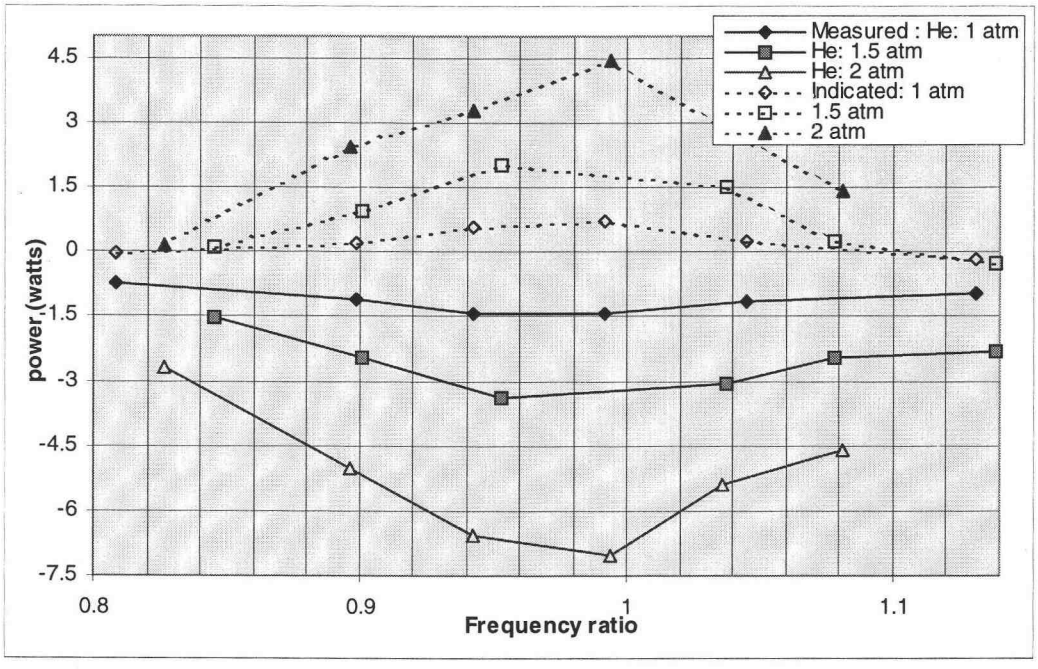

Fig 5.29 Measured cooler power (negative input power) and indicated cooler power vs. frequency ratio.

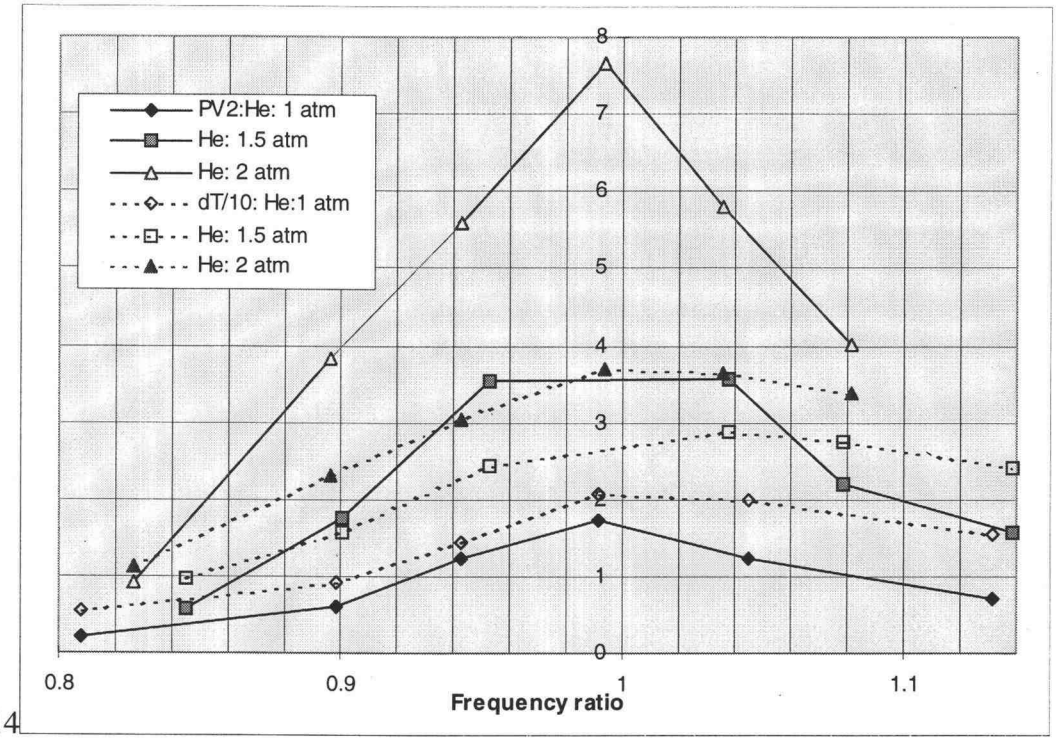

14

Fig. 5.30 Cooling potential (PV2, watts) and the temperature difference(in 1/10 scale) vs. frequency ratio.

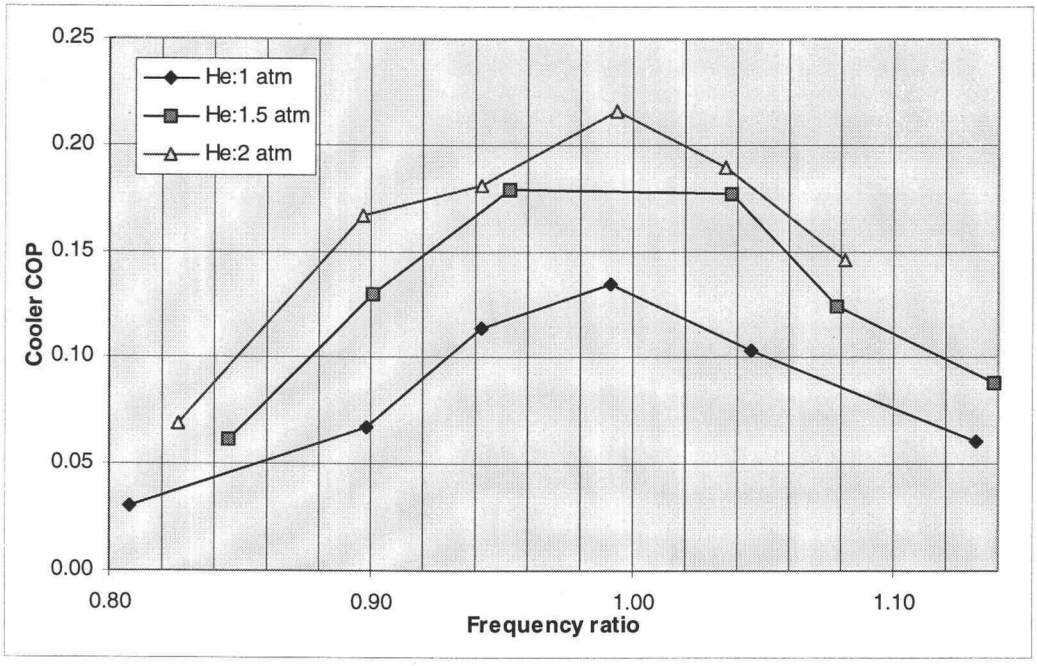

Fig. 5.31 Cooler COP vs. frequency ratio.

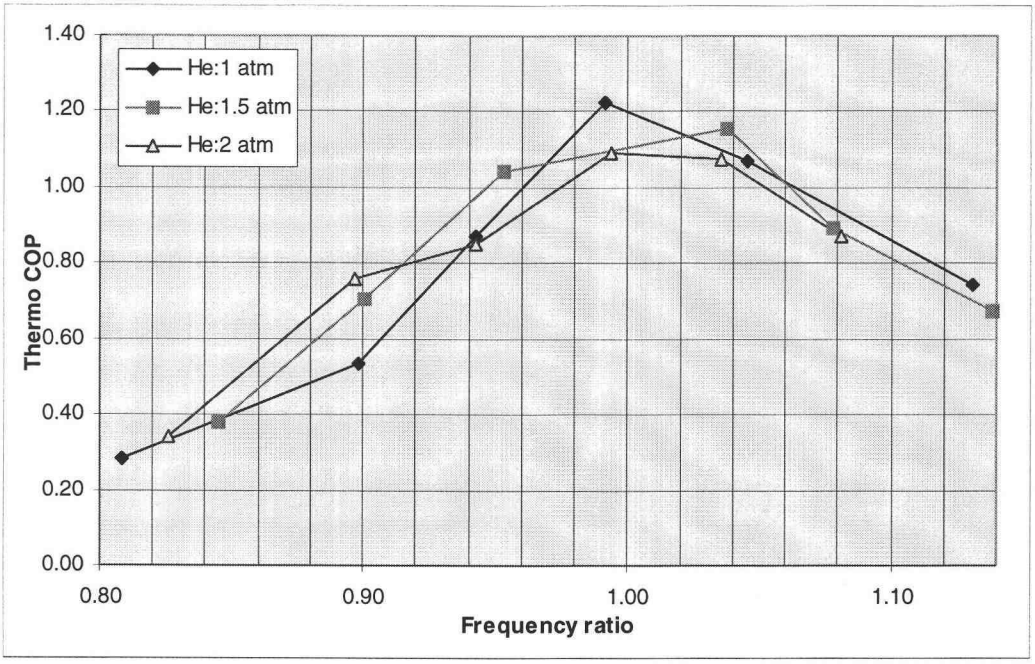

Fig. 5.32 Thermodynamic COP vs. frequency ratio

value of 0.22 near the natural frequency. The thermodynamic *COP* shown in Fig. 5.32, however, shows a similar trend for each charge pressure. Compared with air at 1 atm (having maximum cooler *COP* of 0.17), the maximum value for the helium case is only 0.14. The maximum value of the thermodynamic COP is 1.2 near the natural frequency which is also lower than the case for air (maximum of 1.6).

CHAPTER 6
CONCLUSIONS

6.1 RCAS cooler design and operation

The alpha configuration of the cooler exhibits its simplicity throughout the design. It facilitates the use of the stainless steel bellows in place of the piston. The construction tolerances were relaxed and the placement of transducers was made easier.

The use of stainless steel bellows eliminates the piston seal. The only dynamic seal in this cooler is the driver shaft seal. After experimenting with many design, the tight-fit molded silicone sealant was proved to sustain the working pressure for each test for up to 15 psig.

Although the use of bellows simplified many design details, fatigue life was a problem. For small diameter bellows used in this investigation, the fatigue life is only about six million cycles. Larger diameter bellows employed in the working spaces have 2-3 times longer life. Detailed design studies to extend the bellows life are needed.

The use of voice coil actuator to drive the cooler provides great versatility in terms of the ease of adjustment in both frequency and motion amplitude. The coupling between the driver and cooler is easy and high radial tolerances are allowed.

The critical component of the cooler is the regenerator. The simple design of steel wire wool was employed and the experimental parameter optimization was performed to obtain the best performance from the design. Fractional factorial experimental array from the Taguchi method was brought in to reduce the number of experiments needed for optimization. Four parameters were investigated in the method applied in this study, 1)

coarseness of the wire wool, 2) weight of the wire wool, 3) dynamic mass of the cold-side bellow and, 4) the damping controlled by the orifice. The results are satisfactory: the performance is improved with a minimum set of experiments. The improvement in the temperature difference in the air test and helium test are 8 and 6 % respectively while the number of tests was reduced from 81 to 9 for each working gas. Although the method gives the improved performance for both air and helium tests, the prediction formula is more reliable in the case of air than for helium.

6.2) Frequency and phase response

Driven by the voice coil actuator, the hot-side displacement (*X1*) leads the cold-side displacement (*X2*). This is the characteristic phase shift of the Stirling cycle cooler. The phase shift of 90 degree was chosen as the natural frequency: 51.5 Hz in the air test.

The operating frequency was nondimensionalized by the natural frequency to the frequency ratio. All performance parameters were then referred to this normalized frequency. For the range of frequency ratio between 0.8-1.2 in the air test, the phase shift varies from 15 to 160 degrees. The air test on three levels of hot-side displacement amplitude together with the test with the regenerator removed suggests that the phase shift results primarily from the dynamic response of the system.

At 1 atm, the natural frequency for the helium test is 52 Hz; approximately the same value as in the air test. With the increased charge pressure to 1.5 and 2 atm, the natural frequency increases to 61 and 68 Hz, respectively. When nondimensionalized to

the frequency ratio, however, for all three pressure levels the phase shifts follow essentially the same trend.

The amplitude ratio (*Xr*) between the cold- and the hot-side bellows shows the characteristics of a second-order system. In the air tests, the *Xr*s follow the same trend with the maximum value of 2.5 near the natural frequency. For the helium tests, the *Xr* curves are flatter, and for the case of 1 atm, it has a smaller maximum value of 2.0 compared with the air test. The data suggest that the change from air to helium affect primarily the increase in the damping coefficient while leaving the spring constant essentially the same.

The amplitude of the pressure variations in the compression space (*P1*) is always larger than those of the expansion space (*P2*). The pressure drop is presence as the gas is transferred from the compression to the expansion space. In the compression space, the pressure ratio is maximum near the natural frequency as a result of the near 90 degree phase shift and high *Xr*. The maximum pressure ratios are 1.36 and 1.20 in the air test (*X1*=5.5mm) and the helium test (2 atm), respectively. For the same charge pressure, helium tests give lower pressure drop (nondimensionalized by the *P1*) and phase shift than the air tests. The maximum pressure drop of 70% of *P1* was found in the air test at a maximum *X1* of 5.5 mm. This suggests that the use of helium gives lower friction drop in some degree but the major factor affecting the pressure drop is the velocity of the gas flowing through the regenerator that comes from the combination of favorable phase shift and high *Xr*.

The temperature difference developed across the regenerator is an indication of

the cooling capacity. The temperature difference is at a maximum near the natural frequency where the *Xr* and the pressure ratio also peak. However, in this investigation, there are many parasitic losses. Good correlations were found between the expansion power (*PV2*) and the temperature difference for both air and helium tests. The cold-side temperature, however, is a result of interaction between cooling capacity, parasitic losses, heat exchanger performance and the ambient temperature. The minimum steady state cold-side temperature obtainable in this investigation is 14 °C although the instantaneous temperature of below 10 °C are possible when starting an experiment.

6.3) Enhanced performance by using helium

In the dynamic aspect, the major effect of using helium is the increase in the damping coefficient of the dynamic model as can be seen in the broader span of the phase shift and lower peak of the *Xr*. For example at 1 atm, the maximum amplitude ratios are 2.3 and 2.0 for the case of air and helium, respectively.

From a thermodynamic point of view, it was found that the pressure ratio in the compression space is almost the same for both gases at 1 atm. The maximum temperature difference, lowest cold-side temperature and indicated cooling potential (*PV2*) are all comparable for both air and helium tests although *Xr* is smaller in the helium tests. This may come partially from the reduced pressure drop loss (from 0.35 to 0.15 of the *P1*)in using helium instead of air. As a result, it can be seen that for a given size of cooler (limited *X2*), the use of helium gives higher *X1* and results in higher cooling capacity.

With the increased level of charge pressure to 2 atm, driven with the same *X1*, the helium charged cooler can develop up to 40 °C temperature difference compared with 20 °C at 1 atm. Therefore, with the use of at elevated charge pressure, higher cooling performance can be expected from the same compact package.

6.4 Energy balance

The indicated power was determined from the P-V diagram plotted directly from the working space data. The phase shift between the pressure and volume variation determines the sign of the indicated work. *X1* was found to lead *P1*. This means that the compression work was done by the driver on the hot side bellows. In the cold-side bellows, *P2* was found to lead *X2*. In this latter case, the expansion work was being done by the gas.

Both indicated powers show the maximum value near the natural frequency but the mechanisms for each variation are different. In the compression space where *X1* is kept constant, the phase shift of *X1* leads *P1* and increases with frequency. The maximum pressure ratio and close-to 90 degree phase shift maximizes the indicated power (*PV1*) near the natural frequency. In the expansion space, however, the phase shift of *P2* leads *X2* and are relatively constant for each test. The maximum pressure ratio and maximum *Xr* give the maximum indicated power (*PV2*) near the natural frequency.

The indicated power from the expansion space as an indicator of cooling potential is approximately 2-4 watts for the air case, and 3-7 watts for the helium case. The

summations of the indicated power in all four working spaces are almost always positive. It comes from the high value of *PV2*. The measured power needed to drive the cooler are however negative and indicates the necessary input power. The difference in these powers are the parasitic losses in the cooler. Five types of losses are important: regenerator loss, shuttle heat transfer loss, conduction and radiation loss, windage loss and friction loss. The isolation of these losses for detailed analysis was not possible in this investigation. An attempt however was made to estimate the level of windage and bellow spring hysteresis losses.

A bellow spring was oscillated with varying frequency for two levels of displacement amplitude. Other losses are deducted from the electrical power input and the magnitude of the windage and spring hysteresis losses is revealed. The magnitude of the losses reaches 3 watts with the displacement amplitude of 4.8 mm. Considering the maximum amplitude of 5.5 and 8.0 mm for the displacement of the hot- and the cold-side bellow, regardless of other losses, the magnitude of the windage and bellow spring hysteresis losses can reach a very high value- at least more than 3 watts. The maximum difference between the indicated power and the measured cooler power is 12 watts for the air test at the maximum *X1*. Similar results were found for the helium at the maximum charge pressure.

The total electrical power input varied from 10 to 45 watts in the air test. Approximately 50 to 75% of this power was consumed by Joule heating in the driver coil. Friction and windage losses was also found to increase with the amplitude of bellows and driving frequency and ranged from 20 to 40% of the total power input. Only 10 to 20%

of the power goes to cooler operation. For the helium test, the power input is in the order of 10 to 35 watts. The percentage of the power going to Joule heating, friction and windage loss and the cooler are 60-70%, 10-20% and 10-20% respectively.

Two performance indices were investigated: the cooler *COP* defined by the ratio of *PV2* to the measured cooler power input and the thermodynamic *COP* defined by the ratio of *PV2* to the driver power input. Both *COP*s show maximum values near the natural frequency. The maximum cooler *COP* is 0.18 for air at the maximum *X1* of 5.5 mm. The maximum *COP* of 0.22 was found for helium at 2 atm. For the thermodynamic *COP*, the maximum value are 1.6 and 1.2 for air at *X1*=5.5 mm and helium at 2 atm, respectively.

REFERENCES

Ackerman, R.A. 1981. 'Dynamic analysis of a small free-piston resonant cryorefrigerator'. NBS SP607 ed. J.E. Zimmerman, et al. May 1981 pp.57-69

Agbi, B. 1973. 'Theoretical and Experimental performance of the Beale free piston Stiring engine'. Proc. 8th Inter-Society Energy conversion Engineering Conf. 739034 pp.583-586

Atrey, M.D. et al. 1990. 'Cyclic simulation of Stirling cryocoolers'. Cryogenics. Vol.30 Apr 1990, pp.341-347

Azetsu, A., et al. 1984. 'Study on a two-piston type Stirling engine MELSE II—Analysis of engine performance'. Proc. 19th IECEC 849166 pp.2009-2014

Beale, W., J. Rauch and S. Lewis 1973. 'Design details and performance characteristics of some free-piston Stirling engine'. Proc. 8th IECEC 739077 pp.190-193

Benvenuto, G. and G. Bisio 1989. 'Thermoacoustic systems, Stirling engines and pulse-tube refrigerators:Analogies and differences in the light of generalized thermodynamics'. Proc. 24th IECEC 899046 pp.2413-2418

Benvenuto, G., et al. 1990. 'Dynamic behaviour prediction of free-piston Stirling engines'. Proc. 23th IECEC pp.346-351

Benvenuto, G., et al. 1991. 'Study of the response to load variation of a free-piston Stirling engine'. Proc. 26th IECEC pp.337-342

Berchowitz, D.M. 1988. 'Operational characteristics of free-piston Stirling engines'. Proc. 23thIECEC 889279 pp.107-112

Berchowitz, D.M. and G.F. Wyatt-Mair 1979. 'Closed-form solutions for a coupled ideal analysis of free-piston Stirling engines'. Proc. 14thIECEC 799241 pp.1114-1119

Bradshaw, T.W., et al. 1986. 'Performance of the Oxford miniature Stirling cycle refrigerator'. Adv.Cryo.Eng. 1986 Vol.31 pp.801-809

Carl, Shawn. 1996. 'Detecting Micron-size Movements'. Scientific American, Aug. 1996, pp.96-99

Chen, C.J. and F.P. Griffin 1983. 'Effects of pressure-drop correlations on Stirling engine predicted performance'. Proc. 18thIECEC 839114 pp.708-712

Chen, F.C. 1988. 'Testing of a Stirling cycle cooler'. Analysis and applications of heat pumps. AES Vol.8 p49-55 ASME. New York.

Cichy, M. 1984. 'Frequency dynamic analysis of free piston Stirling engines'. Proc. 19thIECEC 849048 pp.1829-1835

Colgate, S.A. and A.G. Petschek 1994. 'Regenerator optimization for Stirling cycle refrigeration'. Adv.Cryo.eng. Vol.39, pp.1351-1358

Das, R.L. and K.A. Bahrami 1979. 'Dynamics and control of Stirling engines in a 15 kWe solar electric generation concept'. Proc. 14thIECEC 799023 pp.133-138

Davey, G. and A.H. Orlowska 1987. 'Miniature Stirling cycle cooler'. Cryogenics. Vol. 27 Mar 1987, pp.148-151

de Jonge, A.K. 1979. 'A small free-piston Stirling refrigerator'. Proc. 14thIECEC 799245 pp.1136-1141

Dochat, G., et al. 1980. '1-kWe free-piston Stirling engine/Linear alternator test program'. Proc. 15thIECEC 809400 pp.1976-1981

Guo, F.Z. et al. 1987. 'Flow characteristics of a cyclic flow regenerator'. Cryogenics. Vol.27 Mar 1987, pp.152-155

Hamaguchi, K., et al. 1991. 'Effects of regenerator size changes on Stirling engine performance'. Proc. 26th IECEC Vol.5 pp.293-298

Ho, R.C.C., et al. 1980. 'Nodal Analysis of miniature cryogenic coolers'. Proc. 15th IECEC 809452 pp.2265-2273

Kagawa, N., et al. 1991. 'Design and development of a miniature Stirling machine'. Proc. 26th IECEC pp.192-197

Kankam, M.D. and J.S. Rauch 1991. 'Comparative survey of dynamic analyses of free-piston Stirling engines'. Proc. 26th IECEC pp.314-319

Kankam, M.D., et al. 1992. 'Dynamic analysis of free-piston Stirling engine/ Linear alternator-load system - Experimentally validated'. Proc. 27th IECEC 929265 pp.5.315-5.323

Kim, S.T., et al. 1993. 'Study of Stirling cycle refrigerator'. Proc. 29thIECEC 93091 pp.2.615-2.619

Kolin, I. 1984. 'Low temperature difference Stirling engine'. Proc. 19thIECEC 849029 pp.1807-1812

Louie, B. and R. Radebaugh 1984. 'The Stirling cycle and cryogenic refrigerators'. Proc. 19thIECEC 849414 pp.2086-2091

Mancini, T.R., et al. 1994. 'Solar thermal power today and tomorrow'. Mechanical Engineering. Vol.116 No.8, Aug 1994, pp.74-79

Martini, W.R. 1975. 'The free-displacer, free-piston Stirling engine- Potential energy conserver', Proc. 10thIECEC 759149 pp.995-1002

Martini, W.R. 1981. 'A potentially inexpensive, high performance Stirling-air engine'. Proc. 16thIECEC 819786 pp.1880-1885

Martini, W.R. 1983. 'Stirling engine design manual'. 2nd ed. NASA CR 168088

Martini, W.R. 1984. 'On the use of fully instrumented Stirling engines to validate mathematical models'. Proc. 19thIECEC 849017 pp.1788-1793

Miyabe, H., et al. 1982. 'An approach to the design of Stirling engine regenerator matrix using packs of wire gauzes'. Proc. 17th IECEC 829306 pp.1839-1844

Orlowska, A.H. and G. Davey 1987. 'Measurement of losses in a Stirling cycle cooler'. Cryogenics. Vol.27 Nov 1987, pp.645-651

Otaka, T. et al. 1993. 'Study of a 100 W class Stirling cycle cooler : Experimental results Proc. 29th IECEC 93239 pp.2.621-2.626

Reader, G.T. and C. Hooper 1983. 'Stirling engines'. University Press, Cambridge.

Redlich, R.W. and D.M.Berchowitz 1985. 'Linear dynamics of free-piston Stirling engines'. Proc. Instn. Mech. Engrs. Vol.199 No.A3 pp.203-213

Rifkin, W., et al. 1980. 'Applications of free-piston Stirling engines'. Proc. 15th IECEC 809401 pp.1982-1986

Teagan, W.P., et al. 1983. 'Stirling application study'. NASA CR168087

Tew, R.C., et al. 1990. 'Recent Stirling engine loss-understanding results'. Proc. 25th IECEC Vol.5 pp.377-385

Thirumaleshwar, M. and S.V. Subramanyam 1986a. 'Gifford-McMahon cycle-a theoretical analysis'. Cryogenics 1986 Vol.26 pp.182-187

Thirumaleshwar, M. and S.V. Subramanyam 1986b. 'Heat balance analysis of single stage Gifford-McMahon cycle cryorefrigerator'. Cryogenics 1986 Vol.26 pp.189-195

Tiehan, Z., et al. 1989. 'An investigation of cyclic flow pressure drop in Stirling cycle cryocooler regenerator'. Cryogenics and refrigerations-Proceeding of international conference. ed. Chen Guobang and Thomas M. Flynn. IAP 1989 pp.116-121

Urieli, I. and D.M.Berchowitz 1984. 'Stirling cycle engine analysis'. Adam Hilger Ltd, Bristol. Great Britain. 1984

Vincent, R., et al. 1980. 'Analysis and design of fpse-thermodynaics and dynamics'. Proc. 15th IECEC 809334 pp.1686-1695

Walker, G. 1980. 'Stirling engine'. Oxford University press, Oxford, England.

Walker, G. 1983. 'Cryocoolers'. 2 Vols.Plenum press, New York.

Walker, G. 1989. 'Miniature refrigerators for cryogenic sensors and cold electronics'. Oxford University Press, New York.

Walker, G. and J.R. Senft 1985. 'Free Piston Stirling Engine'. Springer-Verlag. Berlin, Heidelberg

Walker, G., et al. 1994. 'The Stirling alternative'. Gordon and Breach Science Publishers. Switzerland.

Walker, G., et al. 1979. 'Operating characteristics of a small Stirling engine'. Proc. 14th IECEC 799249 pp.1157-1161

Walker, G., et al. 1992. 'Stirling, Near-ambient temperature refrigerators: Innovative compact designs'. Proc. 28th IECEC 929035 pp.5.93-5.96

Wegeng, R.S. and M.K. Drost 1994. 'Developing new miniature energy systems'. Mechanical Engineering. Vol.116 No.9, Sept 1994, pp.82-85

West,C.D. 1986. 'Principles and applications of Stirling engines'. Van Nostrand Reinhold. New York.

APPENDICES

Appendix 1 : Analysis of mean formulation

The predicted formula is based on the linear relationship between the signal, y and the response, m.

$$y_{i,j} = \beta \cdot m_i \tag{A1.1}$$

where $i = 1,...,k$: k = number of data

$j = 1,...,r_o$: r_o = number of repetitions

By least square analysis, the sum square of variations can be calculated.

$$SS_v = \sum_i \sum_j (y_{i,j} - \beta \cdot m_i)^2 \tag{A1.2}$$

For the best value of beta, take the derivative

$$dSS_v / d\beta = -2 \sum \sum m_i (y_{i,j} - \beta m_i) = 0 \tag{A1.3}$$

Simplification gives

$$\beta = (\sum_i \sum_j m_i y_{i,j}) / r_o \sum_i m_i^2 \tag{A1.4}$$

or $$\beta = (\sum_j L_j) / r \tag{A1.5}$$

where $$r = r_o \sum_i m_i^2 \tag{A1.6}$$

$$L_j = \sum_i m_i y_{i,j} \tag{A1.7}$$

Appendix 2 : Analysis of mean : Air as a working fluid

Table A2.1 Experimental data for the cooler operating with air at 1 atm.

	Control Factor Settings					M1		M2		M3	
						N1	N2	N1	N2	N1	N2
Run	A	B	C	D							
1	1	1	1	1	T_h	29.1	29.5	32.2	32.6	34.5	35.55
					T_k	24.2	24.2	21	20.85	19.75	19.7
2	1	2	2	2	T_h	28.1	29.4	32.2	34.5	34.45	35.5
					T_k	21.1	22.4	19.45	20.1	18.8	20.15
3	1	3	3	3	T_h	29	29.8	33.5	33.7	36.45	36.65
					T_k	23.3	23.2	22.9	22.8	22.75	22.6
4	2	1	2	3	T_h	31.2	32.5	36.6	36.35	38.1	39.3
					T_k	23.8	23.9	22.6	22.5	21.95	21.8
5	2	2	3	1	T_h	30.2	29.6	34.8	34.1	37.6	38.1
					T_k	20.8	22.6	19.8	19.9	19.1	20.6
6	2	3	1	2	T_h	30	30.4	31.45	32.6	34	35.25
					T_k	24.9	25.4	23.35	23.95	22.6	23.45
7	3	1	3	2	T_h	25.7	26.3	27.45	27.85	29.2	29.45
					T_k	23.2	23.6	21.95	22.3	21	21.35
8	3	2	1	3	T_h	29.9	30.6	35.35	36.15	38.05	39.7
					T_k	22.9	23.2	21.9	21.5	21.5	20.9
9	3	3	2	1	T_h	29.7	29.8	36.4	35.35	39.1	39.85
					T_k	20.7	21.2	19.95	19.6	19.95	19.45

Table A2.2 The temperature difference for each control factor setttings.

ΔT	M1		M2		M3	
Run	N1	N2	N1	N2	N1	N2
1	4.9	5.3	11.2	11.75	14.75	15.85
2	7	7	12.75	14.4	15.65	15.35
3	5.7	6.6	10.6	10.9	13.7	14.05
4	7.4	8.6	14	13.85	16.15	17.5
5	9.4	7	15	14.2	18.5	17.5
6	5.1	5	8.1	8.65	11.4	11.8
7	2.5	2.7	5.5	5.55	8.2	8.1
8	7	7.4	13.45	14.65	16.55	18.8
9	9	8.6	16.45	15.75	19.15	20.4
verify 1	9.5	10.4	16.55	17.5	20.25	21.95
verify 2	6.75	7.75	13.35	14.15	16.2	16.2

Table A2.3 Analysis of mean for the temperature difference factor, β

Expr.	$L_{1,1}$	$L_{1,2}$	$L_{2,1}$	$L_{2,2}$	$L_{3,1}$	$L_{3,2}$	$\beta =$
1	30.63	33.13	179.2	188	368.8	396.3	**0.650**
2	43.75	43.75	204	230.4	391.3	383.8	**0.705**
3	35.63	41.25	169.6	174.4	342.5	351.3	**0.606**
4	46.25	53.75	224	221.6	403.8	437.5	**0.754**
5	58.75	43.75	240	227.2	462.5	437.5	**0.799**
6	31.88	31.25	129.6	138.4	285	295	**0.495**
7	15.63	16.88	88	88.8	205	202.5	**0.335**
8	43.75	46.25	215.2	234.4	413.8	470	**0.774**
9	56.25	53.75	263.2	252	478.8	510	**0.877**
						avg. β	0.666
verify 1	59.38	65	264.8	280	506.3	548.8	**0.937**
verify 2	42.19	48.44	213.6	226.4	405	405	**0.729**

Table A2.4 Determination of the average control factor effects on the temperature difference.

C/F					Control factor settings										
1	2	3	4	β	1/1	1/2	1/3	2/1	2/2	2/3	3/1	3/2	3/3	4/1	4/2	4/3
1	1	1	1	0.650	0.65	0	0	0.65	0	0	0.65	0	0	0.65	0	0
1	2	2	2	0.705	0.705	0	0	0	0.705	0	0	0.705	0	0	0.705	0
1	3	3	3	0.606	0.606	0	0	0	0	0.606	0	0	0.606	0	0	0.606
2	1	2	3	0.754	0	0.754	0	0.754	0	0	0	0.754	0	0	0	0.754
2	2	3	1	0.799	0	0.799	0	0	0.799	0	0	0	0.799	0.799	0	0
2	3	1	2	0.495	0	0.495	0	0	0	0.495	0.495	0	0	0	0.495	0
3	1	3	2	0.335	0	0	0.335	0.335	0	0	0	0	0.335	0	0.335	0
3	2	1	3	0.774	0	0	0.774	0	0.774	0	0.774	0	0	0	0	0.774
3	3	2	1	0.877	0	0	0.877	0	0	0.877	0	0.877	0	0.877	0	0
				avg.	0.653	0.683	**0.66**	*0.58*	**0.76**	0.659	0.64	**0.78**	0.58	*0.78*	0.512	**0.71**

Table A2.5 Analysis of mean for the cold-side temperature factor, β'

	M1 = 6.25		M2 = 16		M3 = 25		ANOM	β'
Expr.	N1	N2	N1	N2	N1	N2		
1	24.2	24.2	21	20.85	19.75	19.7		**1.06**
2	21.1	22.4	19.45	20.1	18.8	20.15		**1.02**
3	23.3	23.2	22.9	22.8	22.75	22.6		**1.17**
4	23.8	23.9	22.6	22.5	21.95	21.8		**1.15**
5	20.8	22.6	19.8	19.9	19.1	20.6		**1.03**
6	24.9	25.4	23.35	23.95	22.6	23.45		**1.21**
7	23.2	23.6	21.95	22.3	21	21.35		**1.12**
8	22.9	23.2	21.9	21.5	21.5	20.9		**1.11**
9	20.7	21.2	19.95	19.6	19.95	19.45		**1.02**
							avg. $\beta =$	1.10
verify1	20.1	20.1	18.9	18.9	18.1	18.2		**0.958**

Table A2.6 Determination of the average control factor effects on the cold-side temperature.

C/F					Control factor settings											
1	2	3	4	β	1/1	1/2	1/3	2/1	2/2	2/3	3/1	3/2	3/3	4/1	4/2	4/3
1	1	1	1	1.064	1.064	0	0	1.064	0	0	1.064	0	0	1.064	0	0
1	2	2	2	1.021	1.021	0	0	0	1.021	0	0	1.021	0	0	1.021	0
1	3	3	3	1.171	1.171	0	0	0	0	1.171	0	0	1.171	0	0	1.171
2	1	2	3	1.149	0	1.149	0	1.149	0	0	0	1.149	0	0	0	1.149
2	2	3	1	1.032	0	1.032	0	0	1.032	0	0	0	1.032	1.032	0	0
2	3	1	2	1.208	0	1.208	0	0	0	1.208	1.208	0	0	0	1.208	0
3	1	3	2	1.119	0	0	1.119	1.119	0	0	0	0	1.119	0	1.119	0
3	2	1	3	1.110	0	0	1.11	0	1.11	0	1.11	0	0	0	0	1.11
3	3	2	1	1.021	0	0	1.021	0	0	1.021	0	1.021	0	1.021	0	0
				avg.	1.085	1.129	**1.08**	1.111	**1.05**	1.134	1.127	**1.06**	1.107	**1.04**	1.116	1.143

Appendix. 3 : Analysis of mean : Helium as a working fluid

Table A3.1 Experimental data for the cooler operating with Helium at 1 atm.

	Control factor				M1=2.5		M2=4.0		M3=5.0	
Experiment	1	2	3	4	T_k	T_h	T_k	T_h	T_k	T_h
1	1	1	1	x	20.5	28.05	18.85	33.35	18.3	36.25
2	1	2	2	x	20.0	28.1	18.8	33.5	18.25	37.5
3	1	3	3	x	24.3	30.0	23.55	34.8	23.25	38.2
4	2	1	2	x	19.75	27.8	18.8	34.55	18.2	39.35
5	2	2	3	x	22.55	31.15	21.25	35.95	21.2	39.5
6	2	3	1	x	21.95	29.0	21.4	32.45	21.2	35.5
7	3	1	3	x	23.2	29.0	21.5	33.05	20.75	35.95
8	3	2	1	x	20.4	30.3	19.15	34.1	18.5	37.75
9	3	3	2	x	20.8	26.95	19.8	31.7	19.3	35.0
Verify1	3	2	2	x	20.1	29.95	18.9	34.4	18.15	38.25
Verify2	2	2	2	x	24.05	30.25	22.25	34.4	21.45	37.8

Table A3.2 The temperature difference for each control factor setttings.

Experiment	1	2	3	4	dT1	dT2	dT3
1	1	1	1	x	7.55	14.5	17.95
2	1	2	2	x	8.1	14.7	19.25
3	1	3	3	x	5.7	11.25	14.95
4	2	1	2	x	8.05	15.75	21.15
5	2	2	3	x	8.6	14.7	18.3
6	2	3	1	x	7.05	11.05	14.3
7	3	1	3	x	5.8	11.55	15.2
8	3	2	1	x	9.9	14.95	19.25
9	3	3	2	x	6.15	11.9	15.7
Verify1	3	2	2	x	9.85	15.5	20.1
Verify2	2	2	2	x	6.2	12.15	16.35

Table A3.3 Analysis of mean for the temperature difference factor, β

Expr.	L_j			β
1	47.1875	232	448.75	0.7912
2	50.625	235.2	481.25	0.8337
3	35.625	180	373.75	0.6406
4	50.3125	252	528.75	0.9033
5	53.75	235.2	457.5	0.8113
6	44.0625	176.8	357.5	0.6286
7	36.25	184.8	380	0.6533
8	61.875	239.2	481.25	0.8503
9	38.4375	190.4	392.5	0.6753
			avg. β =	0.75417
verify 1	61.5625	248	502.5	0.8826
verify 2	38.75	194.4	408.75	0.6977

Table A3.4 Determination of the average control factor effects on the β

Control factor													
1	2	3	4	β	CF1/1	CF1/2	CF1/3	CF2/1	CF2/2	CF2/3	CF3/1	CF3/2	CF3/3
1	1	1	1	0.791	0.791	0	0	0.791	0	0	0.791	0	0
1	2	2	2	0.834	0.834	0	0	0	0.834	0	0	0.834	0
1	3	3	3	0.641	0.641	0	0	0	0	0.641	0	0	0.641
2	1	2	3	0.903	0	0.903	0	0.903	0	0	0	0.903	0
2	2	3	1	0.811	0	0.811	0	0	0.811	0	0	0	0.811
2	3	1	2	0.629	0	0.629	0	0	0	0.629	0.629	0	0
3	1	3	2	0.653	0	0	0.653	0.653	0	0	0	0	0.653
3	2	1	3	0.850	0	0	0.85	0	0.850	0	0.85	0	0
3	3	2	1	0.675	0	0	0.675	0	0	0.675	0	0.675	0
				avg.	0.755	**0.781**	0.730	0.783	**0.830**	0.648	0.757	**0.800**	0.702

Table A3.5 Analysis of mean for the cold-side temperature factor, β'.

	M1	M2	M3	β'
Expr.	Tk	Tk	Tk	
1	20.5	18.85	18.3	**0.9643**
2	20.0	18.8	18.25	**0.9587**
3	24.3	23.55	23.25	**1.2064**
4	19.75	18.8	18.2	**0.9556**
5	22.55	21.25	21.2	**1.0988**
6	21.95	21.4	21.2	**1.0973**
7	23.2	21.5	20.75	**1.0953**
8	20.4	19.15	18.5	**0.9743**
9	20.8	19.8	19.3	**1.01**
			avg. β' =	1.04008
verify 1	20.1	18.9	18.15	**0.9584**
verify 2	6.2	12.15	16.35	**0.6977**

Table A3.6 Determination of the average control factor effects on the cold-side temperature.

CF1	2	3	4	β'	CF1/1	CF1/2	CF1/3	CF2/1	CF2/2	CF2/3	CF3/1	CF3/2	CF3/3
1	1	1	1	0.964	0.964	0	0	0.964	0	0	0.964	0	0
1	2	2	2	0.959	0.959	0	0	0	0.959	0	0	0.959	0
1	3	3	3	1.206	1.206	0	0	0	0	1.206	0	0	1.206
2	1	2	3	0.956	0	0.956	0	0.956	0	0	0	0.956	0
2	2	3	1	1.099	0	1.099	0	0	1.099	0	0	0	1.099
2	3	1	2	1.097	0	1.097	0	0	0	1.097	1.097	0	0
3	1	3	2	1.095	0	0	1.095	1.095	0	0	0	0	1.095
3	2	1	3	0.974	0	0	0.974	0	0.974	0	0.974	0	0
3	3	2	1	1.010	0	0	1.01	0	0	1.01	0	1.01	0
				average	1.043	1.051	**1.030**	**1.010**	**1.010**	1.105	1.012	**0.970**	1.133

Table A3.7 Additional test on the effect of orifice on the temperature difference.

a) Raw Data

				2.5 V		4 V		5 V	
Orifice	Wire	Weight	Mass	Tk	Th	Tk	Th	Tk	Th
None	4	2	2	24.8	26.4	21.6	31.9	20.3	36.3
Small	4	2	2	24.5	25.9	21.8	29.8	20.3	34.1
Large	4	2	2	25.0	26.8	21.8	31.9	20.5	35.9

b) Temperature difference and the calculated temperature difference factor, β.

Orifice	2.5 V	4 V	5 V	β
None	1.6	10.3	16.0	0.606
Small	1.4	8.0	13.8	0.524
Large	1.8	10.1	15.4	0.625

c) Cold-side temperature and the calculated cold-side temperature factor, β'.

Orifice	2.5 V	4 V	5 V	β'
None	24.8	21.6	20.3	1.096
Small	24.5	21.8	20.3	1.097
Large	25.0	21.8	20.5	1.106

Appendix 4 : Physical dimensions and weight of cooler components.

Cold side		Length(in)	Diameter(in)	V(in^3)
S1	Aluminium cylinder	1.103	2.195	4.174
S2	Plastic cyl	0.995	2.120	3.512
S3	End plate protrusion	0.050	2.120	0.176
	Plate recess			0.180
S4	Front plate			0.211
S5	Ballast(each of *3*)			0.145
C1	Bellow	0.950	1.637	1.999
C2	Inside plug	0.700	1.210	0.805

Gas spring Volume
5.189 in^3
8.503*10^{-5} m^3
Compression space
1.195 in^3
1.957*10^{-5} m^3

Regenerator	2.500	0.605	0.719

Regenerator Volume
0.719 in^3
1.178*10^{-5} m^3

Hot side				
S1	Aluminium cylinder	1.103	2.195	4.174
S2	Plastic cyl	1.135	2.120	4.006
S3	End plate protrusion	0.050	2.120	0.176
C1	Bellow	0.95	1.637	1.999
C2	Inside plug	0.6	1.000	0.679
S4	Hub for driver shaft	0.465	1.385	0.701
S5	Front bearing	0.435	1.385	0.655

Gas spring Volume
4.648 in^3
7.617*10^{-5} m^3
Expansion space
1.321 in^3
2.165*10^{-5} m^3

Weight

Hot-side bellow assembly	74.5	grams
Cold-side bellow assembly	110.9	grams
Bellow only (including magnet)	24.6	grams
Ballast ring	17.2	grams

Effective Cold-side bellow mass
110.9-24.6+(17.2*2) =
120.7 grams

Spring constant for both bellows	3250 N/m
Spring constant for cold-side gas spring (1 atm charged pressure)	3444 N/m
$k_g = \gamma \cdot A_p^2 \frac{P_m}{V_b} = 1.4 * 1.35e-3 * \frac{1.015e5}{7.61e-5}$	
Calculated natural frequency, $\omega_{n,c}$	37.5 Hz

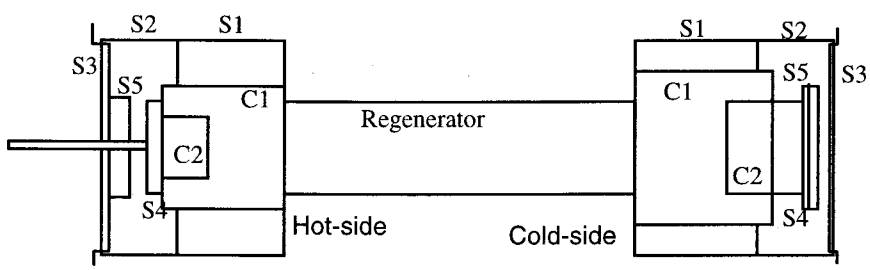

Fig. A4.1 Schematic for the cooler's dimension.

Appendix 5 : Circuitry for HET transducers.

The circuitry for Hall-effect transducer is based on the article 'Detecting Micron-size movements' by Shawn Carlson in the Scientific American, August 1996, pp.96-99. The Original circuits are shown in figure. A5.1, 2 and 3. The circuit for quickly varying signal is used. The low-pass filter in the Fig. A5.3. was dropped out after giving no output signal in the preliminiary testing of the circuit. The power supply circuit was also found to be not workable and a new circuit was developed. The workable circuits are shown in Fig. A5.5 and A5.6.

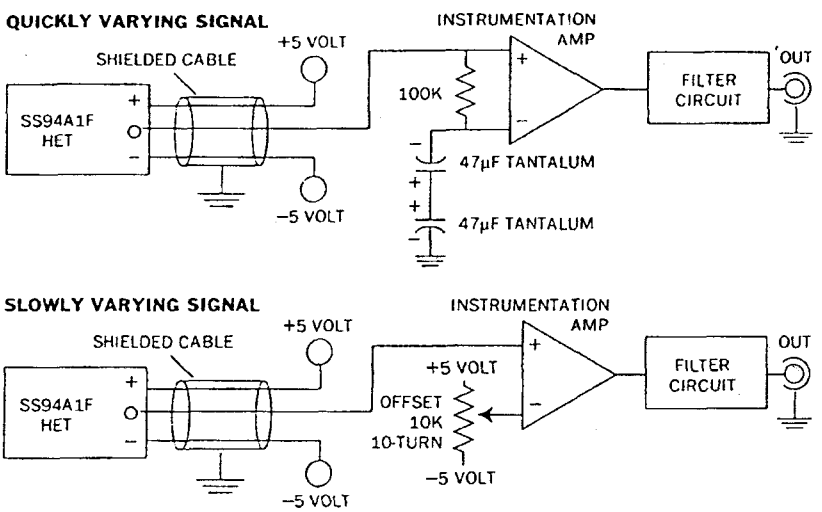

Fig. A5.1 HET circuit for quickly and slowly varying signal.

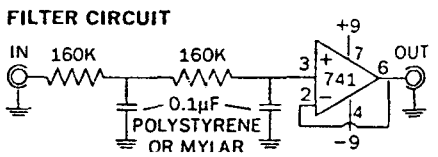

Fig. A5.2 Filter circuit and power supply circuit.

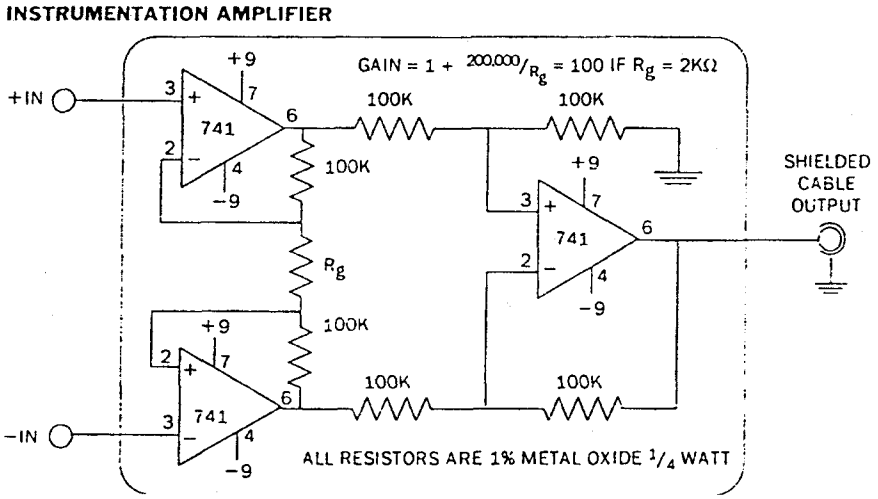

Fig. A5.3 Circuit for instrumentation amplifier.

In this investigation, the HET transducers are the model SS94A1F from Honeywell MicroSwitch. The HET is powered by +/- 5 volts voltage from the power supply circuit. The small varying signal (from the motion of the bellow) riding on top of a large constant voltage (from earth electromagnetic force and other environmental sources) is amplified by the instrumentation amplifier model AD524 from Analog Devices. The suitable amplifying gain for the HET setup used is 100.

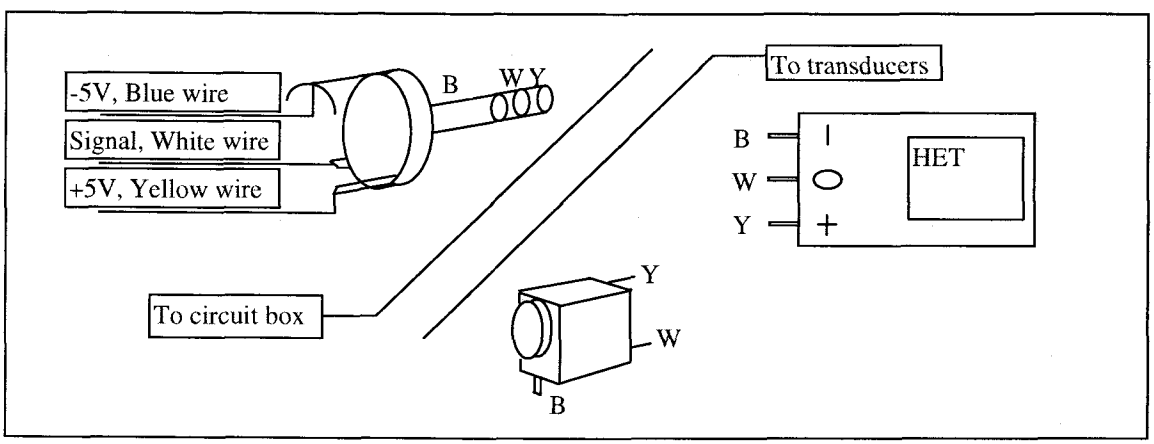

Fig. A5.4 Wiring for the Hall-effect transducer.

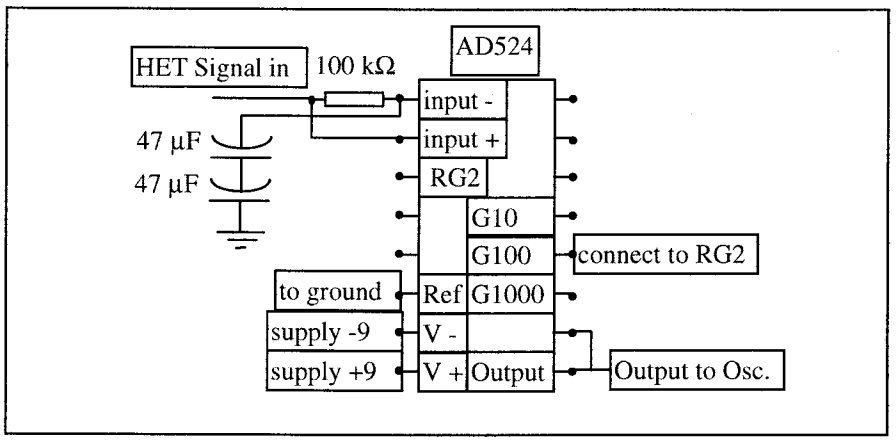

Fig. A5.5 Operating connections for $G = 100$.

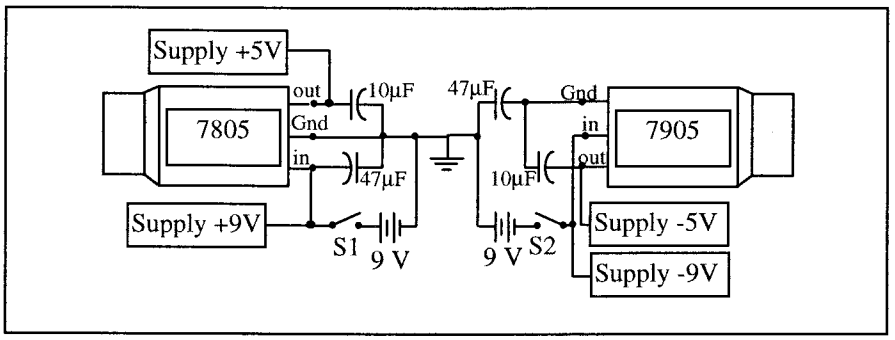

Fig. A5.6 Power supply circuit.

Appendix 6 : Calibration curve for HET transducers.

Table A6.1 Hot-side HET calibration curve.

Reading			Displacement					
Plus side (in)	Minus side (in)	Voltage (V)	(+) (in)	(-) (in)	Amplitude (mm)	Voltage (V)	Predicted (mm)	%error
0.918	1.306	0	0	0	0	0	0.521	
0.885	1.336	0.632	0.033	0.03	1.6	0.632	1.783	11.4
0.869	1.3505	0.92	0.049	0.0445	2.375	0.92	2.357	-0.7
0.853	1.3625	1.248	0.065	0.0565	3.086	1.248	3.012	-2.4
0.844	1.373	1.5	0.074	0.067	3.581	1.5	3.515	-1.9
0.833	1.3845	1.78	0.085	0.0785	4.153	1.78	4.073	-1.9
0.823	1.3965	2.08	0.095	0.0905	4.712	2.08	4.672	-0.8
0.815	1.4055	2.28	0.103	0.0995	5.144	2.28	5.071	-1.4
0.807	1.4115	2.5	0.111	0.1055	5.499	2.5	5.510	0.19
0.798	1.4235	2.76	0.12	0.1175	6.033	2.76	6.029	-0.06
0.794	1.424	2.9	0.124	0.118	6.147	2.9	6.308	2.6
					m= 1.995	b= 0.5217		

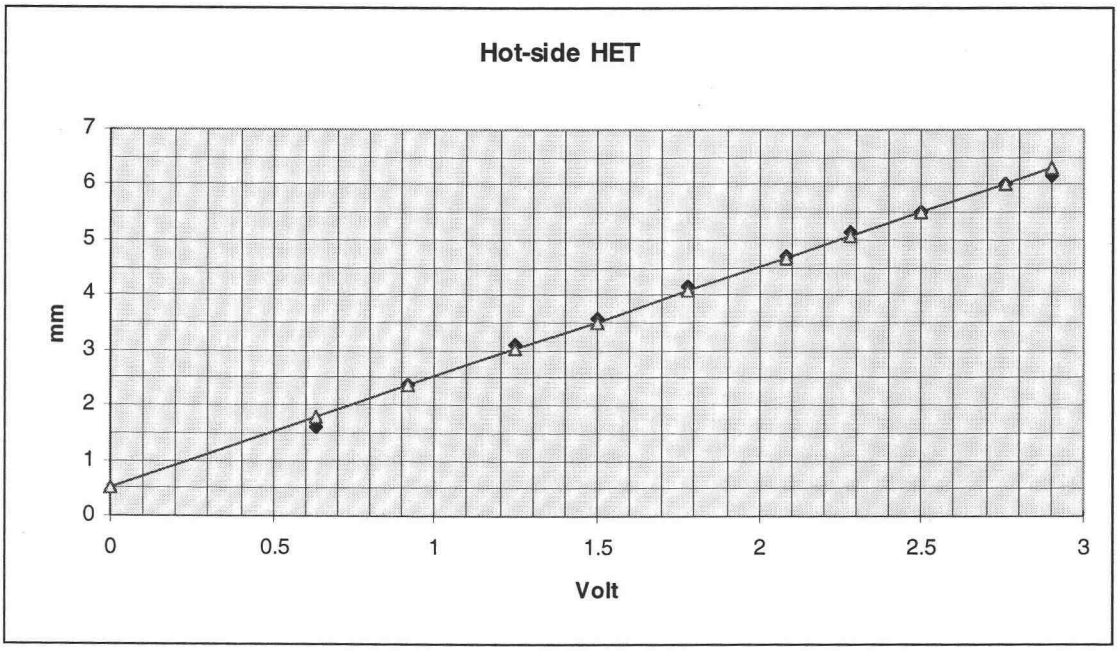

Fig. A6.1. Hot-side HET : Predicted mm = *V**1.955+0.522

Table A6.2 Cold-side HET calibration curve.

Reading (in)	Voltage (V)
0.664	0
0.682	1.78
0.692	3.06
0.6855	2.42
0.696	3.48
0.699	3.64
0.707	4.56
0.7185	5.48
0.7215	5.84
0.7315	6.84
0.742	7.84
0.752	8.88
0.761	9.6
0.771	10.48

Amplitude (mm)	Voltage (V)	Predicted (mm)	%error
0	0	-0.1555	
0.9144	1.78	0.783	14.4
1.4224	3.06	1.457	-2.5
1.0922	2.42	1.120	-2.6
1.6256	3.48	1.679	-3.3
1.778	3.64	1.763	0.84
2.1844	4.56	2.248	-2.9
2.7686	5.48	2.733	1.3
2.921	5.84	2.923	-0.06
3.429	6.84	3.450	-0.61
3.9624	7.84	3.977	-0.37
4.4704	8.88	4.525	-1.2
4.9276	9.6	4.905	0.47
5.4356	10.48	5.369	1.2
m=	b=		
0.5271	-0.1555		

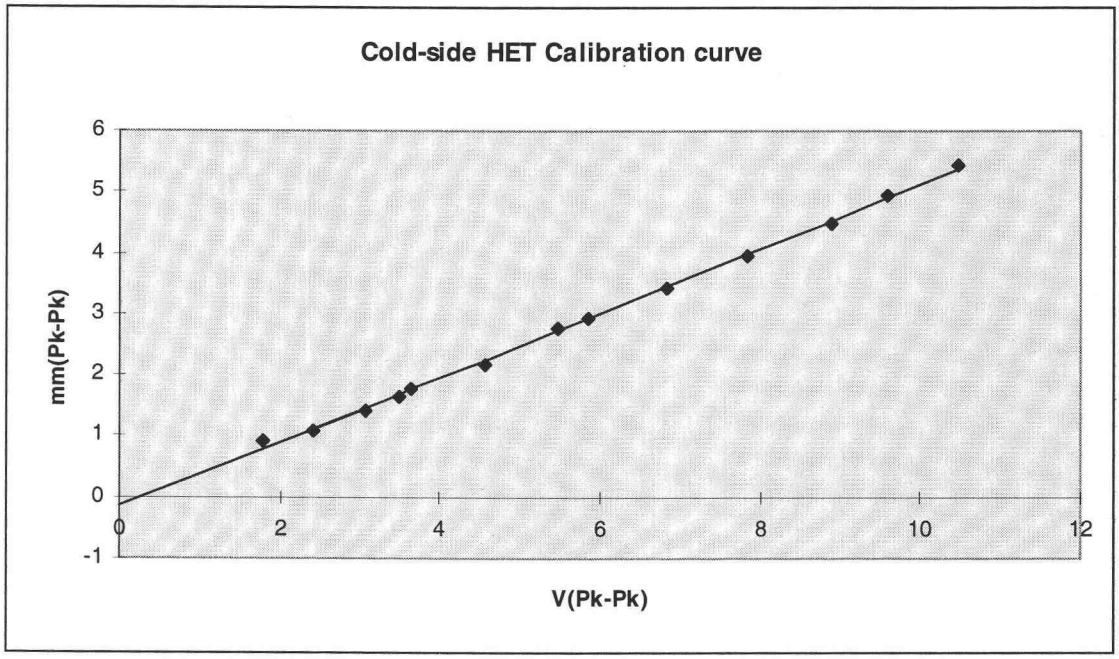

Fig. A6.2. Cold-side HET : Predicted mm = *V**0.5271-0.1555

Appendix 7 : Circuitry / calibration curves for the pressure transducers.

The circuit for the pressure transducers is basically the same as the one for the HET in Appendix 5. The voltage regulator is not needed because the pressure transducers need the excitation voltage of 10 V dc with maximum of 16 V dc. The 12 V battery pack is therefore enough for both the transducers and instrumentation amplifiers.

For this investigation, there are some tests being done above atmospheric pressure. To measure the pressure variation on top of the elevated mean pressure, the filter circuit is added to the circuit to filter out the constant charged pressure and pass only the variation of the pressure. The filter circuit is shown in Fig. A7.2

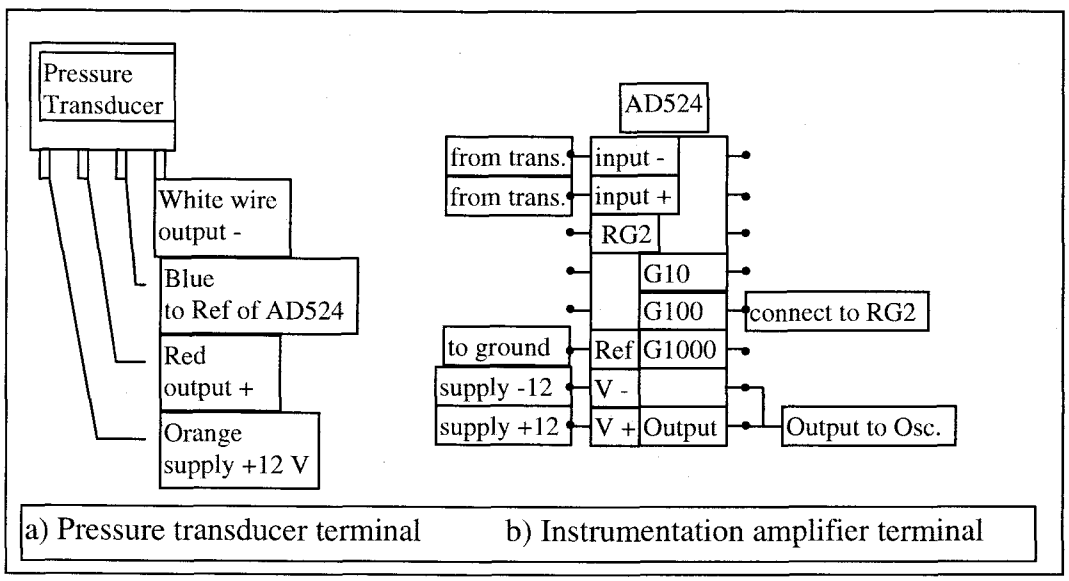

Fig. A7.1 Circuitry for the pressure transducers.

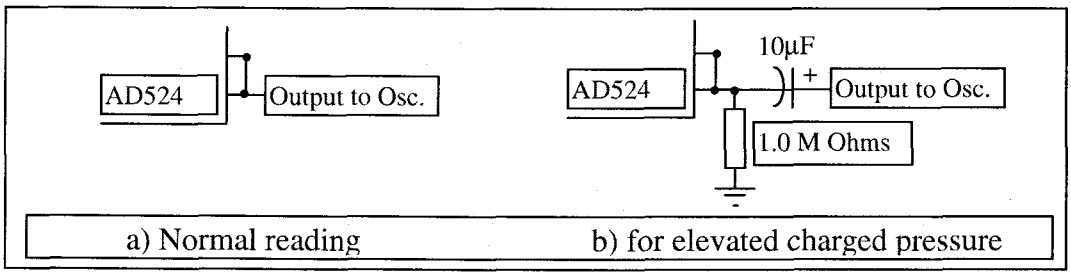

Fig. A7.2 Filter circuit

Table A7.1 Calibration data for the pressure transducer no.1.

No signal Pressure	Signal (V) 120-160 mV		Pressure	Predict1: p = 61.46*100*V	
psig		dV1	(N/m^2)	(N/m^2)	%error
0	-0.24				
2.5	2.48	2.72	17237	16718	3.0
5	5.32	5.56	34474	34173	0.87
7.5	8.16	8.4	51711	51629	0.16
10	11	11.24	68947	69085	-0.20
12.5	13.8	14.04	86184	86294	-0.13
15	16.6	16.84	103421	103504	-0.08
17.5	19.4	19.64	120658	120714	-0.05
20	22.2	22.44	137895	137923	-0.02
22.5	25	25.24	155132	155133	0.00
25	27.8	28.04	172368	172343	0.015
27.5	30.8	31.04	189605	190781	-0.62
30	33.4	33.64	206842	206762	0.039

Table A7.2 Calibration data for the pressure transducer no.2.

No signal Pressure	Signal (V) 0-40 mV		Pressure	Predict2: p = 60.76*100*V	
psig		dV2	(N/m^2)	(N/m^2)	%error
0	0.04				
2.5	2.84	2.8	17237	17014	1.3
5	5.72	5.68	34474	34514	-0.12
7.5	8.56	8.52	51711	51771	-0.12
10	11.4	11.36	68947	69029	-0.12
12.5	14.2	14.16	86184	86043	0.16
15	17	16.96	103421	103057	0.35
17.5	19.8	19.76	120658	120071	0.49
20	22.8	22.76	137895	138300	-0.29
22.5	25.6	25.56	155132	155315	-0.12
25	28.4	28.36	172368	172329	0.023
27.5	31.4	31.36	189605	190558	-0.50
30	34	33.96	206842	206357	0.23

Appendix 8 : Experimental data on RCAS test on air at 1 atm
with *X1* = 2.35, 3.25, 5.5 mm.

Table A8.1 Basic operating parameter : *X1*=2.35 mm

Freq	X1	X2	P1	P2	P3	P4	X2 leads X1	P1 leads X1	P2 leads X2	P3 leads X1	P4 leads X2
Hz	mm	mm	N/m^2	N/m^2	N/m^2	N/m^2	degree	degree	degree	degree	degree
49.5	2.36	4.74	10079	7631	4425	11058	-58.8	-108.7	119.4	178.2	-1.8
50.5	2.36	5.37	13521	8992	4228	12152	-78.2	-125.5	118.2	181.8	-1.8
52.1	2.36	4.99	14382	9381	4031	11180	-105	-146.3	116.3	183.8	3.8
53.2	2.36	3.77	12415	8409	4130	8506	-122.6	-164.7	114.9	183.8	3.8
54.9	2.34	2.75	9759	7242	4031	6367	-128.6	-172.1	116.7	189.9	5.9
56.8	2.34	2.33	9317	6950	4474	5346	-126.8	-180	110.5	184.1	0

Table A8.2 Basic operating parameter : *X1*=3.25 mm

Freq	X1	X2	P1	P2	P3	P4	X2 leads X1	P1 leads X1	P2 leads X2	P3 leads X1	P4 leads X2
Hz	mm	mm	N/m^2	N/m^2	N/m^2	N/m^2	degree	degree	degree	degree	degree
50.5	3.27	8.17	19667	8263	6588	17985	-67.3	-107.3	103.6	181.8	-1.8
52.6	3.25	7.91	26551	12638	6785	19443	-108	-149.7	108	174.3	-1.9
53.8	3.28	6.31	22371	12030	6736	14461	-121.9	-164.5	106.5	189.7	-5.8
55.6	3.25	4.84	18807	10694	6932	10840	-132	-172	108	188	4
56.8	3.28	4.16	15980	6440	6686	8506.4	-135	-180	98.2	188.2	0
58.1	3.24	3.44	17209	9770	8149	8457.8	-142.3	-188.4	108.8	188.4	-4.2

Table A8.3 Basic operating parameter : *X1*=5.5 mm

Freq	X1	X2	P1	P2	P3	P4	X2 leads X1	P1 leads X1	P2 leads X2	P3 leads X1	P4 leads X2
Hz	mm	mm	N/m^2	N/m^2	N/m^2	N/m^2	degree	degree	degree	degree	degree
42.4	5.47	5.16	5359	2843	11063	11544	-15.3	-69.1	120.1	187.2	10.2
46.7	5.51	8.15	15119	4860	11923	19079	-28.6	-75.7	99.3	181.7	1.7
56.2	5.51	7.69	31222	11058	10817	17499	-135.5	-184	95.06	177.9	-10.1
56.8	5.51	6.38	29009	10572	10571	14704	-143.2	-180	102.3	167.7	4.1
58.8	5.51	5.12	25936	8846	10940	11666	-150.4	-188.5	99.5	165.2	2.1
62.5	5.47	3.89	23355	7777	11309	8943.9	-157.5	-193.5	99	157.5	4.5

Table A8.4 Indicated power from the P-V diagram area : *X1*=2.35 mm

	PV1	PV2	PV3	PV4	PV (1+2+3+4)
Hz	(W)	(W)	(W)	(W)	(W)
49.5	-0.77	1.50	0.0063	-0.0086	0.72
50.5	-0.97	2.02	0.012	-0	1.06
52.1	-0.67	2.09	0.030	-0.0045	1.45
53.2	-0.28	1.41	0.039	-0.024	1.14
54.9	-0.086	0.93	0.051	-0.030	0.87
56.8	-0.011	0.77	0.080	-0.032	0.81

Table A8.5 Indicated power from the P-V diagram area : *X1*=3.25 mm

	PV1	PV2	PV3	PV4	PV (1+2+3+4)
Hz	(W)	(W)	(W)	(W)	(W)
50.5	-2.53	3.28	0.039	-0.076	0.71
52.6	-1.47	4.67	0.098	-0.17	3.13
53.8	-0.95	3.59	0.17	-0.023	2.78
55.6	-0.39	2.29	0.22	-0.0019	2.11
56.8	-0.044	1.31	0.21	-0.0043	1.47
58.1	+0.048	1.57	0.27	-0.0024	1.88

Table A8.6 Indicated power from the P-V diagram area : *X1*=5.5 mm

	PV1	PV2	PV3	PV4	PV (1+2+3+4)
Hz	(W)	(W)	(W)	(W)	(W)
42.4	-1.09	0.55	0.49	-0.033	-0.083
46.7	-3.31	1.76	0.34	-0.041	-1.24
56.2	-1.22	4.71	0.62	-0.16	3.95
56.8	-1.01	3.79	0.39	-0.054	3.11
58.8	-0.01	2.66	0.48	-0.0051	3.12
62.5	+0.31	1.92	0.73	-0.0043	2.96

Table A8.7 Friction and windage power loss : *X1*=2.35 mm

	$PV3_f$	$PV1_f$	V_f	I_f	V_f*I_f	I_f^2R	Friction
Hz	(W)	(W)	(V)	(A)	(W)	(W)	(W)
49.5	0.074	0.14	3.74	1.58	5.91	3.74	1.95
50.5	0.092	0.15	3.76	1.66	6.24	4.13	1.86
52.1	0.094	0.16	3.77	1.61	6.07	3.89	1.93
53.2	0.091	0.17	4.01	1.71	6.86	4.39	2.21
54.9	0.10	0.17	4.07	1.69	6.88	4.28	2.32
56.8	0.16	0.20	4.13	1.65	6.81	4.08	2.42

Table A8.8 Friction and windage power loss : *X1*=3.25 mm

	$PV3_f$	$PV1_f$	V_f	I_f	V_f*I_f	I_f^2R	Friction
Hz	(W)	(W)	(V)	(A)	(W)	(W)	(W)
50.5	0.20	0.48	5.33	2.12	11.3	6.74	3.87
52.6	0.23	0.53	5.54	2.1	11.6	6.62	4.26
53.8	0.23	0.57	5.69	2.16	12.3	7.00	4.49
55.6	0.26	0.59	5.52	1.93	10.7	5.59	4.22
56.8	0.27	0.53	5.89	2.19	12.9	7.19	4.90
58.1	0.34	0.64	6.14	2.26	13.9	7.66	5.23

Table A8.9 Friction and windage power loss : *X1*=5.5 mm

	$PV3_f$	$PV1_f$	V_f	I_f	V_f*I_f	I_f^2R	Friction
Hz	(W)	(W)	(V)	(A)	(W)	(W)	(W)
42.4	0.56	0.14	7.36	3.04	22.4	13.86	7.81
46.7	0.64	0.28	7.93	2.95	23.4	13.05	9.42
56.2	1.01	1.17	9.03	3.03	27.4	13.77	11.41
56.8	0.98	0.94	9.17	3.05	28	13.95	12.09
58.8	1.08	2.15	9.72	3.2	31.1	15.36	12.51
62.5	1.37	3.37	10.4	3.44	35.9	17.75	13.38

Table A8.10 Power distribution : *X1*=2.35 mm

	V	I	Electrical Input, VI	I^2R Loss	Friction	Cooler Power	PV Power	T_h	T_k	dT
Hz	(V)	(A)	(W)	(W)	(W)	(W)	(W)	(C)	(C)	(C)
49.5	4.72	2.24	10.57	7.53	1.95	1.10	0.72	37.8	19.8	18
50.5	5.02	2.46	12.35	9.08	1.86	1.41	1.06	43.4	20.8	22.6
52.1	5	2.47	12.35	9.15	1.93	1.27	1.45	43.6	19.4	24.2
53.2	4.82	2.29	11.04	7.87	2.21	0.96	1.14	40.2	19.9	20.3
54.9	4.72	2.21	10.43	7.33	2.32	0.79	0.87	37.1	18.2	18.9
56.8	4.81	2.13	10.25	6.81	2.42	1.02	0.81	35	18	17

Table A8.11 Power distribution : *X1*=3.25 mm

	V	I	Electrical Input, VI	I^2R Loss	Friction	Cooler Power	PV Power	T_h	T_k	dT
Hz	(V)	(A)	(W)	(W)	(W)	(W)	(W)	(C)	(C)	(C)
50.5	7.02	3.17	22.25	15.07	3.87	3.31	0.71	52.3	19.9	32.4
52.6	7.67	3.36	25.77	16.93	4.26	4.58	3.13	63	18.6	44.4
53.8	6.84	2.92	19.97	12.79	4.49	2.70	2.78	57.9	16.7	41.2
55.6	6.92	2.85	19.72	12.18	4.22	3.32	2.11	53.5	17.9	35.6
56.8	6.43	2.54	16.33	9.68	4.90	1.75	1.47	47.2	17.5	29.7
58.1	7.39	2.81	20.77	11.84	5.23	3.69	1.88	47.3	16.6	30.7

Table A8.12 Power distribution : *X1*=5.5 mm

	V	I	Electrical Input, VI	I^2R Loss	Friction	Cooler Power	PV Power	T_h	T_k	dT
Hz	(V)	(A)	(W)	(W)	(W)	(W)	(W)	(C)	(C)	(C)
42.4	7.37	2.65	19.53	10.53	7.81	1.19	-0.083	40.7	24.7	16
46.7	9.58	3.73	35.73	20.87	9.42	5.44	-1.24	53	23.3	29.7
56.2	10.8	4.07	43.92	24.85	11.41	7.66	3.95	71.9	13.9	58
56.8	10.9	3.96	43.05	23.52	12.09	7.43	3.11	65.6	15	50.6
58.8	11.2	3.98	44.70	23.76	12.51	8.43	3.12	57	14.7	42.3
62.5	11.6	3.9	45.08	22.81	13.38	8.89	2.96	48.6	16.2	32.4

Table A8.13 Windage and bellow spring hysteresis loss : X = 2.4 mm.

a) Raw data

	Run with bellow		Run without bellow	
Hz	Voltage (V)	Current (amp)	Voltage (V)	Current (amp)
62	4.16	1.77	3.58	1.16
58	3.6	1.42	3.31	1.05
55	3.35	1.25	3.065	0.96
52	2.98	1.04	2.903	0.9
50	2.77	0.94	2.685	0.83
48	2.7	0.89	2.588	0.8
46	2.518	0.81	2.466	0.77

b) Processed data

	Run with bellow		Run without bellow		
Hz	Input (W)	I^2R (W)	Input (W)	I^2R (W)	Windage and Hysteresis loss (W)
62	7.36	4.70	4.15	2.02	0.53
58	5.11	3.02	3.48	1.65	0.27
55	4.19	2.34	2.94	1.38	0.28
52	3.10	1.62	2.61	1.22	0.079
50	2.60	1.33	2.23	1.03	0.083
48	2.40	1.19	2.07	0.96	0.10
46	2.04	0.98	1.90	0.89	0.046

Table A8.14 Windage and bellow spring hysteresis loss : $X = 4.8$ mm.

a) Raw data

	Run with bellow		Run without bellow	
Hz	Voltage (V)	Current (amp)	Voltage (V)	Current (amp)
62	8.65	3.61	7.19	2.28
58	7.41	2.9	6.66	2.06
55	6.78	2.5	6.21	1.9
52	6.05	2.11	5.83	1.77
50	5.61	1.89	5.44	1.63
48	5.42	1.77	5.18	1.56
46	5.01	1.59	5.03	1.52

b) Processed data

	Run with bellow		Run without bellow		
Hz	Input (W)	I^2R (W)	Input (W)	I^2R (W)	Windage and Hysteresis loss (W)
62	31.23	19.55	16.39	7.80	3.08
58	21.49	12.62	13.72	6.37	1.52
55	16.95	9.38	11.80	5.42	1.19
52	12.77	6.68	10.32	4.70	0.47
50	10.60	5.36	8.87	3.99	0.36
48	9.59	4.70	8.08	3.65	0.46
46	7.97	3.79	7.63	3.47	0.01

Table A8.15 Coefficient of performance : X1=2.35mm

	PV2	W_{motor}	W_{cooler}	COP_{cooler}	COP_{thermo}
Hz	(W)	(W)	(W)		
49.5	1.50	10.57	1.10	0.14	1.36
50.5	2.02	12.35	1.41	0.16	1.43
52.1	2.09	12.35	1.27	0.17	1.65
53.2	1.41	11.04	0.96	0.13	1.47
54.9	0.93	10.43	0.79	0.09	1.18
56.8	0.77	10.25	1.02	0.08	0.75

Table A8.16 Coefficient of performance : X1=3.25mm

	PV2	W_{motor}	W_{cooler}	COP_{cooler}	COP_{thermo}
Hz	(W)	(W)	(W)		
50.5	3.28	22.25	3.31	0.15	0.99
52.6	4.67	25.77	4.58	0.18	1.02
53.8	3.59	19.97	2.70	0.18	1.33
55.6	2.29	19.72	3.32	0.12	0.69
56.8	1.30	16.33	1.75	0.08	0.75
58.1	1.57	20.77	3.69	0.08	0.42

Table A8.17 Coefficient of performance : X1=5.5mm

	PV2	W_{motor}	W_{cooler}	COP_{cooler}	COP_{thermo}
Hz	(W)	(W)	(W)		
42.4	0.55	19.53	1.19	0.03	0.47
46.7	1.76	35.73	5.44	0.05	0.32
56.2	4.71	43.92	7.66	0.11	0.61
56.8	3.79	43.05	7.43	0.09	0.51
58.8	2.66	44.70	8.43	0.06	0.32
62.5	1.92	45.08	8.89	0.04	0.22

Appendix 9 : Experimental data on RCAS test on helium at 1 atm, 7.5 psig, and 15 psig (*X1*=2.35 mm)

Table A9.1 Basic operating parameter : Helium 1 atm

Freq	X1	X2	P1	P2	P3	P4	X2 leads X1	P1 leads X1	P2 leads X2	P3 leads X1	P4 leads X2
Hz	mm	mm	N/m^2	N/m^2	N/m^2	N/m^2	degree	degree	degree	degree	degree
42	2.4	2.26	2826	2346	5439	5225	-16.6	-86.2	104.4	-19.7	13.6
46.7	2.4	3.57	6132	5439	5759	8425	-32.0	-65.6	139.6	-18.5	8.4
49	2.4	4.67	10984	9811	5759	11197	-52.9	-77.7	144.7	-14.1	7.1
51.5	2.4	4.79	14930	13463	5545	11730	-87.2	-102.1	146.6	-16.7	13.0
54.3	2.4	3.53	13597	12264	5492	8425	-109.6	-129.1	144.8	-15.7	7.8
58.8	2.4	2.33	11597	10504	5865	5332	-124.9	-141.9	141.9	-14.8	6.4

Table A9.2 Basic operating parameter : Helium 7.5 psig

Freq	X1	X2	P1	P2	P3	P4	X2 leads X1	P1 leads X1	P2 leads X2	P3 leads X1	P4 leads X2
Hz	mm	mm	N/m^2	N/m^2	N/m^2	N/m^2	degree	degree	degree	degree	degree
51.5	2.4	3.19	6345	5652	9078	11597	-20.4	-65.0	131.8	-9.3	1.9
54.9	2.4	4.63	14130	12797	9358	17329	-37.6	-65.3	144.4	-9.9	2.0
58.1	2.4	5.64	22394	19462	9131	20928	-71.2	-87.9	146.5	-8.4	8.4
63.3	2.4	4.71	24261	20928	8664	17596	-102.5	-116.2	143.5	-20.5	6.8
65.8	2.4	3.42	21328	18529	8904	12530	-118.4	-132.6	146.8	-18.9	9.5
69.4	2.4	2.47	19462	16663	9651	8904	-125	-140	140	-20	10

Table A9.3 Basic operating parameter : Helium 15 psig

Freq	X1	X2	P1	P2	P3	P4	X2 leads X1	P1 leads X1	P2 leads X2	P3 leads X1	P4 leads X2
Hz	mm	mm	N/m^2	N/m^2	N/m^2	N/m^2	degree	degree	degree	degree	degree
56.2	2.4	3.44	8424	7411	13730	17329	-14.2	-50.6	139.6	-18.2	10.1
61	2.4	5.09	20928	16796	14396	26793	-43.9	-61.5	140.5	-13.2	17.6
64.1	2.4	5.97	28926	23061	13997	30926	-55.4	-83.1	124.6	0	4.6
67.6	2.4	5.93	36524	27193	12264	30659	-87.6	-111.9	131.4	-4.9	4.9
70.4	2.4	4.79	33592	24661	11864	23861	-103.9	-129.3	129.3	-12.7	2.5
73.5	2.4	3.4	29859	21595	13063	16929	-121.8	-137.6	132.4	-21.2	15.8

Table A9.4 Indicated power from the P-V diagram area : Helium 1 atm

	PV1	PV2	PV3	PV4	PV (1+2+3+4)
Hz	(W)	(W)	(W)	(W)	(W)
42.0	-0.21	0.21	-0.135	0.073	-0.059
46.7	-0.45	0.59	-0.14	0.19	0.19
49.0	-0.89	1.25	-0.12	0.35	0.58
51.5	-1.29	1.74	-0.14	0.39	0.70
54.3	-1.07	1.24	-0.18	0.23	0.22
58.8	-0.79	0.71	-0.23	0.11	-0.20

Table A9.5 Indicated power from the P-V diagram area : Helium 7.5 psig

	PV1	PV2	PV3	PV4	PV (1+2+3+4)
Hz	(W)	(W)	(W)	(W)	(W)
51.5	-0.45	0.58	-0.26	0.25	0.12
54.9	-1.12	1.75	-0.25	0.54	0.92
58.1	-2.18	3.53	-0.23	0.88	2.00
63.3	-2.45	3.57	-0.29	0.67	1.49
65.8	-1.96	2.21	-0.38	0.39	0.26
69.4	-1.60	1.56	-0.48	0.23	-0.29

Table A9.6 Indicated power from the P-V diagram area : Helium 15 psig

	PV1	PV2	PV3	PV4	PV (1+2+3+4)
Hz	(W)	(W)	(W)	(W)	(W)
56.2	-0.65	0.92	-0.56	0.43	0.15
61.0	-1.99	3.82	-0.43	1.02	2.42
64.1	-3.30	5.58	-0.28	1.30	3.29
67.6	-4.21	7.66	-0.26	1.26	4.46
70.4	-3.37	5.80	-0.41	0.88	2.90
73.5	-2.52	4.01	-0.65	0.55	1.39

Table A9.7 Friction and windage power loss : Helium 1 atm (R = 1.5 Ohms)

	$PV3_f$	$PV1_f$	V_f	I_f	V_f*I_f	I_f^2R	Friction
Hz	(W)	(W)	(V)	(A)	(W)	(W)	(W)
42.0	0.15	0.25	3.94	1.95	7.68	5.70	1.58
46.7	0.17	0.28	4.19	1.94	8.13	5.65	2.03
49.0	0.18	0.29	4.31	1.9	8.19	5.42	2.30
51.5	0.22	0.36	4.61	1.93	8.9	5.59	2.74
54.3	0.23	0.38	4.76	1.91	9.09	5.47	3.01
58.8	0.28	0.41	5.26	1.99	10.5	5.94	3.85

Table A9.8 Friction and windage power loss : Helium 7.5 psig (R = 1.5 Ohms)

	$PV3_f$	$PV1_f$	V_f	I_f	V_f*I_f	I_f^2R	Friction
Hz	(W)	(W)	(V)	(A)	(W)	(W)	(W)
51.5	0.29	0.49	4.53	2.1	9.51	6.62	2.11
54.9	0.34	0.56	4.71	2.05	9.66	6.30	2.46
58.1	0.41	0.68	5.16	2.15	11.1	6.93	3.07
63.3	0.45	0.74	5.45	2.16	11.8	7.00	3.59
65.8	0.48	0.84	5.77	2.21	12.8	7.33	4.10
69.4	0.59	0.94	6.31	2.33	14.7	8.14	5.02

Table A9.9 Friction and windage power loss : Helium 15 psig (R = 1.5 Ohms)

	$PV3_f$	$PV1_f$	V_f	I_f	V_f*I_f	I_f^2R	Friction
Hz	(W)	(W)	(V)	(A)	(W)	(W)	(W)
56.2	0.63	0.94	5.34	2.45	13.1	9.00	2.51
61.0	0.63	1.02	5.75	2.46	14.1	9.08	3.42
64.1	0.75	1.18	6.1	2.49	15.2	9.30	3.96
67.5	0.79	1.30	6.34	2.49	15.8	9.30	4.40
70.4	0.84	1.45	6.78	2.59	17.6	10.06	5.21
73.5	1.03	1.43	7.23	2.68	19.4	10.77	6.14

Table A9.10 Power distribution : Helium 1 atm

	V	I	Electrical Input, VI	I^2R Loss	Friction	Cooler Power	PV Power	T_h	T_k	dT
Hz	(V)	(A)	(W)	(W)	(W)	(W)	(W)	(C)	(C)	(C)
42.0	3.97	1.78	7.07	4.75	1.58	0.74	-0.059	28.2	22.6	5.6
46.8	4.53	1.94	8.79	5.64	2.03	1.11	0.19	31	21.9	9.1
49.0	4.99	2.19	10.93	7.19	2.30	1.43	0.58	34.8	20.5	14.3
51.5	5.34	2.41	12.87	8.71	2.74	1.42	0.70	39.9	19.1	20.8
54.3	5.25	2.28	11.97	7.80	3.01	1.16	0.22	39.2	19.3	19.9
58.8	5.47	2.17	11.87	7.06	3.85	0.96	-0.20	34.9	19.4	15.5

Table A9.11 Power distribution : Helium 7.5 psig

	V	I	Electrical Input, VI	I^2R Loss	Friction	Cooler Power	PV Power	T_h	T_k	dT
Hz	(V)	(A)	(W)	(W)	(W)	(W)	(W)	(C)	(C)	(C)
51.5	4.82	1.98	9.54	5.88	2.11	1.55	0.12	31.6	21.9	9.7
54.9	5.65	2.39	13.50	8.57	2.46	2.48	0.92	36.6	20.8	15.8
58.1	6.63	2.97	19.69	13.23	3.07	3.39	2.00	43.9	19.5	24.4
63.3	6.72	2.99	20.09	13.41	3.59	3.09	1.49	47.2	18.3	28.9
65.8	6.5	2.73	17.75	11.18	4.10	2.47	0.26	45.4	17.9	27.5
69.4	6.74	2.63	17.73	10.38	5.02	2.33	-0.29	41.4	17.2	24.2

Table A9.12 Power distribution : Helium 15 psig

	V	I	Electrical Input, VI	I^2R Loss	Friction	Cooler Power	PV Power	T_h	T_k	dT
Hz	(V)	(A)	(W)	(W)	(W)	(W)	(W)	(C)	(C)	(C)
56.2	5.72	2.32	13.27	8.07	2.51	2.69	0.15	33.1	21.7	11.4
61.0	7.38	3.11	22.95	14.51	3.42	5.03	2.42	44.6	21.5	23.1
64.1	8.38	3.68	30.84	20.31	3.96	6.56	3.29	51	20.6	30.4
67.6	8.86	4.00	35.44	24.00	4.40	7.04	4.46	56	18.9	37.1
70.4	8.38	3.65	30.59	19.98	5.21	5.39	2.90	54.5	18.1	36.4
73.5	8.23	3.34	27.49	16.73	6.14	4.61	1.39	50.9	17	33.9

Table A9.13 Coefficient of performance : Helium 1 atm

	PV2	W_{motor}	W_{cooler}	COP_{cooler}	COP_{thermo}
Hz	(W)	(W)	(W)		
42.0	0.21	0.74	7.07	0.03	0.29
46.8	0.59	1.11	8.79	0.07	0.53
49.0	1.25	1.43	10.93	0.11	0.87
51.5	1.74	1.42	12.87	0.13	1.22
54.3	1.24	1.16	11.97	0.10	1.07
58.8	0.71	0.96	11.87	0.06	0.74

Table A9.14 Coefficient of performance : Helium 7.5 psig

	PV2	W_{motor}	W_{cooler}	COP_{cooler}	COP_{thermo}
Hz	(W)	(W)	(W)		
51.5	0.58	1.55	9.54	0.06	0.38
54.9	1.75	2.48	13.50	0.13	0.70
58.1	3.53	3.39	19.69	0.18	1.04
63.3	3.57	3.09	20.09	0.18	1.15
65.8	2.21	2.47	17.75	0.12	0.89
69.4	1.56	2.33	17.73	0.09	0.67

Table A9.15 Coefficient of performance : Helium 15 psig

	PV2	W_{motor}	W_{cooler}	COP_{cooler}	COP_{thermo}
Hz	(W)	(W)	(W)		
56.2	0.92	2.69	13.27	0.07	0.34
61.0	3.82	5.03	22.95	0.17	0.76
64.1	5.58	6.56	30.84	0.18	0.85
67.6	7.66	7.04	35.44	0.22	1.09
70.4	5.80	5.39	30.59	0.19	1.08
73.5	4.01	4.61	27.49	0.15	0.87

Appendix 10 : Pictorial illustrations of the test apparatus

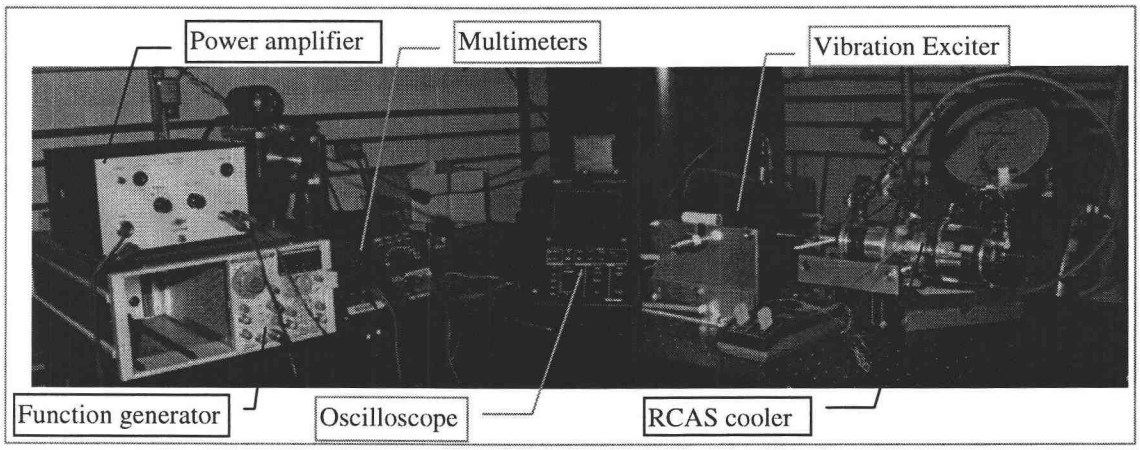

Fig. A10.1 The complete setup of the test apparatus

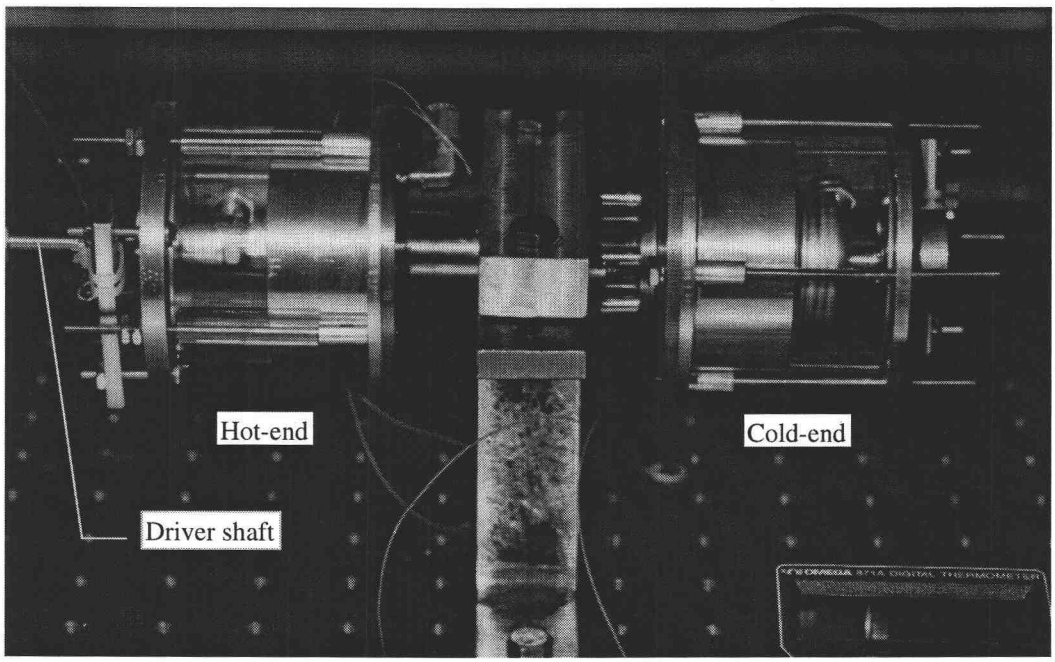

Fig. A10.2 A close-up view of the RCAS cooler

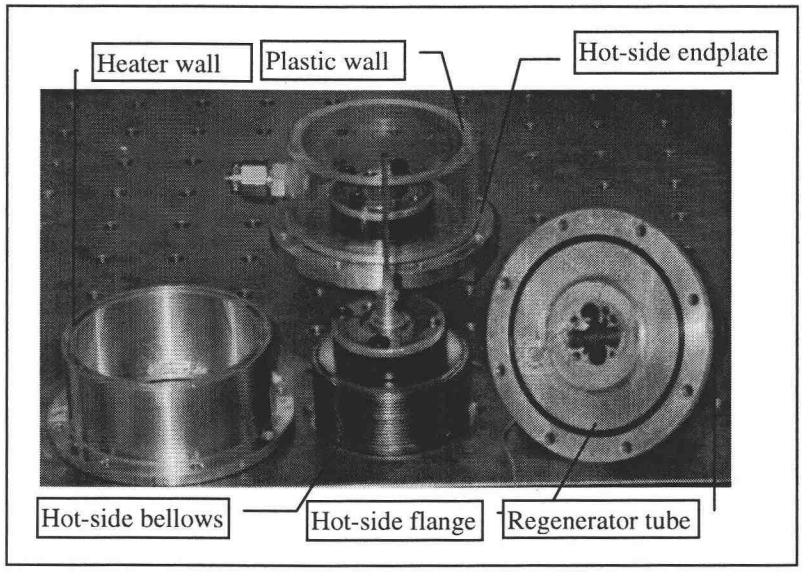

Fig. A10.3 Hot-side assembly

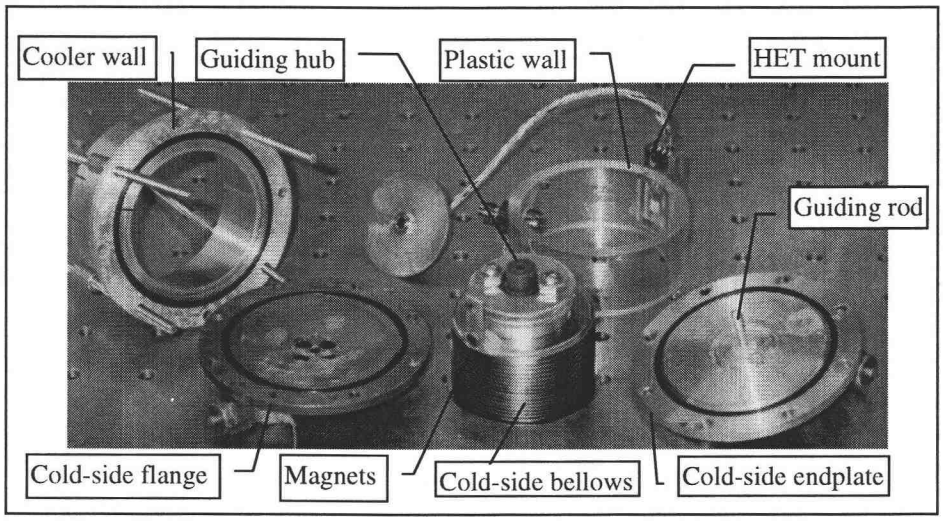

Fig. A10.4 Cold-side assembly

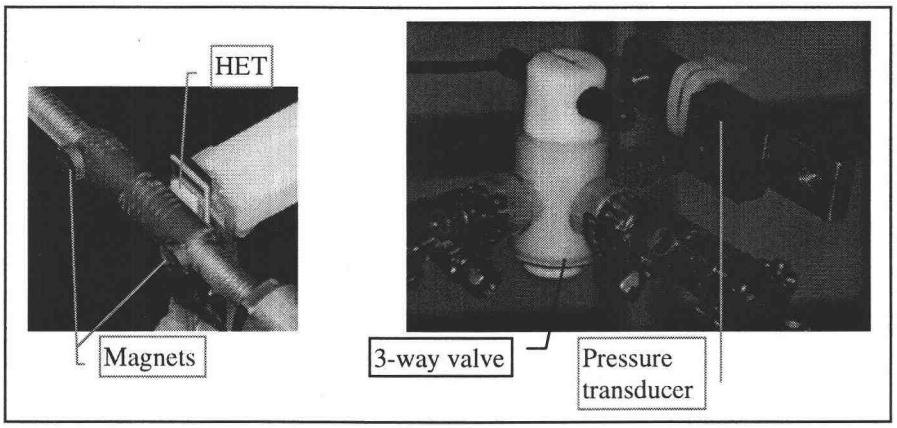

a) HET setup b) Pressure transducer mounting

Fig A10.5 Transducer setup

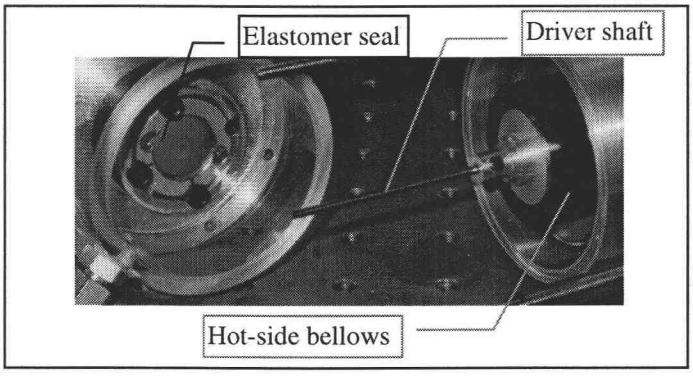

Fig. A10.6 Elastomer seal

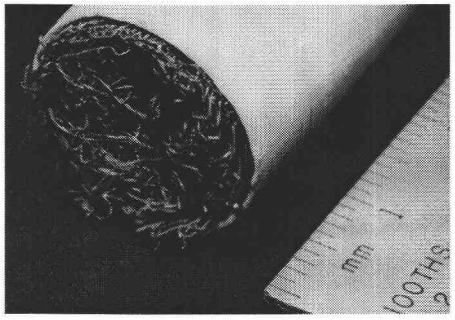

Fig. A10.7 Close-up view of the regenerator matrix : coarse wire wool.